Design and Development of a Minimally Invasive Endoscope: Highly Flexible Stem with Large Deflection and Stiffenable Exoskeleton Structure

By
JungHun Choi

Dissertation submitted to the Faculty of the
Virginia Polytechnic Institute & State University
in Fulfillment of the Requirements for the Degree
Of
Doctor of Philosophy
In
Mechanical Engineering

Approved by

_____
Dr. Robert H. Sturges, Chairman

_____ _____
Dr. Charles F. Reinholtz Dr. Dennis Hong

_____ _____
Dr. Robert L. West Dr. Surot Thangjitham

February 3, 2006
Blacksburg, Virginia

Keywords: endoscopy, colonoscopy, sigmoidoscopy, sigmoid colon cancer, colon biopsy, stiffenable endoscope exoskeleton structure, friction coefficient, stress-strain analysis, elastica.

Design and Development of a Minimally Invasive Endoscope: Highly Flexible Stem with Large Deflection and Stiffenable Exoskeleton Structure

By
JungHun Choi

ABSTRACT

Colonoscopy provides a minimally invasive tool for examining and treating the colon without surgery, but current endoscope designs still cause a degree of pain and injury to the colon wall. The most common colonoscopies are long tubes inserted through the rectum, with locomotion actuators, fiber optic lights, cameras, and biopsy tools on the distal end. The stiffness required to support these tools makes it difficult for the scopes to navigate the twisted path of the colon without damaging the inside wall of the colon or distorting its shape. In addition, little is known about how sharp and forceful endoscopes can be without accidentally cutting into tissue during navigation.

In order to solve the requirements of stiffness (to support tools) and flexibility (to navigate turns), we expanded on a design by Zehel et al. [49], who proposed surrounding a flexible endoscope with an external exoskeleton structure, with controllable stiffness. The exoskeleton structure is comprised of rigid, articulating tubular units, which are stiffened or relaxed by four control cables. The stiffened or locked exoskeleton structure aids navigation and provides stability for the endoscope when it protrudes beyond the exoskeleton structure for

examination and procedures. This research determined the design requirements of such an exoskeleton structure and simulated its behavior in a sigmoid colon model.

To predict just how pointed an endoscope can be without damaging tissue under a given force, we extrapolated a strength model of the descending colon from published stress-strain curves of human colon tissue. Next we analyzed how friction, cable forces, and unit angles interact to hold the exoskeleton structure in a locked position. By creating two- and three-dimensional models of the exoskeleton structure, we optimized the dimensions of the units of an exoskeleton structure (diameter, thickness, and leg angle) and cable holders (cable attachment location) to achieve the turns of the sigmoid colon, while still remaining lockable. Models also predicted the loss of force over the exoskeleton structure due to curving, further determining the required cable angles and friction between units. Finally we determined how the stiffness of the endoscope stem affected locking ability and wear inside the exoskeleton structure.

Acknowledgements

First of all, I would like to confess that all my works and knowledge are belonging to God, and I dedicate myself and all things to Him.

I would like to extend my sincere gratitude to everyone involved in making this research possible. I must think Dr. Robert H. Sturges for the opportunity to learn and work under his advisement, and for his constant support and helpfulness through every aspect of this research. I would also like thank Dr. Charles F. Reinholtz, Dr. Dennis Hong, Dr. Robert L. West, and Dr. Surot Thangjitham , not only for serving as my committee members, but also for encouraging and supporting my education during my time at Virginia Tech.

In addition, I want to thank my parents for their constant love and tireless support throughout my education and my life. I am grateful to my father, BongLak Choi and mother, OckSoon In for their endless praying, encouraging words and for always being proud of my achievements. Also, thanks so much to my father in law, ManKyu Lee and mother in law, YooChan Chung, and their infinite love, prayer, and support. My fiancé, ShinHee Lee gave me endless love and made me successfully finish my study in Virginia Tech. I could not have made it through this time without the support of all family in my life. Lastly, I would like to thank Dr. MunKi Lee, Roger Anderson, and Tiffany New for their support, and friendship.

Table of Contents

List of Figures

List of Tables

1. Introduction

1.1 Endoscopy

In this research, we propose a design and development of an endoscope that has an exoskeleton structure with controllable stiffness and a highly flexible stem. Endoscopy is a minimally invasive procedure and it can minimize risk or side effects associated with open surgery. An endoscope is a device that can pass through the body so that physicians can examine the interior of body organs. Usually, an endoscope comprises fiber optics and lenses for a light source for inspection inside a patient. Small instruments such as scissors, forceps, and baskets can be inserted to obtain the body tissue specimens for biopsy. Currently, many endoscopes are used with a camera to provide an image for better visualization and to save it for further analysis by physicians. Endoscopist has a technical difficulty in 10 to 20% of procedure due to the variable colonic anatomy and fixation. About 10 to 25% of patients cannot be fully examined for the rejection of endoscopy [51]. There are various shapes of endoscopes for the needs of different body parts and their usage. Table 1 shows the types of endoscopes and the target organs.

Table 1. Endoscopy types [50]

The gastrointestinal tract (GI tract)	
Endoscopic device	Target organs
Esophagogastroduodenoscopy	Esophagus, stomach and duodenum
Colonoscopy	Colon
Sigmoidoscopy	Sigmoid colon

The respiratory tract	
Rhinoscopy	The nose
Bronchoscopy	The lower respiratory tract
Cystoscopy	The urinary tract
The female reproductive system	
Culposcopy	The cervix
Hysteroscopy	The uterus
Falloscopy	The Fallopian tubes
Normally closed body cavities through a small incision	
Laparoscopy	The abdominal or pelvic cavity
Arthroscopy	The interior of a joint
Thoracoscopy	Organs of the chest
During pregnancy	
Amnioscopy	The amnion
Fetoscopy	The fetus

We will consider the endoscope that has a long and slender body with a controllable distal tip, and mainly used for colonoscopy or sigmoidoscopy also called proctoscopy. Sigmoidoscopy is using a flexible sigmoidoscope so that a physician can examine the rectum and sigmoid colon. More than two thirds of colon diseases occur at the sigmoid colon and sigmoidoscopy can diagnose inflammatory bowel disease, bowel obstruction, colon cancer, colon polyps, etc. Sigmoidoscopy can also determine the cause of blood, mucus, or pus in the stool and confirm findings of another test by taking a biopsy. Polyp removal is one of the main function of sigmoidoscopy [1,2].

The motion of an endoscope should be flexible enough to minimize the stress on a colon wall and avoid patient pain and discomfort. Many new mechanisms have

been proposed for endoscopes to minimize invasiveness. The previous works improve the function of an endoscope for the aspects of convenience of the endoscopist and are not much focused on the reduction of patient pain and discomfort.

1.2 Literature Review of endoscopes

We categorize endoscopes for the points of dependent/independent types and actuators used in endoscopes. We define two types of endoscopes (dependent/independent) for the shape of endoscopes, and give details of their differences. For actuators, we explain the characteristics of each actuator and its usage. Table 2 shows a brief summary of category of endoscopes.

Table 2. Category of endoscopes

<table>
<tr><td>Shape</td><td colspan="3">Dependent (Connected)</td><td colspan="2">Independent (Disconnected)</td></tr>
<tr><td>Motion</td><td colspan="3">Self-motion</td><td>Self-motion</td><td>No self-motion</td></tr>
<tr><td rowspan="2">Actuators</td><td>SMAs</td><td>Pneumatic Hydraulic</td><td>Motors</td><td>SMAs</td><td>X</td></tr>
<tr><td>Steering</td><td colspan="2">Locomotion</td><td>Locomotion</td><td>Peristaltic motion</td></tr>
</table>

1.2.1 Dependent / Independent type of endoscopes

The dependent type of endoscopes has long cables and tubes for the purpose of operations. The independent type of endoscopes has no attachment and the shape of its body is cylindrical for an easy navigation in a colon.

1.2.1.1 Dependent type of endoscopes

We can define the conventional endoscopes with actuators at the end of tube as the dependent type of endoscopes. The main characteristic of the dependent type is that actuators are attached at the end of endoscopes for locomotion. Endoscopist does not have to push or pull the stem of an endoscope for advancing or retracting the endoscope. Endoscopist can control actuators at the end of an endoscope to navigate inside a colon.

Koji Ikuta, et al. [3] applied SMAs (Shape Memory Alloys) and servo motors to active endoscope and showed the practical purposes. The authors fulfilled the condition of mechanical compliance, which can pass the minimum radius of curvature of a sigmoid colon on a two-dimensional plane.

A. Menciassi, et al. [4] illustrated a semi-autonomous robot for colonoscopy. They proposed a self-propelled device without external forces such as pushing and pulling by endoscopist, and tried to improve colonoscopy in terms of patient pain reduction and easy advancement of a device.

Wan Sing Ng, et al. [5] developed a robotic colonoscope named EndoCrawler for an inspection and surgical procedures. A graphical user interface program can allow users to control two direct current motors for the motion of EndoCrawler and monitor its motion. In vitro and in vivo experiment were performed to see if it

is a viable replacement for the conventional colonoscope. Due to the experiment using the prototype, in vivo experiments and animal trial showed non-smooth advance and collision against the colon wall.

Joel Burdick, et al. [6] developed a prototype robotic endoscope for gastrointestinal diagnosis and therapy. Experiments were performed in rigid tubing and the swine intestine. Because of the size of a prototype design, their future goal is the development of a smaller version of a robotic endoscope, suitable for use in humans.

H.D. Hoeg, et al. [7] discussed the locomotion of a robotic endoscope in the human small intestine and analytical models for the body's blood flow auto regulation mechanism. Low inflation pressure testing of in vivo porcine intestine was done to determine constitutive relations, quantitative models, and simulations of bowel tissue. These experiments and models can help to determine the traction forces from a robot and avoid over-expanding the intestine. They made tissue model and checked the blood circulations for the expansion of the intestine. The expansion shape of the intestine using the locomotion system is not the same as the shape of an expansion test, but the assumptions and the results from the experiments can support their model.

Elizabeth V. Mangan, et al. [13] described the peristaltic endoscope successfully moved both forward and backward within a transparent acrylic tube. The peristaltic endoscope can be used in medical or industrial contexts with necessary medical tools.

1.2.1.2 Independent type of endoscopes

The independent type of endoscope is also called the capsule type. They can be categorized a passive and active type for a mobility point of view. A passive capsule type has no actuator and it is used as a mouth to anus (M2A) method, and an active capsule type has actuators for mobility with wireless control.

Dorin Panescu [12] presented an imaging pill for gastrointestinal endoscopy. The capsule endoscopy called the mouth to anus (M2A) can image and diagnose conditions of most regions of the gastrointestinal tract. The main target of the capsule endoscopy is for the small intestine, which is not easy to access with current endoscopes. The limitations of the capsule endoscopy are the limited field of views because of its dependency on the natural bowel movements and the capsule endoscope cannot sample the tissues for biopsy. Because of the non-controllability, the patients must try the image pill more than one time if the image pill passes a problematic spot in the intestine without capturing an image.

TS. Kim et al. [10] described a functional and controllable robotic endoscopic capsule by the technologies of biomedical engineering, micro-systems, and robotics. The capsule has biopsy tools, legged locomotion, and a stopping mechanism to hold its position. SMA wires are used as actuators, and for the stopping mechanism, biomimetic fibrillar attachment mechanisms are developed to grip the walls of the digestive tract. Wireless electrical power transmission technology has been introduced to overcome the limitations of batteries inside the capsule. In vivo animal testing was done for the evaluation of some functions of the capsule.

BK. Kim et al. [11] proposed the locomotive mechanism for wireless capsule-type endoscopes. They made mechanisms for capsule-type endoscopes using a brushless DC motor, an ionic polymer metal composite, and SMA wires, and analyzed the characteristics of three micro-actuators. Two-way linear actuators comprised of SMA springs are selected as small and efficient actuators. The detailed design and analysis of SMA actuators are explained and in vitro tests under a single surface and three surface contacts are done.

1.2.2 Actuators used in endoscopes

Pneumatic/hydraulic actuators are mainly used in the dependent type of endoscopes for advancing and retracting. Shape memory alloys are used in the independent type of endoscopes for the steering and mobility purpose. We describe the characteristics and usages of each actuator.

1.2.2.1 Shape Memory Alloys (SMAs)

Shape memory alloys are used for the steering purpose for dependent type and locomotion purpose for independent type of endoscopes.

Koji Ikuta, et al. [3] discussed a control system Shape Memory Alloy (SMA) servo actuators and its application to an active endoscope. First, they proposed a new control scheme of antagonistic type SMA actuator with electric resistance feedback and verified by some experiments. They also achieved reduced hysteresis and overheating of SMA actuator.

A. Menciassi, et al. [4] used three Shape Memory Alloy (SMA) springs to steer the entire robot body and a distal tip. Three SMA springs are installed at the central bellow to elongate and retract the entire body. A distal tip is designed with a silicon bellow and three SMA springs for an enhanced visualization and performance. Cold air is applied in the silicone bellow to cool SMA springs and to decrease the response time of the system.

TS. Kim et al. [10] used SMA wires as actuators, and Pulse Width Modulation (PWM) technique is used for a homogeneous heating of the SMA. The actuator consists of a PEEK structure, a leg, and an actuation mean. SMA wires and pulley are connected in the PEEK structure, and the lag is connected to the pulley. Activation of SMA wires rotates the leg, and a body can be advanced.

BK. Kim et al. [11] selected two-way linear actuators as bi-directoinal linear actuators, and the actuators comprised of SMA springs, clampers, and a capsule body. The principle of mobility is as follows:
The clamper moves forward when a front linear actuator is connected. After forwarding, the clamper holds the contact surface, and the body moves forward during the contraction of the rear linear actuator. The clamper releases the contact surface and slides forward while the front linear actuator is contracting.

1.2.2.2 Pneumatic/hydraulic actuators

Pneumatic/hydraulic actuators are used for a locomotion purpose for dependent type of endoscopes. Pneumatic actuators are one of the popular actuators to make

an advance motion of an endoscope, and they are very positive for the point of operational speed and energy efficiency.

A. Menciassi, et al. [4] developed a propulsion mechanism based on the inchworm locomotion. The authors combined the inchworm and sliding clamper solutions to overcome the flexibility and tortuousness of the colon. Pneumatic mechanism such as a vacuum generator, on-off valves, and manual pressure regulator can make elongation and retraction phases for the movement of the endoscope.

Wan Sing Ng, et al. [5] developed a robotic endoscope named EndoCrawler. By using rubber bellow actuators, EndoCrawler pushes against the colon wall and makes self-propulsion without helping of external forces. To advance a robotic colonoscope, pressurized air and vacuum are introduced to inflate and collapse the base of the bellow actuator.

Joel Burdick, et al. [6] introduced a concept of locomotion by using the components of traction and extensor segments. Hydraulic power actuation can locally increase the diameter of the traction segments. Extensor segments were designed to expand and contract along the local axial direction. The specific sequences of gripping and stretching cause the net displacement of the robotic endoscope.

H.D. Hoeg, et al. [7] developed a robotic endoscope for the small intestines. The locomotion system is the same as Joel Burdick's [6] and they reduced the size of the prototype of the robotic endoscope to fit into a human small intestine.

Elizabeth V. Mangan, et al. [13] described a device, which has three actuators in series. It is comprised of three serial pneumatic actuators and can make a peristaltic locomotion. The locomotion efficiency, speed of the robot, and a slip with an inner wall are suggested for the future works.

1.2.2.3 Magnetic actuators

Magnetic actuators are used for the locomotion purpose for independent type of endoscopes.

M. Sendoh, et al. [9] proposed a magnetic actuator for a capsule endoscope. The capsule-type magnetic actuator contains a permanent magnet inside, and the outside shape is a spiral. External rotational magnetic field can rotate and advance the capsule. Moving velocity and starting torque were measured to specify its moving characteristic evaluation. The magnetic actuator does not need an internal source of power and has a simple structure. To activate the magnetic actuator, large amount of magnetic fields have to be generated in many directions into a human body and no effects of the magnetic fields or possible interferences with other medical equipments are conveyed to a human body.

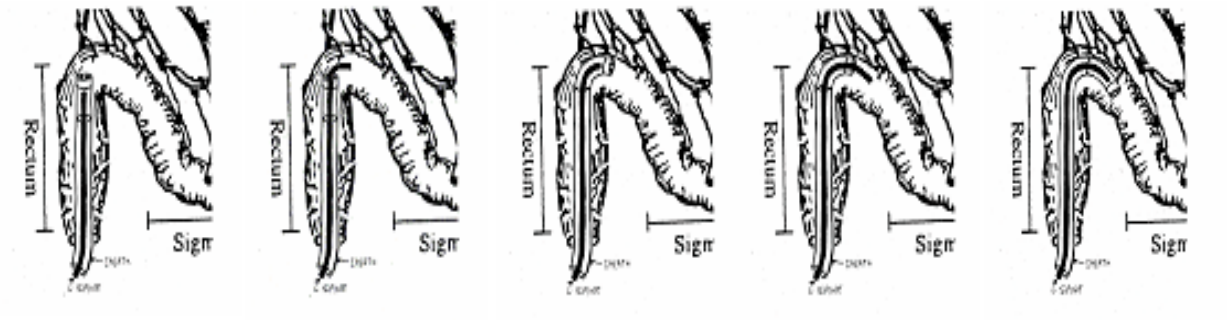

Figure 1. Representation of an endoscope traveling through colon with alternate stiffening and relaxing of exoskeleton structure [16]

Sturges et al. [14] proposed way of guiding an endoscope to reduce patient's pain by introducing controllable stiffness of the exoskeleton structure and an alternate sliding motion of an endoscope. Figure 1 shows the procedure of an endoscope traveling through colon with alternate stiffening and relaxing of exoskeleton structure. In Figure 1, the bold line depicts the stem of the endoscope. Figure 1-A shows the endoscope inside the rectum with the surrounding exoskeleton structure stiffened. In Figure 1-B, the endoscopist advances the stem a short distance, using visual feedback to steer the distal tip of the endoscope with minimal contacting of the colon wall. In Figure 1-C, the exoskeleton structure is relaxed. It is advanced the same distance that the endoscope is advanced using the guidance of the distal tip. The endoscopist can once again stiffen the exoskeleton structure and advance the endoscope as shown in Figure 1-D. In a similar manner, the exoskeleton structure is relaxed and advanced. The result is shown in Figure 1-E. In this way, we can minimize the stress on the colon wall and explore inside the human colon.

1.3 Literature Review of the Friction Analysis

Hual-Te T. Huang and B. Ravani [20] presented for analysis of contact stresses and deformation conditions in ball screw mechanism using the tubular medial axis representation of contacting surface. The authors obtained simplified Hertzian contact solutions using the curvature information. The frictional effect and the temperature effect are not addressed and left for the future research.

S.A. Lukowski et. al [21] explained an analysis of the contact stress and frictional coupling elements of multi-disk stepless transmission with initial point contact. They applied Hertz's formulation for the stresses on curved bodies for both point and line contact cases, assuming isotropic materials.

L.J. Gutkowski and G.L. Kinzel [22] developed the force-constraint equations on spherical joints with Coulomb friction. The reasonably modeled friction effects in a spherical joint are the very important characteristics of the work. The paper also helped to understand how Coulomb friction manifests in a spherical joint.

Ali Faraz and Shahram Payandeh [23] considered two approximate models of coulomb frictional moments in revolute pin joints and spherical-socket ball joints. In this paper, the authors proposed more accurate estimation of the Coulomb frictional moment and compact solution that can be extended to other geometrical multi-body contact configurations.

Y.J. Shin and C.H. Kim [24] introduced a new solution for the analysis of multi-body systems with spherical joint under Coulomb friction. The authors derived the complete solutions of governing equations and reaction forces by using

Lagrangian formulation. The methods were applied to the components of a car air conditioning compressor and examined the effectiveness.

2. Characteristics of a human colon

This chapter analyzes how much force can be applied to the inner tissue of a human colon, by different shapes of instruments, without causing damage. We hope to provide useful information on the magnitude of force which a colon can tolerate without pain for the patient or damage to colon tissue. This information will guide our endoscope and an exoskeleton structure design, and should prove useful to others in the field of endoscopy.

Some of the researches have been done for mechanical properties of a descending colon [15,38,39], but the results of tension or expansion tests are still not enough to determine the force limits for different sizes of end tools. We develop a simple colon model to find out a damage level of the colon wall with various sizes of spherical end tools. We used previously experimented results [15].

2.1 Structure of a human colon

Improving endoscopes requires basic knowledge of the function and structure of a human colon. The normal functions of a human colon are dehydration, secretion of mucus, and transport of undigested food residues by peristaltic contractions. A human colon begins at the cecum, or portal from the small intestine, followed by the ascending colon, transverse colon, descending colon, sigmoid colon, rectum, and anus. The ascending colon is located on the right side of the abdomen, between the cecum and the transverse colon. It is shorter than the descending colon, with a length of about one foot. The transverse colon lies from right to left in the abdomen, between the ascending colon and the descending colon. The descending colon descends retrogradely in the left part of the abdomen, to the

sigmoid colon. The sigmoid colon has a generally twisted shape and is connected to the rectum. The exact boundary of the sigmoid colon cannot be defined along the colon, and its diameter is about 2.5 cm. The rectum is located at the lower end of the colon and has a relatively straight shape. The anus is the end of the colon system and is connected to the anal canal, which is approximately 4 cm long [1,2]. After a colonoscope passes the rectum, endoscopists encounter the first curve of the sigmoid colon (2.45 cm radius of curvature). This describes the general shape of a normal colon, though abnormal colons may follow a much more tortured shape.

The many twists and turns in the colon present an interesting challenge for colonoscopies. Endoscopes must be stiff enough to proceed into the colon, but not so stiff that they cannot bend and curve to accommodate the colon shape. Overly rigid endoscopes can also damage the interior surface of the colon. On the other hand, overly flexible scopes cannot support the cameras, biopsy tools, and other instruments so crucial to an effective endoscope.

2.2 Mechanical properties of a human colon

In order to understand and model the strength of human colon tissue, we will analyze the stress-strain values measured by previous investigators. From these stress-strain curves, we extrapolate the elastic limit of the descending colon, relative to various sizes of end tools. This allows us to create a strength model of a descending colon in relation to tools commonly used on colonoscopes. This model will later be used to inform decisions regarding the shape and forces allowable in our own endoscope and an exoskeleton structure design.

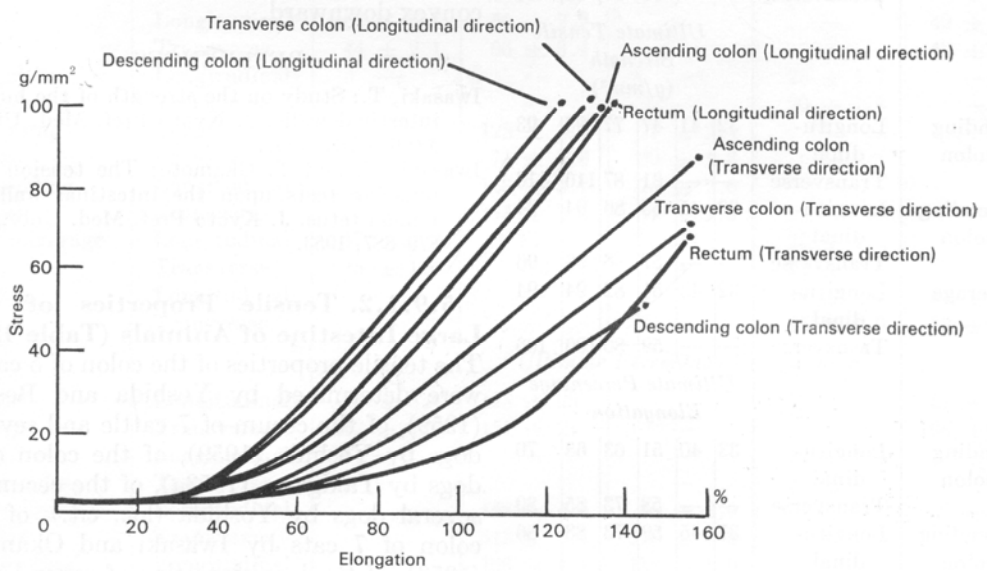

Figure 2. Stress-strain curves in tension of the large intestine of persons 20 to 29 years of age [15]

Yamada performed a variety of experiments to find out the mechanical properties and characteristics of human organs [15]. The dimensions of his tissue samples were 10 mm in length, 2~3mm in width, with a length-width ratio of 3:1. The testing machines used in tension tests of organ tissues were the Schopper and the Amsler tension testers, with various weight capacities. For the sample of a human colon, the gauge length for the test sample was the distance between points marked at each end of reduced region.

Figure 2 shows stress-strain curves of different parts of a human colon. The ultimate elongation in the transverse direction is greater than that in the longitudinal direction for four parts of a human colon. The ultimate tensile strengths of the descending colon in the longitudinal and transverse directions are

100 and 49 g/mm^2, respectively. Due to elastic characteristics of samples, there is a pre-stress to the sample at zero elongation of about 3.7 g/mm^2.

Actually, Figure 2 represents engineering stress versus percentage of elongation curve. From Figure 2, the elongation is up to 140% of the original length, and we should consider the reduced area for each load and transform the engineering stress-stress curve in a true stress-strain curve. From elementary mechanics, we have:

$$\sigma_E = \frac{P}{A_0} \text{ and } \varepsilon_E = \frac{\Delta l}{l_0} \qquad (1)$$

$$\sigma_T = \frac{P}{A} \text{ and } \varepsilon_T = \ln(1+\varepsilon_E) \qquad (2)$$

Where,

σ_E : *Engineering stress*
ε_E : *Engineering strain*
σ_T : *True stress*
ε_T : *True strain*
P : *Load*
A_0 : *Initial area*
A : *Instantaneous cross sectional area*

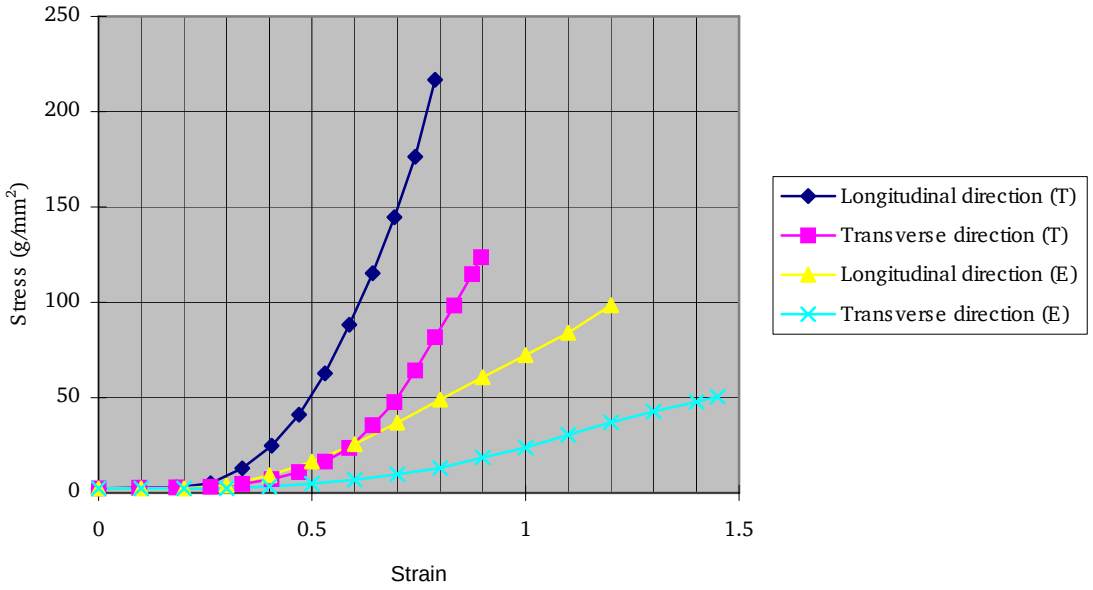

Figure 3. Stress-strain curves in tension of the large intestine of persons 20 to 29 years of age (descending colon only with true and engineering stress-strain curves)

We solved for the true stress and strain by using the engineering stress, strain, and equation (2). Figure 3 shows both engineering and true stress-strain curves of a descendent colon only. For small strains, engineering and true stress-strain curves have relatively similar values, but there are significant differences of stress as the strain goes to large values because of the reduction of area. We will use true stress and strain values to establish the simple model of a descending colon for the next chapter.

2.3 Simple characteristic modeling of a human colon

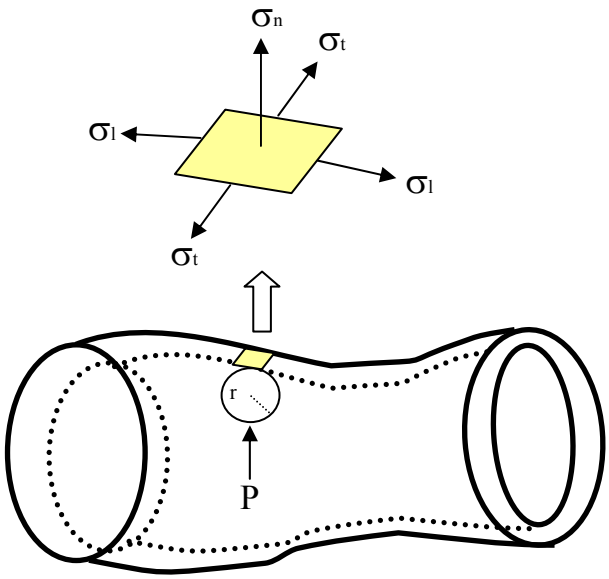

Figure 4. Ball with force P inside a descending colon

(σ_l, σ_t, and σ_n are stresses on the longitudinal, transverse, and normal directions. P is a force on the ball and r is a radius of the ball.)

The next step in predicting what kind of force the colon tissue can withstand is to create a model of the human colon. The goal is to transform the stress-strain curves presented above into a model of the mechanical properties of a human colon. The model should guide researchers in designing the shape and size of tool that colon tissue can tolerate.

This model is insensitive to the length and boundary conditions of a colon. Naturally, colon tissue can withstand greater force if it is spread out over a large, blunt area. In order to predict just how pointed an endoscopic tool can be without

damaging tissue under a given force, we simulate a rounded distal tool as a ball with radius *r* and applied force *P*. Figure 4 shows a schematic of the colon and tool model.

Initially, the ball makes contact to the inside of a colon wall with an initial force. If applied force *P* increases, then the stresses of longitudinal, transverse, and normal directions will increase. To simplify the problem, we assumed that longitudinal and transverse stresses have the same strain values from the given stress. In reality, the shape of a human colon is arbitrary from person to person, but our model is insensitive to the boundary condition or length of a colon. We used the mean stress of longitudinal and transverse direction in the true stress-strain curves from the assumption. We used the thin wall theory to approach the stress-strain problem of the colon wall.

$$\sigma_M = \frac{\sigma_l + \sigma_t}{2} = \frac{\sigma_n r}{2t} \qquad (3)$$

$$\sigma_n = \sigma_M \frac{2t}{r} \qquad (4)$$

For a unit thickness of a descending colon, we can set t=1mm and equation (4) becomes the following:

$$\sigma_n = \sigma_M \frac{2}{r} \qquad (5)$$

Equation (5) shows that the normal stress is proportional to two times the mean stress over the radius. If the radius of the ball that contacts inside a descending

colon becomes large, then the normal stress will have a small value and the breaking strength will be slowly increased with respect to the large value of strain.

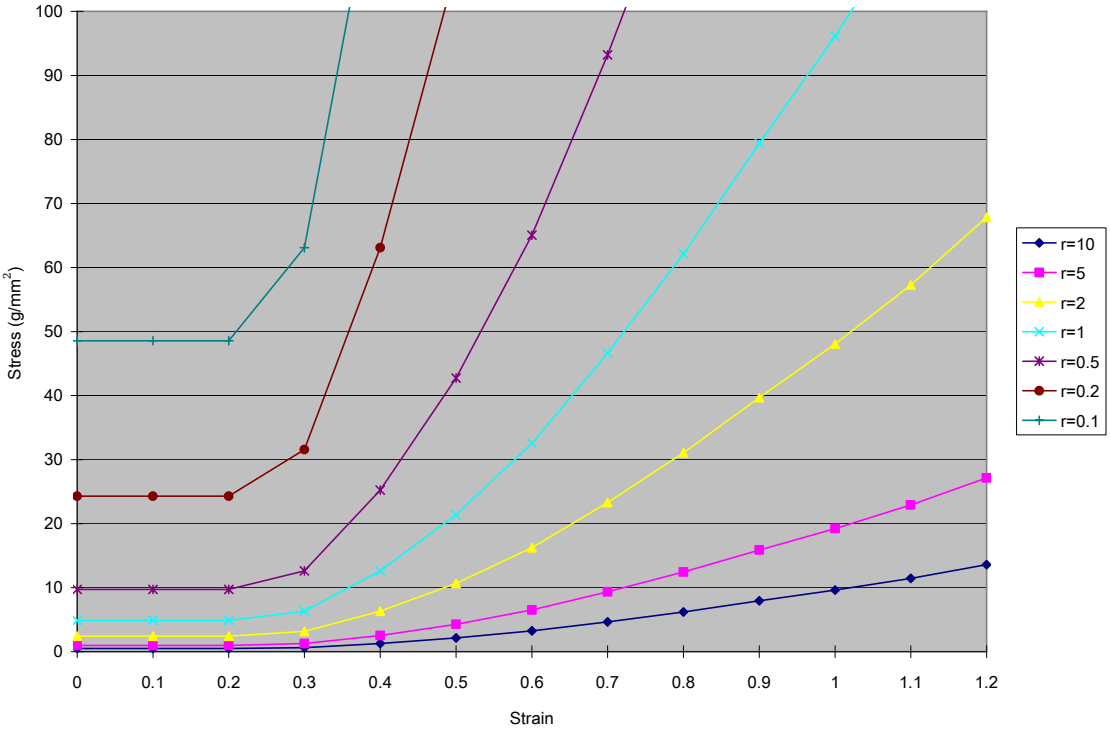

Figure 5. The stress-strain curve for the different radii.

We used equation (5) to find normal stress versus true strain for the different values of radius. The different radii represent various tool ends from dull to sharp needle-type tool ends in seven grades. Figure 5 shows the stress-strain curve for the different radii. Now we can derive forces from true stress values and radii of the ball. We assumed that the ball had an initial contact to the inner surface of a descending colon with initial forces. The assumption of an initial contact is from

Yamada's tension test [15]. Because of very soft and elastic characteristics of a colon, strain can be increased with small stress or force. In a two-dimensional plane, we assumed that an initial contact length between the ball and a colon wall caused by an initial force is the diameter of a ball. The contact length can be varied with an initial force, but we are interested in final situation for the large strain rather than transient interface between the ball and a colon wall. Initial contact area will not much affect to the final breaking strength or damaging strength of the colon tissue. For the given radius we can decide the range of contact length:

$$2r \leq \textit{contact length} \leq \pi r$$

πr is a circumference of a half circle.

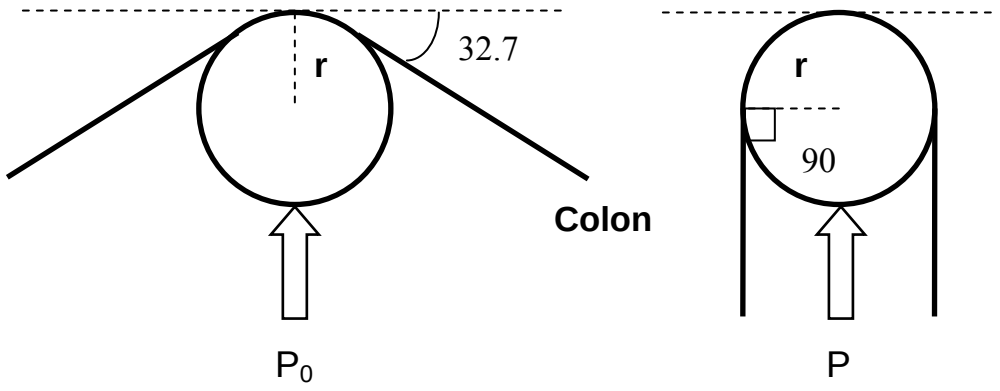

Figure 6. Contact shape between a ball and a colon wall with forces.

(P_0: initial force. P: force after true strain value of 0.45)

The initial contact length is 2r and maximum contact length is πr. The corresponding true strain values are zero and 0.45. Figure 6 shows two contact figures between the ball and a colon wall with forces. The initial angle of a colon wall is 32.7° from the left side of Figure 6, and initial angle 32.7° is the corresponding value of initial contact length 2r. No more contact will be made after 90° angle of colon wall. We can convert the contact length to a contact area by using the geometry of a half circle.

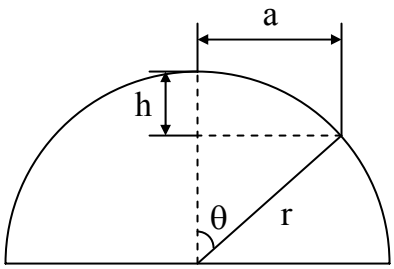

Figure 7. Geometry of a half-circle with a radius of r

Figure 7 shows geometry of a half-circle with a radius of r and θ starts from a vertical dashed line. Once we know the contact length, then we can solve for θ. From Figure 7, the r is a fixed constant and parameter h can be obtained from equation (6).

$$h = r(1-\cos\theta) \qquad (6)$$

After we solve for the parameter h, we can calculate a contact surface area.

$M=2\pi\times r\times h$ (7)

M is a surface contact area of a hemisphere with a radius of r.

Finally force P that pushes a ball to a colon wall is normal stress times contact area.

$$Force\ P\ (g)=\sigma_n\ (g/mm^2)\times M\ (mm) \quad (8)$$

Figure 8 and 9 show the result of equation (8).

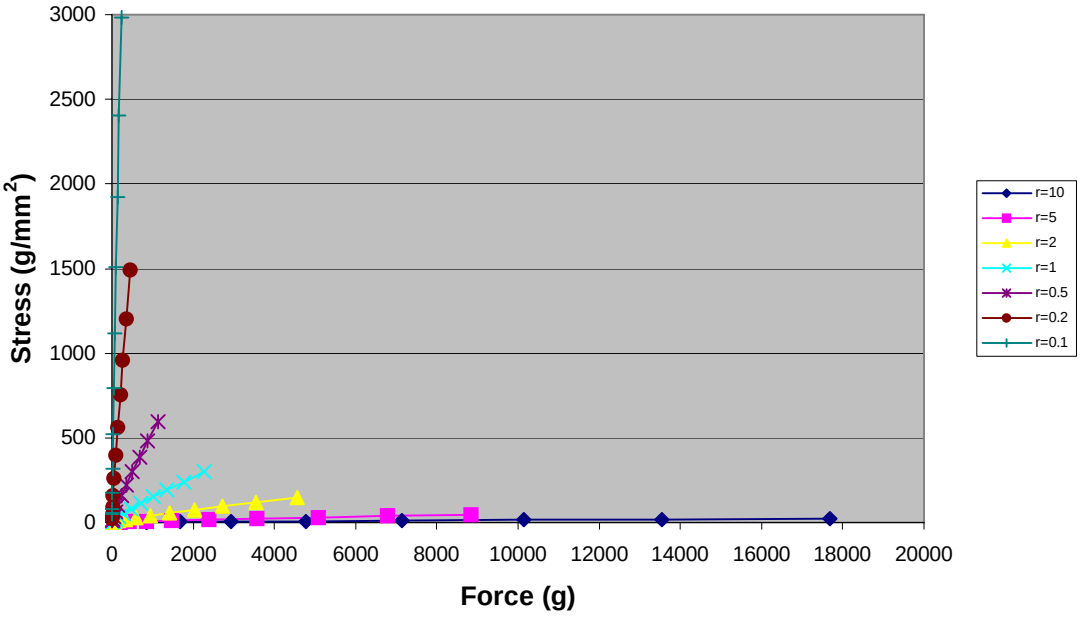

Figure 8. Stress-force curves for different radii.
(The unit of r is mm)

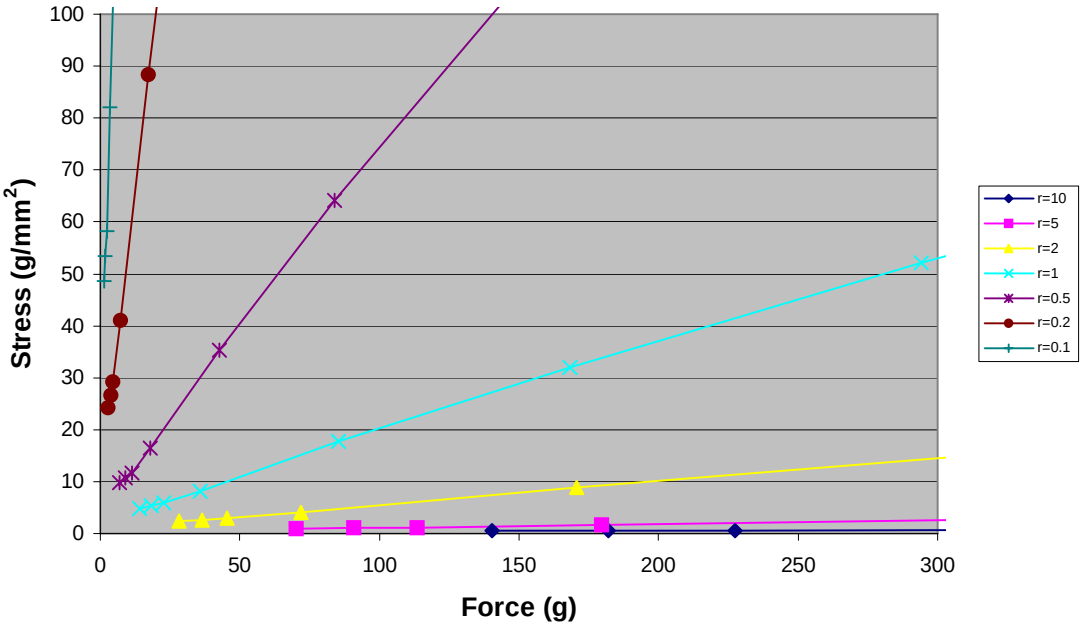

Figure 9. Figure 8 is repeated with a magnification of the initial region.
(The unit of r is mm)

Figure 8 shows stress-force curves for the different value of ball radii, and Figure 9 is the magnification of initial region of Figure 8 for detailed look of the initial region. Initial stresses are all different for the given radii because of different contact values between the surface of the ball and a colon wall. When a radius r is smaller, the stress is getting larger including the initial stress. From Figure 8, the end points of each graph form a $\frac{1}{F}$ curve, and the reason is that boundary condition of the colon model is insensitive to the colon length. Since the colon has an elastic limit and the percentage of elastic recovery of the transverse colon is 43% of its ultimate strength, we can set the damage level of a colon wall to 32 g/mm^2 for the different radii.

Table 3. Elastic limit of force for different radii

Radius (mm)	Elastic limit of force (g)
0.1	N/A
0.2	5
0.5	38
1	168
2	N/A
5	
10	

Table 3 shows the elastic limit of force for different radii. The range of ball radius in our model is from 0.1 to 10 mm, and Yamada's experimental data can cover the ball radius of 0.2, 0.5, and 1.0 mm.

In the case of radius 0.1, the colon wall will be broken before it fulfills the initial contact condition. For the radius 2, 5, and 10, they cannot reach the elastic limit of stress for the given range of force. It means that the contact area between the surface of the ball and a colon wall is wide enough to sustain forces. Thus we have briefly reviewed the structure of a human colon, and determined the elastic limits of forces for different radii of tools.

3. System Description

To develop a minimally invasive endoscope, we designed an exoskeleton structure which an endoscopist can stiffen or relax while easing the endoscope into the colon. The stiffenable exoskeleton structure is controlled by pulling and relaxing two cables. The endoscope is inserted and moved through the inside of this exoskeleton structure, which acts like an exoskeleton for the endoscope. To collect visual data or biopsies, the distal tip of the endoscope is advanced a few cm beyond the end of the exoskeleton structure. This chapter will present the exoskeleton structure design, comprised of cylindrical rigid units, as well as the design requirements and parameters of the entire unit.

In order to analyze the force applied by the exoskeleton structure and stem unit, we derive a series of force balance of equations, solving for the required friction coefficient between two units. To check the relations of cable forces and the geometry of the unit, we analyze cable forces with respect to the cable angle, and we find the loss of cable forces is a function of cable angles.

The geometric restrictions of a colon and the functionality of a minimally invasive endoscope create design requirements and objective parameters. We develop a geometric model based on Sturges' model [14] and analyze cable forces relative to this model. A closed form solution of the friction coefficient is calculated to check the functionality of the model.

3.1 Design Requirements

We describe design requirements and geometric constraints for a minimally invasive endoscope. Because we aim at sigmoidoscopy, the design will have to accommodate the sharp curve at the start of the sigmoid colon and reach the full length of the sigmoid colon. The radius of curvature of the first sharp curve of the sigmoid colon can be treated as a geometric requirement. The total length of the exoskeleton structure reaches up to the end of sigmoid colon. For the purpose of stability analysis, the units should maintain contact with each other when the two cables are pulled and the exoskeleton structure is stiffened. The detailed design requirements follow.

Radius of curvature – The unit must be able to pass the junction between the rectum and sigmoid colon. Generally, this is the sharpest turn of the human colon. This means the unit must be able to bend with a 25mm of radius of curvature.

Total length of the endoscope – Approximately 60% of the colon diseases occur in rectum and sigmoid colon; thus we have designed a unit that will perform a complete sigmoidoscopy. So reach the end of the sigmoid colon, the total length of the endoscope must be 500mm.

Contact ability - We assumed that each cylindrical rigid unit inside the stiffenable exoskeleton structure keeps contacting its neighboring units constantly on both sides, as viewed in cross section. These cylindrical units are conically tapered, so that they will articulate inside of each other, maintaining contact

with each other. We will not consider the case in which some cylindrical units might lose contact with each other.

Locking ability – In order to guide and hold the endoscope stem, the exoskeleton structure must be lockable. When cable forces are applied to the cylindrical rigid units inside the exoskeleton structure, and they do not subsequently move relative to each other as a result, we say units have a locking ability. According to our model, the required friction coefficient μ for locking is a function of cable forces and geometrical variables. If the friction coefficient is less than the value of a required friction coefficient, the unit will have a locking ability.

Clearance – Clearance is the minimum clear aperture between successive units of the exoskeleton structure. The exoskeleton structure of the endoscope is like an exoskeleton structure surrounding a highly flexible endoscope; the endoscope is inserted and moved through the inside of the exoskeleton structure. The minimum clearance is the diameter of the distal tip of the endoscope, which is 12 mm. Thus even when the exoskeleton structure is bent to its full capacity, it still must leave just over 12 mm inner clearance for the endoscope to pass through. To accommodate visual data taking and biopsy collection, distal tip of the endoscope will be advanced a few cm outside the exoskeleton structure. Thus the exoskeleton structure must have at least a 12mm opening.

3.2 Geometric Model

The exoskeleton structure unit is designed to allow it to bend and lock inside the colon. The exoskeleton structure of the endoscope is comprised of a series of small, rigid cylindrical units. These cylindrical units are conically tapered, so that they will articulate next to each other, allowing the exoskeleton structure to bend inside the colon. The geometric model of the unit is based on Sturges' model [14]. A cylindrical geometry of units is assumed for the exoskeleton structure. Each unit has four small holes to constrain tendon cables radially but not axially at points *p*. A highly flexible endoscope will be inside the exoskeleton structure. If we apply the appropriate ratio of cable forces, the two units will have a locking ability. When no cable forces are applied, the stem is flexible, enough not to make the shape of a colon. The leg angle ($\theta_{leg\ angle}$) is defined as the angle of the internal cone of the unit. The maximum angle that the unit can rotate about the center "o" is $\theta_{leg\ angle}$.

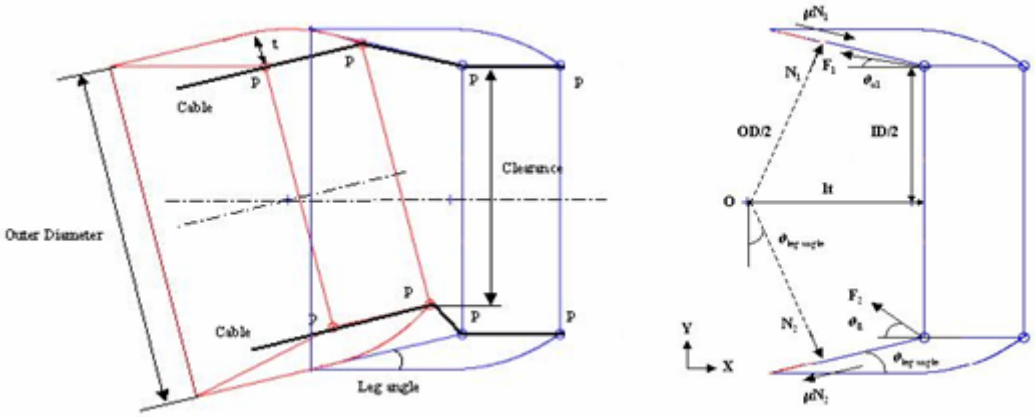

Figure 10. Configuration and free-body diagram of the unit.

3.3 Free-Body Diagram of the Unit

We need to know the required friction coefficient to determine the locking ability between two units. The required friction coefficient can be achieved after we make the free body diagram and solve three force balance equations.

We make a kinematic model of the unit, and analyze the cable forces and friction coefficient from the free body diagram of the model. Using the free-body diagram in Figure 10, we drive three equations (Equations (9), (10), and (11)) to solve for three unknown variables: N_1, N_2, and μ, where N_1 and N_2 are contact forces between the ring elements. F_1 and F_2 are upper and lower cable forces, and N_1 and N_2 are normal forces from the center of the ring element to the conical surfaces. Four cases must be examined for all possible configurations of the respective units: the rotation CW or CCW and force conditions of $F_1 \geq F_2$, and $F_1 < F_2$. Two possible cases of cable forces ($F_1 \geq F_2$, or $F_1 < F_2$) will change the direction of friction forces (μN_1 and μN_2), which will affect the direction of the moment at the center of a unit. Two directions of rotation angle will change the sign of the cable angles relative to the horizontal axis. Figure 10 shows the case when the unit has a CCW rotation and $F_1 \geq F_2$.

From the free-body diagram of Figure 10, the sum of forces in the x-direction is

$$\Sigma F_x : (N_1 + N_2)\sin\theta + \mu(N_1 - N_2)\cos\theta - F_1\cos\theta_{u1} - F_2\cos\theta_{l1} = 0 \qquad (9)$$

The sum of forces in the y-direction is

$$\Sigma F_y : (N_1 - N_2)\cos\theta - \mu(N_1 + N_2)\sin\theta + F_1\sin\theta_{u1} + F_2\sin\theta_{l1} = 0 \qquad (10)$$

The sum of moments at the point "o" is

$$\Sigma T : -\mu(N_1 + N_2)\frac{OD}{2} + (F_1 \cos\theta_{u1} - F_2 \cos\theta_{l1})\frac{ID}{2} + lt(F_1 \sin\theta_{u1} + F_2 \sin\theta_{l1}) = 0 \qquad (11)$$

3.4 Cable Force Analysis

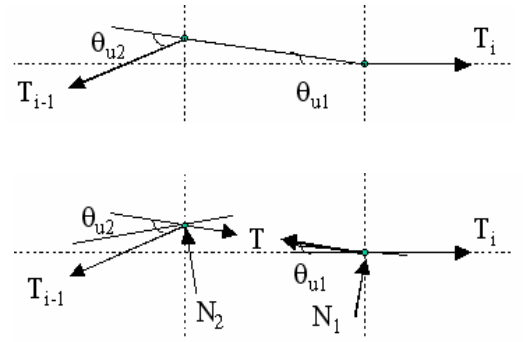

Figure 11. Analysis of cable force

To determine the ability of the exoskeleton structure to achieve locking along its entire length, we calculate the loss of force in each cable from one element to the next due to friction and geometry. Figure 11 is a view of a single cable from Figure 10 shown twice for the purposes of cable force analysis. The lower figure represents free-body diagram with two reaction forces N_1 and N_2. The cable diameters are assumed to be negligibly small for the force analysis. The leg angle ($\theta_{leg\ angle}$) is defined as the angle of the internal cone of the unit. The friction

coefficient between the cables and the unit is assumed to be 0.15 for stainless steel on aluminum. (If another cable material such as aramid fiber is selected, this value will be lower.) θ_{u1} and θ_{u2} are the upper angles between the two cables and their contacting units, respectively.

From Figure 11, the contact force N_1 is

$$N_1 = \mu_{cable}(T_i + T)\sin\frac{\theta_{u1}}{2} \tag{12}$$

Summing forces in the horizontal direction, we obtain

$$T\cos\frac{\theta_{u1}}{2} = T_i\cos\frac{\theta_{u1}}{2} + \mu_{cable}(T_i + T)\sin\frac{\theta_{u1}}{2} \tag{13}$$

From the equation above, we can derive the relation between force T and T_i as

$$T = T_i\frac{\left(\cos\frac{\theta_{u1}}{2} + \mu_{cable}\sin\frac{\theta_{u1}}{2}\right)}{\left(\cos\frac{\theta_{u1}}{2} - \mu_{cable}\sin\frac{\theta_{u1}}{2}\right)} = T_i\frac{\left(1 + \mu_{cable}\tan\frac{\theta_{u1}}{2}\right)}{\left(1 - \mu_{cable}\tan\frac{\theta_{u1}}{2}\right)} \tag{14}$$

In the same manner, we can solve N_2 and T with respect to T_{i-1} to find that

$$T = T_{i-1}\frac{\left(\cos\frac{\theta_{u2}}{2} - \mu_{cable}\sin\frac{\theta_{u2}}{2}\right)}{\left(\cos\frac{\theta_{u2}}{2} + \mu_{cable}\sin\frac{\theta_{u2}}{2}\right)} = T_{i-1}\frac{\left(1 - \mu_{cable}\tan\frac{\theta_{u2}}{2}\right)}{\left(1 + \mu_{cable}\tan\frac{\theta_{u2}}{2}\right)} \tag{15}$$

From equation (14) and (15), we can derive T_i as the following function of T_{i-1}, μ_{cable}, θ_{u1} and θ_{u2} :

$$T_i = T_{i-1} \frac{\left(1 - \mu_{cable} \tan \frac{\theta_{u1}}{2}\right)\left(1 - \mu_{cable} \tan \frac{\theta_{u2}}{2}\right)}{\left(1 + \mu_{cable} \tan \frac{\theta_{u1}}{2}\right)\left(1 + \mu_{cable} \tan \frac{\theta_{u2}}{2}\right)} \tag{16}$$

Since μ_{cable} depends on the materials, if we select the value of μ_{cable}, then θ_{u1} and θ_{u2} are the key variables, which affect the loss of force. If θ_{u1} and θ_{u2} are zero, both cables are straight and there are no friction forces; no loss of force will occur. For a given leg angle, θ_{u1} and θ_{u2} have to be minimum values to achieve the maximum efficiency of force transfer to the next unit. Equation (16) will also be applied to the lower angles θ_{l1} and θ_{l2} for that case.

3.5 Closed Form Solutions of Friction Coefficient μ

From the closed form solution of the friction coefficient and the constraint conditions, we can determine the locking ability between two units with two cable forces. Equation (9), (10), and (11) from the free-body diagram are solved using Mathematica™. See Appendix A for the closed form solution of the friction coefficient. There are two sets of closed-form solutions for μ, and we select the set with a friction coefficient. There are two constraints from the solution of the friction coefficient. First, if F_1 equals F_2 and both θ_{u1} and θ_{u2} are zero, then the denominator of the solution of the friction coefficient is zero. We assumed that if F_1 equals F_2 and both θ_{u1} and θ_{u2} are zero, the friction coefficient is equal to zero and no forces due to friction exist. The second constraint condition is that the argument of the square root of the solution of the friction coefficient has to be equal or greater than zero. This constraint condition is always satisfied under the normal design values, such as $OD > ID > 0$ and $Lt > 0$.

4. Design Parameters

To select the geometrical dimensions of the cylindrical units, and check its functionality, we determine the geometric variables of the unit. To ensure that the units will be able to lock and hold their place, we must also determine the range of cable forces that will make the units lock, or hold their positions. We will also examine the location of cable attachments on each unit, for optimal control of the exoskeleton structure. These geometric variables must also fulfill the design requirements specified in Section 3.1.

In order to visualize the relationship among the geometric variables, we have selected Taguchi's factorial orthogonal array method of tabulating the data and providing an error index [19]. Taguchi's method will help optimize the outer diameter, thickness, and leg angle of the units. Next we will examine the range of cable forces and corresponding friction coefficients which will allow the units to lock. Section 4.4 analyzes how the force each cable can apply is affected by the rotation angle of the units. And finally, Section 4.5 examines the optimal location of cable attachments on each unit. These analyses will assist in the final design of the units, how they should articulate, and where/how the control cables should attach.

4.1 Selection of geometric variables

According to the basic shape of the unit in Chapter 3, we have three independent geometric variables to optimize and they are outer diameter, thickness, and leg angle of the unit. First, we manually set the ranges of control variables and

narrowed them by a trial and error method. Taguchi's factorial orthogonal array method is simple and easy to visualize the relation of the variables by tabulating the combination of control variables. We use Taguchi's factorial orthogonal array method to compare and select the geometric variables within the given ranges

The range of control variables:

OD: 19 – 25 mm

Thickness: 2 – 6 mm

Leg Angle: 12 - 30 degrees

Table 4. Taguchi's factorial orthogonal array

OD = [20 23 25] (mm)
Thickness = [4 5 6] (mm)
Leg Angle = [20 25 30] (degree)

		OD1			OD2			OD3	
	T1	T2	T3	T1	T2	T3	T1	T2	T3
LA1	**1**	**1**	**1**	**1**	**1**	**1**	**0**	**1**	**1**
LA2	**1**	**1**	**1**	**4**	**1**	**1**	**3**	**1**	**1**
LA3	**4**	**1**	**1**	**4**	**4**	**1**	**4**	**4**	**4**

OD = [20 23 25] (mm)
Thickness = [2 3 4] (mm)
Leg Angle=[12 15 17] (degree)

		OD1			OD2			OD3	
	T1	T2	T3	T1	T2	T3	T1	T2	T3
LA1	**0**	**0**	**1**	**0**	**0**	**0**	**0**	**0**	**0**
LA2	**0**	**1**	**1**	**0**	**0**	**0**	**0**	**0**	**0**
LA3	**0**	**1**	**1**	**0**	**0**	**0**	**3**	**0**	**0**

OD = [19 20 21] (mm)
Thickness = [2 2.25 2.5] (mm)
Leg Angle = [12 13 14] (degree)

		OD1			OD2			OD3	
	T1	T2	T3	T1	T2	T3	T1	T2	T3
LA1	**0**	**0**	**0**	**0**	**0**	**0**	**0**	**0**	**0**
LA2	**0**	**0**	**0**	**0**	**0**	**0**	**0**	**0**	**0**
LA3	**0**	**0**	**1**	**0**	**0**	**0**	**0**	**0**	**0**

There are three control variables for the orthogonal array. OD is the outer diameter (mm), T is the thickness of a unit (mm), and LA is the leg angle (degree). We define an error index E_i (i=1 and 2) so that we can evaluate the state of array outputs. If the control variables pass the clearance condition expressed by equation (17), then E_1=0. Otherwise, E_1=1. If the control variables pass the contact ability condition, then E_2=0. Otherwise, E_2=3. The clearance and the contact ability condition are mentioned as design requirements in Chapter 3.1. The output of the orthogonal array is a sum of E_1 and E_2 so that we can consider which control variables violate the conditions. Three tables of orthogonal arrays cover high, middle, and low range of control values. From the three tables, the last table shows the best result. The clearance is found from the geometry of Figure 10 and is expressed on Equation (17).

$$clearance = \left(\frac{OD}{2} - t\right)(\cos\alpha + 1) - \sin\alpha\sqrt{OD \times t - t^2} \tag{17}$$

Because the first sharp curve of sigmoid colon has about 25.4 mm (one inch) radius of curvature, we define 25.4 mm as the objective radius of curvature. Based on this curvature, we can determine the "effective length" of each unit. We define the effective length as the maximum length of the unit, tangent to the objective radius of curvature, which will allow the necessary freedom of rotation or bend in the exoskeleton structure. If the actual length of the unit is longer than the effective length, the exoskeleton structure cannot bend enough to meet the objective radius of curvature. The unit length can be shorter than the effective length. However, if the units are much shorter than the effective length, the cable will lose more force when the exoskeleton structure bends. In other words, the effective length is also constrained by the minimum length that will still allow the

cables to exert effective force on the units. Therefore, effective length of the unit is a dependent variable and is a function of leg angle. Effective length is also directly related to the number of units in a given length of the exoskeleton structure, the cable angles, and the loss of cable forces.

Figure 12 shows the effective length of unit for the objective radius of curvature.

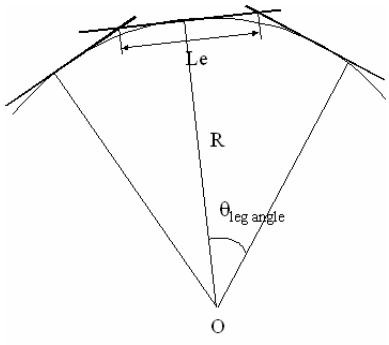

Figure 12. Objective radius of curvature and effective length of unit

The effective unit length for a given radius of curvature can be calculated by the equation below with the selected value of the leg angle 14 degrees.

$$Le = 2R\tan\left(\frac{\theta_{leg\ angle}}{2}\right) \tag{18}$$

where,

Le: Effective length of unit

R: Radius of curvature (25.4 mm)

Le=6.24 when leg angle is 14 degrees.

To find relations of the geometric control variables, we made Table 5, and compared each control variables. We defined that if the geometric variable varies along x or y direction, we called it x or y directional variable. A x-y variable can affect both x and y directions. The x and y directional variables are orthogonal to each other, and can be treated as independent variables. (A change of x directional variables can not affect y directional variables.) Delta and Le are x directional variables, and OD and T are y directional variables. LA is a x-y directional variable.

Table 5. Relations of geometric control variables

	delta(x)	Le(x)	OD(y)	T(y)	LA(x-y)
delta(x) ↑		↑	X	X	↑
Le(x) ↑	↑		X	X	▲
OD(y) ↑	X	X		▲	↑
T(y) ↑	X	X	▲		▲
LA(x-y) ↑	↑	▲	↑	▲	

Where,

Delta(x): A location of cable holder (x direction)

Le(x): Effective length (x direction)

OD(y): Outer diameter of the unit (y direction)

T(y): Thickness of the unit (y direction)

LA(x-y): Leg angle (x-y direction)

For the dependent variables,

▲ : Increment (verified relation by an equation or geometry)

↑ : Increment (maximum range)

There is no relation among independent variables.

X : No relation (Independent variable)

We found direct relations of dependent variables from the geometric constraints and design requirements. From the clearance condition in equation (17), OD and T have the dependent relation. We can increase OD and T within the allowance of equation (17). Le and LA are also dependent variables to each other, and equation (18) shows the relation. From the geometric relations of LA and T, we can determine the upper boundary of delta. The brief summary of conditions and dependent variables are following:

- Clearance condition : OD and T
- Objective radius of curvature : Le and LA
- Geometric relations : delta and LA , delta and T

With the defined relations of geometric dependent variables, we can change the dimension of the unit for the needs of new design requirements.

4.2 Resulting Configuration of a Pair of Exoskeletal Units

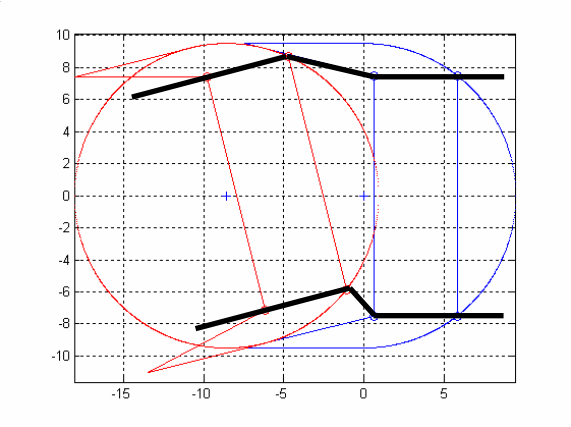

OD=19 mm
T=2 mm
LA=14 degrees
Alpha_max = 14 degrees
Lc = 8.57 mm
Le = 6.24 mm
Clearance = 13.37 mm

Alpha = rotation angle between units

Figure 13. Configuration of two units

Based on the analysis in the previous section, we are able to determine the optimal configuration, or physical dimensions of the unit: outer diameter, thickness, length, and leg angle. From the last row of Table 4, the optimal geometrical parameters were selected. A schematic of two optimally shaped units is presented in Figure 13. The small 'o' marks on the first and second units are the locations of cable holes or attachment sites. Two bold lines depict the cables.

Geometric analysis determined that the outer diameter needs to be small (19mm), and the units should be thin (2mm). The smaller the leg angle, the more units will be needed to achieve a given radius of curvature. In other words, a larger leg angle decreases number of the units required to achieve the needed bend. The optimal leg angle is 14 degrees. We also observe that the effective length of the unit

(6.24mm) is substantially less than the outer diameter of the unit for our selected geometric variables.

4.3 Checking the Friction Coefficient

In order to find the range of cable forces that can satisfy the locking condition between two units, we analyze the possible combinations of cable forces and check their corresponding friction coefficient. The required friction coefficient μ for locking is a function of forces and geometric variables. From the geometry of Figure 13, we vary the two cable forces and plot the friction coefficient from zero to 0.2. In this case, the material used to manufacture the unit is assumed to be aluminum, and the maximum friction coefficient between two units is 0.2. From the geometrical characteristics, the maximum possible rotation angle between two units is alpha_max = 14 degrees.

Figure 14 plots two cable forces and the required friction coefficient. F_1 is the upper cable and F_2 is the lower cable in Figure 14. Figure 14 B is the top view of Figure 14 A. Because the rotation angle alpha is non-zero, it is asymmetrical with respect to the line that two cable forces have the same values (F_1=F_2). We can say that the unit can have a locking ability if the value of the friction coefficient is in the region defined by valid values of F_1 and F_2. When the two forces are equal, the friction coefficient is between 1.0 and 1.5 for the given geometry; and a minimum required friction coefficient is found to be 0.114.

Table 6. Legend of the friction coefficient

Brightness	Required friction coefficient
Lightest	0.15 – 0.2
Medium	0.1 – 0.15
Light	0.05 – 0.1
Darkest	0 – 0.05

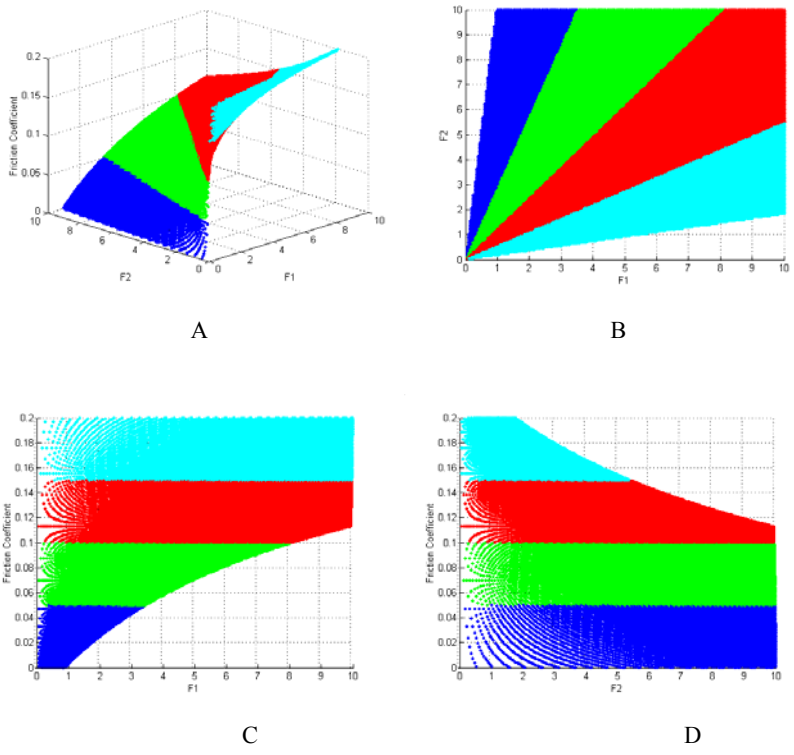

Figure 14. The relation between friction coefficient and cable forces. Figure 14 B, C, and D are two-dimensional projected views of the same plot

When the values of two cable forces F_1 and F_2 are located anywhere in the shaded section of Figure 14 B, the cable will have locking ability. Since each material has a different friction coefficient, we should re-consider the ranges of forces that satisfy the locking ability for the possible change of materials.

4.4 Cable Angles as a Function of the Unit Rotation

Rotation between two units changes cable angles, and it affects the loss of cable forces. Figure 15 shows the relation between the change of rotation angle and upper and lower cable angles. The cable angles θ_{u1}, θ_{l1}, θ_{u2}, and θ_{l2} represent angles of upper and lower cables from Figure 13. When the segment rotation angle alpha varies from zero to fourteen degrees (CCW), the upper cable angles of θ_{u1} and θ_{u2} are greater than lower cable angles of θ_{l1} and θ_{l2}. From equation (16), the loss of cable force due to the friction between the cable and the unit surface is a function of cable angles. The increasing value of rotation angle will lessen the upper and lower cable forces. If the rotation angle alpha is zero, two units are consecutively straight and all cable angles have zero values.

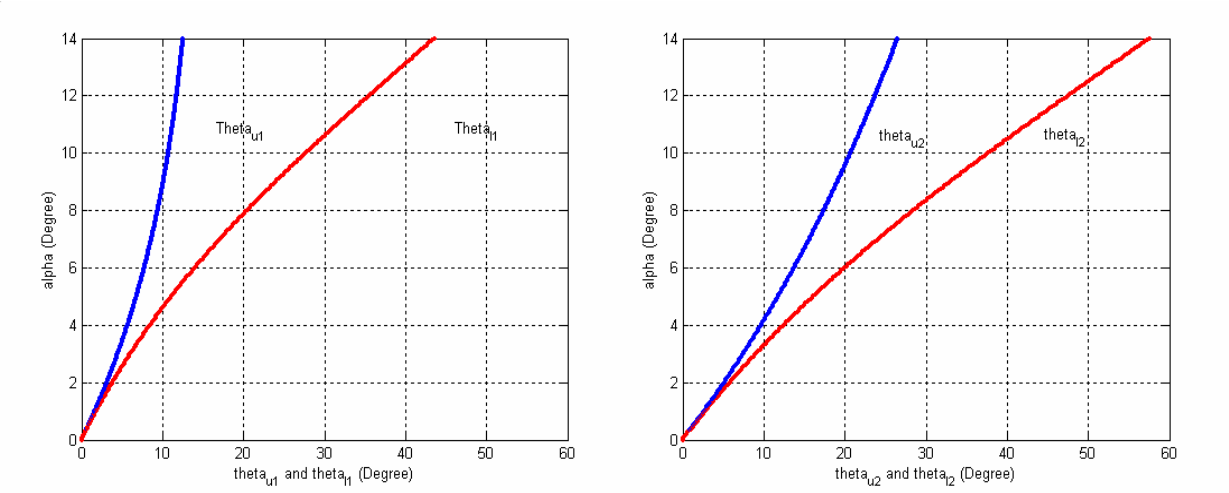

Figure 15. Change of upper and lower cable angles vs. rotation angle of alpha

4.5 Locating the Cable Holders

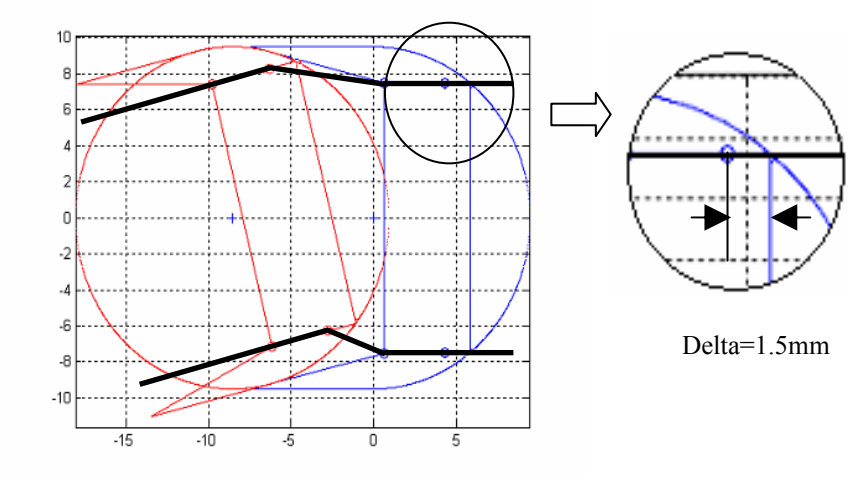

Figure 16. Configuration of two units and delta (1.5mm)

Now we approach the question of where to attach the control cables on each unit. From Chapter 4.4, we find that the cable angle is a function of rotation angle of the units; cable angle is also directly related to cable forces. By adjusting the location of cable holders or attachment sites, we can change the rotation angles between the units. By locating the two cable holders at the unit head, we hope to minimize the loss of cable forces and prevent kinks in the cables. In order to evaluate the optimum location of cable attachments, we assign the variable delta as the distance from the unit head to the first cable holder site. Then we assess how various values for delta affect cable forces along the chain of linked units. Figure 16 shows an example value of delta of 1.5 millimeter. The selected geometrical values from Table 4 are used to find the maximum and minimum delta. In this geometric case, the range of delta can be from zero to five millimeters. If the cables in Figure 16 have a finite diameter, a possible kink can be happen at the junction of beginning

and ending parts of the cable holes. The minimum bending radius of the cable should be considered to avoid the possible kink of the cable.

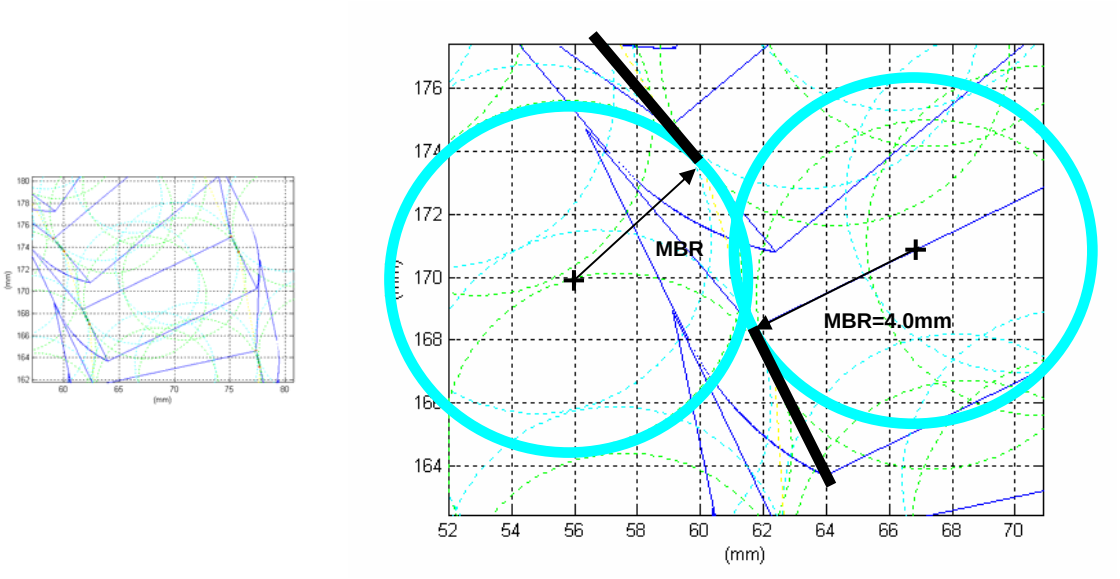

Figure 17. Required minimum banding radius for a cable

The left side of Figure 17 shows the maximum rotation with respect to each unit and the cable diameter is disregarded. The right figure is a magnified view with a single cable and dashed circle of a minimum bending radius. The center points of minimum bending radius circles are perpendicular to the cable at the beginning and end of cable constraints. We consider two minimum bending radius circles with two segments of cables (bold lines) for the maximum cable tension. If two minimum bending radius circles are overlapped, we consider that the cable is kinked. In the case of the stranded stainless steel cable, which cable diameter is 1/32 inch (0.79mm), the minimum bending radius is 0.155 inch (3.94mm), and the cable can be used for the geometry of Figure 16.

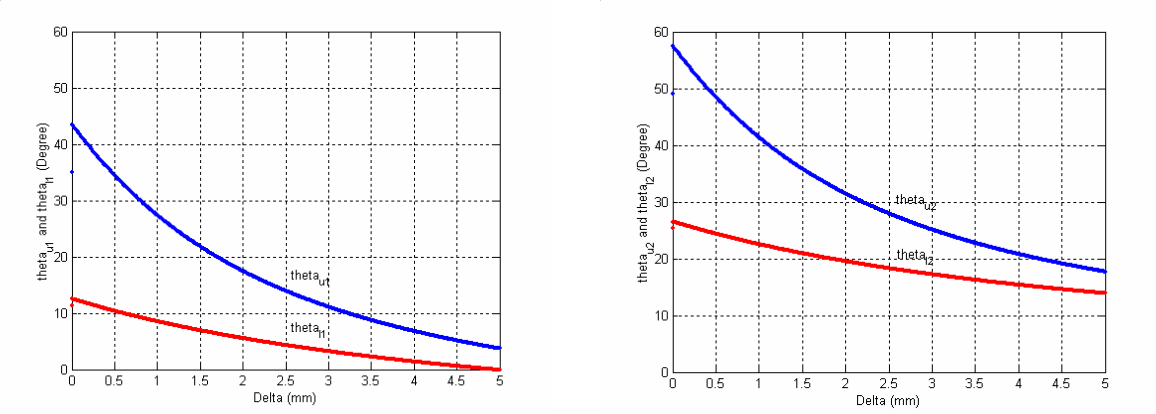

Figure 18. Change of upper and lower cable angles vs. delta

Figure 18 represents the relation between delta and cable angles. The maximum delta can achieve the minimum value of the upper and lower cable angles. By selecting the value of delta, the position of the first upper and lower cable holders can be moved to increase or decrease the cable angles θ_{u1}, θ_{l1}, θ_{u2}, and θ_{l2}. We can compare the cable angles when delta is zero and five. When delta is zero, the cable angles θ_{u1}, θ_{l1}, θ_{u2}, and θ_{l2} are 43.8, 13.2, 57.7, and 26.5 degrees. When delta is equal to five, the cable angles are respectively decreased to 4.2, 0.8, 17.4, and 14.8 degrees. From the previous chapter, we showed that decreasing value of cable forces is smaller at low values of cable angles than that of large value of cable angles.

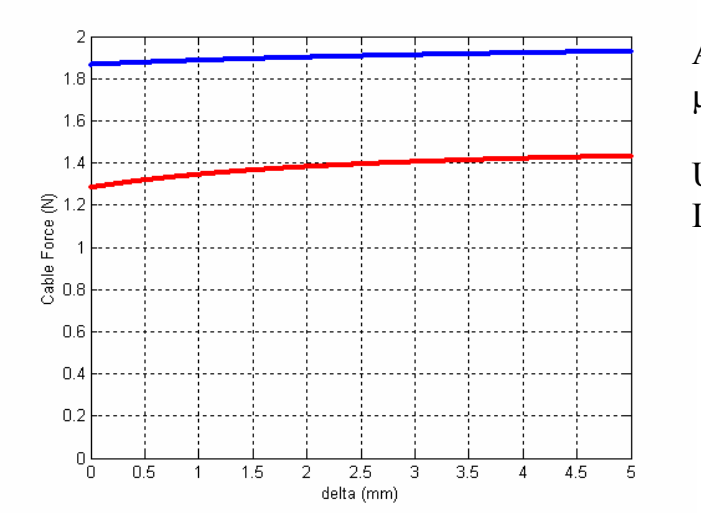

Alpha = 14 degree
$\mu_{cable} = 0.15$

Upper cable force: $F_1 = 2.0$ N
Lower cable force: $F_2 = 1.5$ N

Figure 19. Change of delta vs. cable forces

Figure 19 shows the change of delta versus upper and lower cable forces on the fixed rotation angle. The cable forces F_1 and F_2 begin with practical values of 2 and 1.5 N. When delta equals zero, the cable forces are decreased from the original values of 1.89 and 1.29 N. When delta is five, two cable values are 1.93 and 1.42 N. As the value of delta increases from zero to five, upper and lower forces increase and approach their original values. As long as the rotation angle of alpha is greater than zero, cable forces decrease and we can minimize the loss of cable forces by selecting the optimal value of delta. When delta is five, we can achieve the minimum loss of cable forces.

4.6 Conclusion for Chapter 4

This chapter presented the preliminary design of an exoskeleton structure that includes an analysis of geometry and the cable forces. We checked the locking ability between two units by calculating a required friction coefficient. From static modeling, we derived equations for cable forces and the closed form solution of the required friction coefficient. We found the range of cable forces that is suitable for sustaining the locking ability between two units. Using Taguchi's factorial orthogonal array method, we selected the optimal geometric values for the given design requirements. By adjusting the location of cable holes at the unit head, we can also minimize the loss of cable forces.

Based on the geometry and force analysis, we will next model a configuration of a human colon and simulate our exoskeleton structure model. We will find force variables that can satisfy the required friction coefficient. After we have the force variables, we will analyze the detailed relations of force variables, delta, and the friction coefficient. An analysis of external forces on the exoskeleton structure will be performed.

5. Simulation in the Curvature of a Human Colon

In Chapter 5, we tested which physical dimensions of the units would best accommodate the curves of the human colon. We also analyzed cable forces and friction coefficients between units to confirm that the unit could be locked for increased maneuverability. In order to prevent kinking and loss of cable force, we modeled cable attachment locations.

With the exception of accommodating the angle of the sigmoid colon, all the previous modeling and design work dealt with the internal workings of the exoskeleton structure. In the present chapter, we will simulate the exoskeleton structure operation with and without the external forces placed on the exoskeleton structure by the surrounding human colon. We will examine how these forces affect locking ability and cable forces. Thus we can be more confident that the exoskeleton structure will function properly when built and tested in an actual colon.

5.1 Simulation without External Forces

5.1.1 Test of the Kinematic Model

Chapter 4 described the exoskeleton structure design decisions that were made based on 2-unit models. Now we create a 10-unit model to test those designs, though still without external forces. We test the kinematics of the exoskeleton structure to verify that it will be able to bend and lock as needed outside the colon,

before we add to the simulation the more difficult case of countering forces from the colon.

To validate the model and the dimensions selected in Chapter 4, we choose three basic configurations of the exoskeleton structure: straight, simple curved, and combined or S-curved configurations. To observe the variation of the friction coefficient and cable forces, we create a model that consists of ten units. In Figure 20 and 22, the two bold lines depict the cables. The straight and curved configurations are overlapped in Figure 19. The cable forces are F_1 for the left side and F_2 for the right. In this case, no mathematical solution of the required friction coefficient exists. Although it is impossible to solve the closed form solution of the required friction force, a system can still have locking ability.

Now we ask, if F_1 and F_2 are unequal, do the resulting friction coefficients allow the exoskeleton structure to stay straight? To answer this, we test a ratio of cable forces. For example, given F_1=2 N and F_2=1 N (or vice versa), we solve each unit's friction coefficient and cable force for the straight configuration on Figure 19. Because of zero rotation angles, there are no losses of cable forces and the friction coefficient is the same through all ten units, i.e. 0.06. In other words, the cable can stay straight and locked. However, if the ratio of F_1:F_2 is greater than three, then the exoskeleton structure cannot stay straight and locked. The forces on the left side overcome the friction coefficients on the right side, and the cable bends to the left, in the direction of F_1.

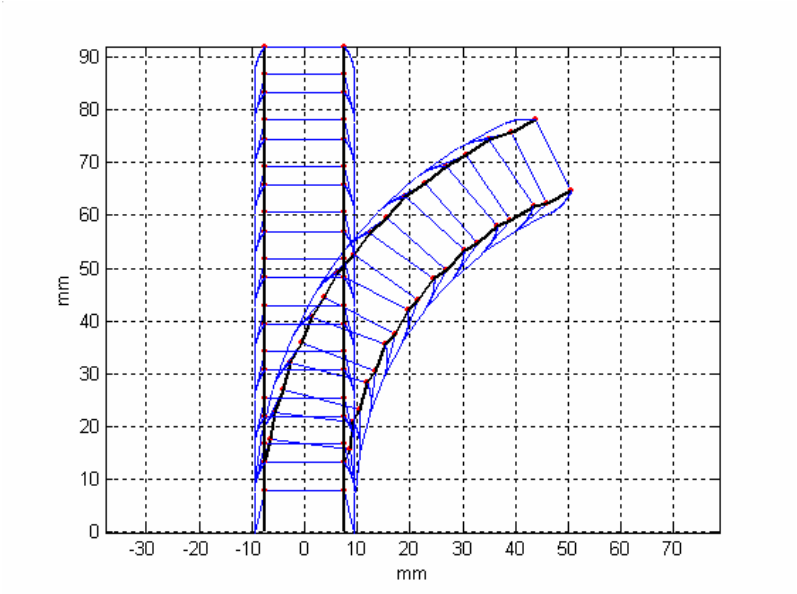

Figure 20. Straight and curved 7-degree configuration

The straight configuration is obtained by applying zero rotation angles to each unit. When the same cable forces (F_1=F_2) are applied to the exoskeleton structure, no mathematical solution of the required friction coefficient exists. Although it is impossible to solve the closed form solution of the required friction force, system can still have a locking ability. If the ratio of two cable forces is bigger than three, the exoskeleton structure cannot maintain the straight configuration. We apply the cable force of F_1=2 N and F_2=1 N and vice versa. We can solve each unit's friction coefficient and cable force for the straight configuration on Figure 20. Because of zero rotation angles, there are no losses of cable forces and the friction coefficient is the same through all ten units.

In the curvature of a human colon, the second curve of a sigmoid colon is 7 degrees. Figure 20 shows the ten model units curved to 7 degrees. Now we analyze the change in friction coefficients to check the locking ability of each unit.

The corresponding cable forces are shown in Figure 21. Passing from the first to the tenth unit, the friction coefficient increases linearly. Curved configurations can provide the different radius of curvature to each cable and a loss of cable forces is also different. More radius of curvature causes more loss of force. According to the geometry of the unit, 14 degrees is the maximum rotation angle that the unit can make. This meets the requirements of passing through the first sharp curve of the sigmoid colon.

According to the geometry of the unit, 14 degrees are the maximum rotation angle that the unit can make, and the units must have the rotation angles of 14 degrees to make the first sharp curve of the sigmoid colon. Moreover, we want to check the changes of the friction coefficient at the junction where the direction of the rotation angle is reversed. Next we examine the effects of bending the unit in an S-curve. This mimics any section in the colon that turns first one way, and then another. We made the S-curved configuration by taking the rotation angle of +14 degrees from the first to fifth unit and -14 degrees from the sixth to tenth unit. The combined curved configurations are shown in Figure 22.

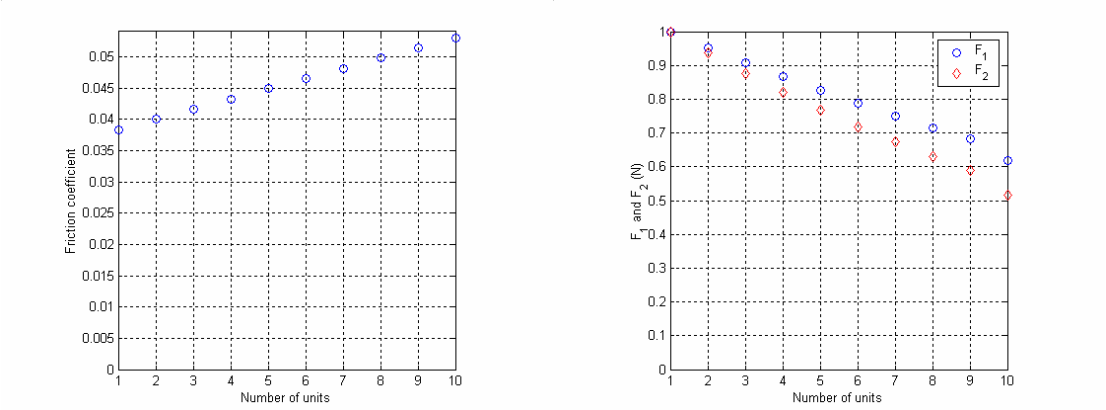

Figure 21. Friction coefficient and cable forces for the curved configuration

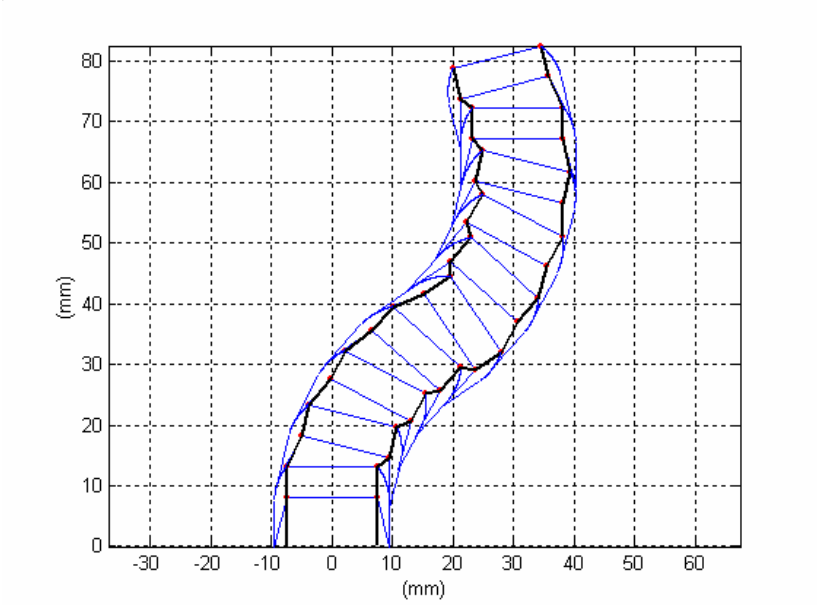

Figure 22. Combined curved configuration at 14 degrees per unit

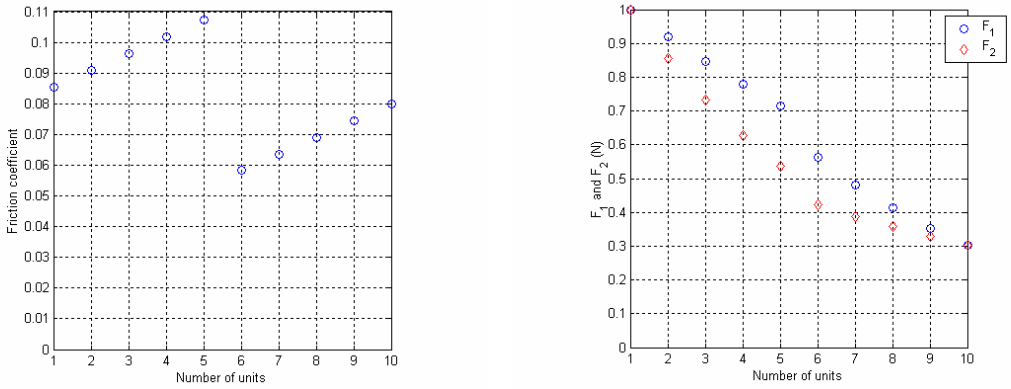

Figure 23. Friction coefficient and cable forces for the combined curved configuration

We apply the same cable force (F_1=F_2) and the change of cable forces for each unit to create Figure 23. Because of the different radius of curvature, the loss of force is different for each unit. There is a sudden drop in the friction coefficient between the fifth and sixth units because of the changing direction of the rotation angle. For these particular configurations, the cable forces at the tenth unit are the same due to the force compensation in an S-curve. In other words, we can conclude that if the initial cable forces are the same and the sum of all rotation angles is zero (as in the 10^{th} unit), the final cable forces are identical. The cable forces should equal whenever the left and right curves involve the same angle over the same number of units. There is a linear (geometric path conservative) result about the loss of forces for the symmetric configurations but the locking characteristics of the friction coefficient is different. We will see more details about the characteristics of friction coefficient and cable forces in next section.

5.1.2 Simulation in a Human Colon-Like Curves

Now that we have examined the cable forces and friction coefficients acting on the units given straight, simple curved and combined curved shapes, we proceed to a more complex, sigmoid colon-like series of curves. In the first simulation, the model only approximates a curving human colon might have on an inserted exoskeleton structure. (Note that the model still does not account for external forces from the colon, which will be discussed in Section 5.2.) We also simulate different values of delta (the distance between the distal end of a unit and the cable attachment).

We chose the geometric variables from the orthogonal array and determined the relation between two cable forces and the friction coefficient. We tested the unit

model and showed how the friction coefficient varied for each unit along the simple configurations. However, the cable attachment offset delta (see Figure 24) is another variable that affects the upper and lower cable angles and the loss of cable force. It is straightforward to determine from the geometry of the unit that the maximum varying friction coefficient to lock varies with delta.

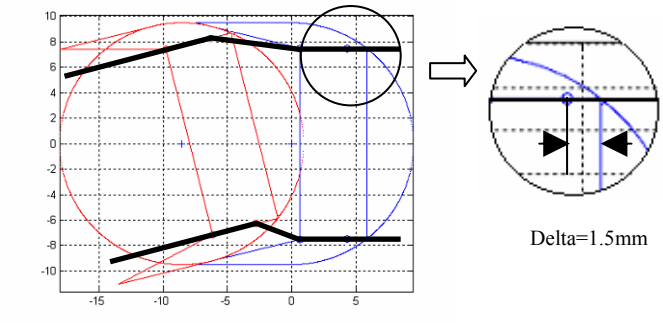

Figure 24. Configuration of two units and delta (1.5mm)

We developed a simulation program to find out the variables that can satisfy the friction coefficient 0.2, which is required for locking. After we have the sets of variables, we can identify the relations of force variables, delta, and friction coefficient. We consider that there are no external forces on the units for this first analysis. The simulation with external forces will be followed on Chapter 5.2.

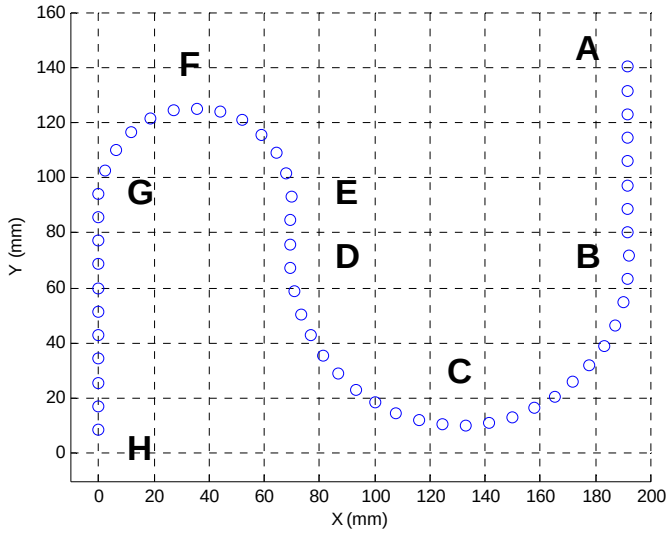

Figure 25. Simulation of curvature for sigmoid colon

The unit starts from point H and ends at point A. At point H, cable forces F_1 and F_2 are applied on the left and right sides of the unit and the direction of the cable force is opposite to the vertical axis (point G to H).

A brief description of the pseudo code is as follows:

- Define the geometrical constraints such as R, OD, t, and leg angle that are already selected from Taguchi's factorial orthogonal array.
- Set the range and step size of input variables (F_1, F_2, and delta).
- Load the rotation angles and length for the configuration of a human colon.
- Compute and compare the friction coefficient that is function of F_1, F_2, and delta.
- If it satisfies the key condition ($0 <$ friction coefficient ≤ 0.2), save the array sets.

```
Define the geometric_constants such as R, OD, t,
and leg angle
 for delta=0 : 1 : 5,            % location of cable holder
    for F1=0 : 1 : 10,           % upper cable force
        for F2=0 : 1: 10,        % lower cable force
            load (length, angle)
                                 % for all  58 units
            mu (F1,F2,delta,geometric_constants)
            if 0<mu≤0.2
            save all data : F1, F2, delta, and mu
            end
        end
    end
```

Figure 26. Pseudo code of a simulation of curvature for a human colon

According to the structure of the unit, the range of delta is 0 to 5mm with a 1mm step size. For the cable force, we set the step size to 0.1 for the purpose of a graphic display and analysis of results.

Table 7. Output variables with delta

Delta	0	1	2	2.7
Area percentage on F_1-F_2 plane (%)	6.89	4.04	4.48	2.22

Table 7 shows the valid operating range for locking of all 58 units. (Reaching the end of the sigmoid colon requires 58 units.) Percentage of area on the F_1-F_2 plane means the possible combination of two cable forces hold a locking ability. For all

values of delta, area percentages on the F_1-F_2 plane have the similar values to each other. We have found that delta has a practical limit of 2.7 mm. The average of friction coefficient is decreases as delta goes from zero to 2.7 mm.

Figure 27 represents the relation between cable forces and the required friction coefficient for delta values of zero (A), 1 mm (B), 2 mm (C), and 2.7 mm (D). When delta is zero, friction coefficients are stacked without vertical discontinuity. As delta goes from zero to 2.7, the friction coefficients (0~0.1) are slightly moving to the border of F_1=F_2.

At the region of $F_1 > F_2$, the key condition of simulation is not satisfied and no value exists. The reason is that for the input variables such as F_1, F_2 and delta, all 58 units have to satisfy the key condition. In other words, if only one unit out of 58 units did not pass the condition, data will be not saved and that unit cannot hold a locking ability. When F_1=F_2 and the configuration of units are straight, there is no closed form solution of the required friction coefficient and the friction coefficient is decreasing near F_1=F_2. In case $F_1 < F_2$, as F_1 is much bigger than F_2, the friction coefficient is approaching 0.1 for the low value of delta.

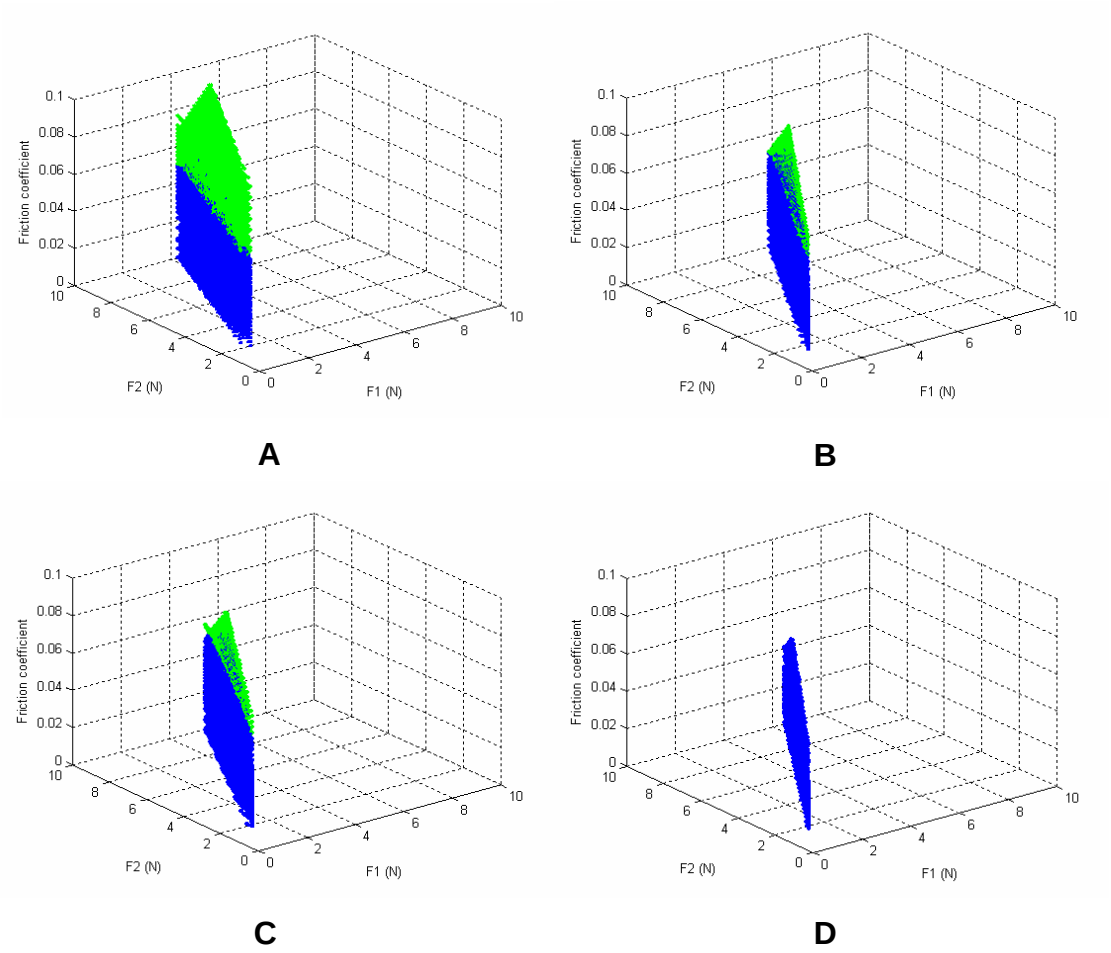

Figure 27. Cable forces vs. friction coefficient with varied delta. (A=0, B=1, C=2, and D=3)

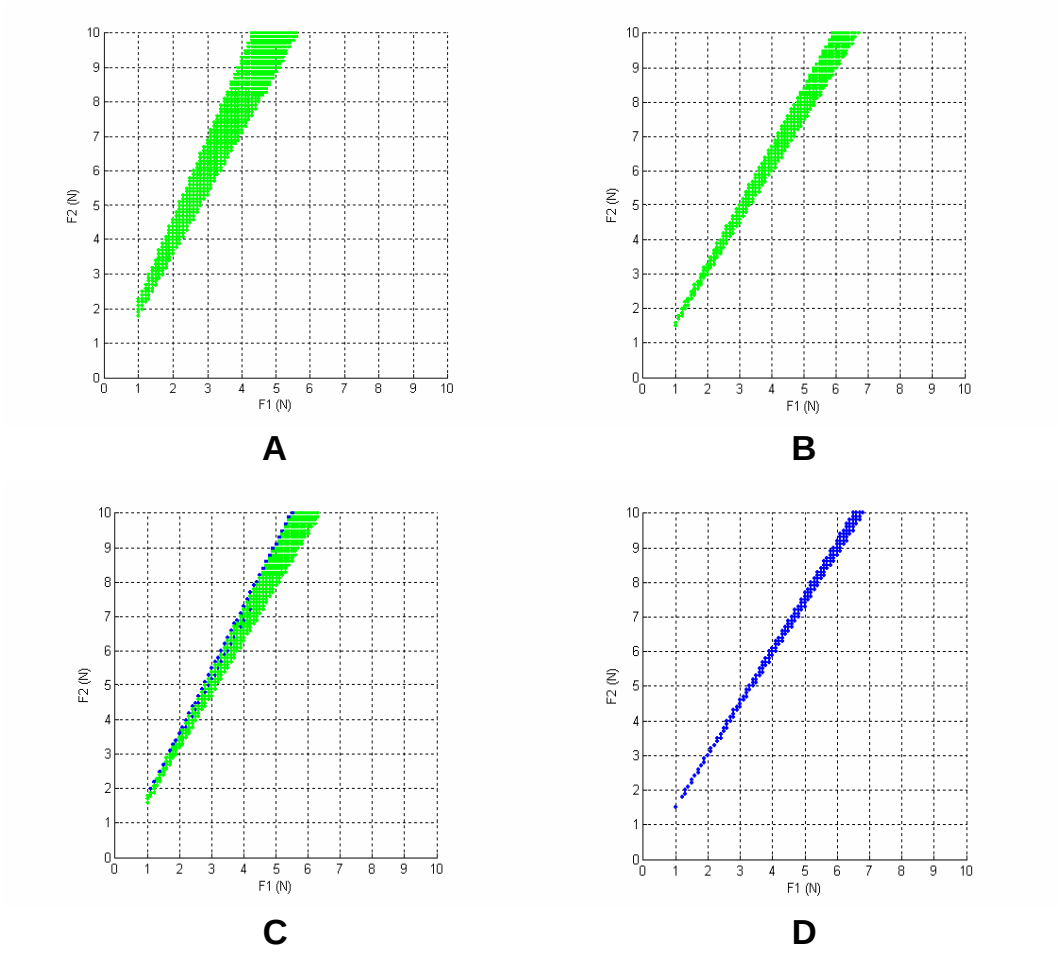

Figure 28. Cable forces vs. friction coefficient with varied delta on F_1-F_2 plane. (A=0, B=1, C=2, and D=2.7)

Table 8. Legend of Figure 27 and 28

Contrast	Friction coefficient
Light	0.05 – 0.10
Medium	0.00 – 0.05

5.1.3 Conclusion for Chapter 5.1

Based on the geometry and force analysis, we examined the simple configurations and modeled a configuration of a human colon and simulated our endoscope model. We found values that can satisfy the required friction coefficient and analyzed the relations of force variables, delta, and the friction coefficient without external forces. The exoskeleton structure will be stable if the combination of cable forces has a value of the friction coefficient.

For the cable control point of view, a cable control will be hard to be implemented for the narrow controllability of cable forces.

5.2 External Forces on the Curvature of a Human Colon

Now that we have determined the cable forces and friction coefficients acting on the units, i.e. resulting from the cable and unit interactions when straight or curved, we can begin to model how external forces affect the exoskeleton structure. To analyze the external forces on the exoskeleton structure, we can treat the exoskeleton structure as a retractor. The main function of a retractor is to hold or retain a designated tissue or organ, and most of the forces will be located at the end of a retractor. In this case, we consider a self-retaining, flexible retractor with a base. Two external forces represent the loads at the end of the flexible retractor in Figure 29. From the simulation program with external forces, we have the appropriate variables. We can identify the relationships between the force variables, the friction coefficient, and the location of cable holders (delta) on Figure 24. By the value of a delta, the cable angles θ_{u1} and θ_{l1} will be decided and minimum values of the cable angles will minimize the loss of cable forces [1].

There are two required conditions when external forces are considered in the simulation. The first is the same as for the case of no external force [18], where the required friction coefficient has to be greater than zero and less than or equal to 0.2. The second condition is that since the required friction coefficient is a function of an external moment, the external moment applied to each must meet the friction coefficient requirement. The calculated external moment is the maximum external resisting moment.

Figure 29 shows an abstracted curvature simulation for a human colon, with external forces *P* and *F* applied to the units at point A. (*P* is axial force *P* and *F* is lateral force.) The moments caused by the external forces *P* and *F* are shown in Table 9. The total number of units is 58; the first unit starts at point H and the last

ends at point A. At point H, cable forces F_1 and F_2 are applied to the first unit on the left and right sides, respectively. The direction of the cable force is opposite to the vertical axis (in the direction from G to H).

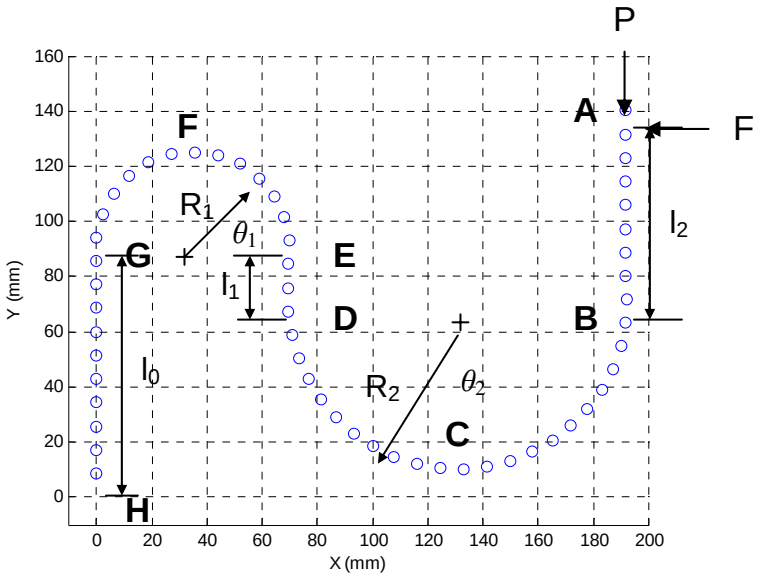

Figure 29. Simulation of curvature for a human colon with external forces

Table 9. Moment for each interval of curvature

Interval	Moment [caused by P] (N-mm)	Moment [caused by F] (N-mm)
A - B	0	F s $(0 \le s \le l_2)$
B - D	$P R_2 (1 - \cos \theta_2)$ $(0 \le \theta_2 \le 180$ degrees)	$F l_2 + F R_2 \sin \theta_2$ $(0 \le \theta_2 \le 180$ degrees)
D - E	$2 P R_2$	$F l_2 - F s$ $(0 \le s \le l_1)$
E - G	$2 P R_2 + P R_1(1 - \cos \theta_1)$ $(0 \le \theta_1 \le 180$ degrees)	$F (l_2 - l_1) - (F R_1 \sin \theta_1)$ $(0 \le \theta_1 \le 180$ degrees)
G - H	$2P R_2 + 2P R_1$	$F (l_2 - l_1) + F s$ $(0 \le s \le l_0)$

```
Define the geometric_constants such as R, OD, t, and leg
angle

for delta=0 : 1 : 5,            % location of cable holder
 for F1=0 : 1 : 10,             % upper cable force
  for F2=0 : 1: 10,             % lower cable force
   for P=0 : 0.0335 : 0.335,    % external force (axial)
    for F=0 : 0.0335 : 0.335,   % external force (lateral)

% for all 58 units
load (length, angle)            % shape of a colon

      required_moment(F1,F2,friction_coefficient,unit_number,..)
external_moment (P,F,unit_number,geometric_constants)
mu (F1,F2,delta,external_moment,geometric_constants)

if 0<mu ≤ 0.2 & external_moment ≤ max_resisting_moment
save all data : F1, F2, delta, P, F, mu, and external_moment
end

    end
   end
  end
 end
end
```

Figure 30. Pseudo code of simulation with external forces

If the sum of two external moments caused by the force P and F is less than the maximum external resisting moment, then the system will be stable and have a locking ability. We saved the satisfied variables, which satisfy the two required conditions to analyze the relationship between the variables such as cable forces, friction coefficients, and delta. The pseudo code of the simulation is shown on Figure 30, and its description is outlined below:

- Define the geometric constants (such as R, OD, t, and leg angle) that are already selected from the external-force-free model.
- Set the range and step size of input variables (delta, F1, F2, P, and F)

- Load the data of curvature shape.
- Compute the maximum external resisting moment, the external moment caused by P and F, and the friction coefficient.
- If it satisfies the first condition (0 < friction coefficient ≤ 0.2) and second condition (external moment ≤ maximum external resisting moment), save the variable sets.

In Figure 30, the maximum range of external forces P and F is manually decided by a trial and error method, and Figure 31 depicts the example of the maximum value external force P and F for a fixed delta.

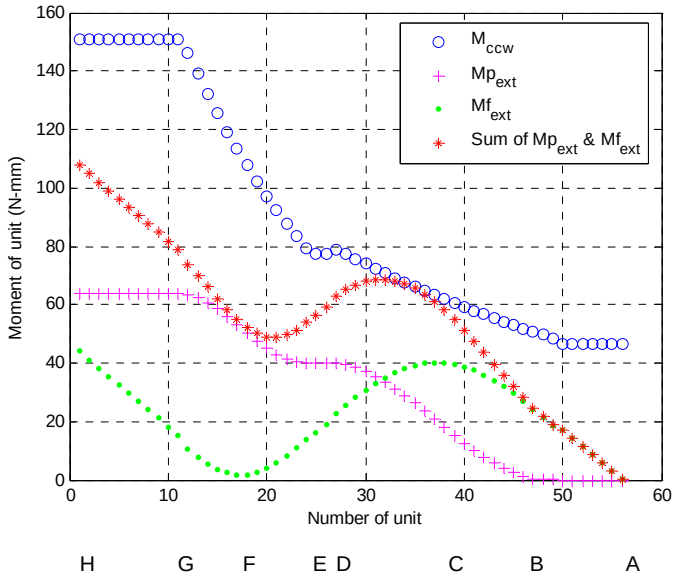

Figure 31. The second required condition of simulation: external moment ≤ maximum external resisting moment

Figure 31 shows one example case of the second required condition. The characters A through H below the graph represent locations along the endoscope stem in Figure 31. M_{ccw} represents the maximum external resisting moment in the CCW direction. Mp_{ext} and Mf_{ext} are the moments caused by an axial force P and a lateral force F. From Figure 31, M_{ccw} is always larger than the sum of Mp_{ext} and Mf_{ext} from the first to 58th unit (point H to A) to maintain the stability from the external forces P and F. We select the maximum values of the input variables to demonstrate the clear difference between M_{ccw} and the summation of Mp_{ext} and Mf_{ext}. for the constant value of delta. The input and geometric variables for the simulation on Figure 31 are as follows:

```
% Input variables
F1 = 10                  % Upper cable force (N)
F2 = 10                  % Lower cable force (N)
P = 0.335                % External axial force (N)
F = 0.335                % External lateral force (N)
delta = 5                % Position of the cable holder (mm)

% Geometric variables
OD = 19                  % Outside diameter (mm)
t = 2                    % Thickness of the unit (mm)
theta = 14               % Leg angle (degree)
R = 25.40                % Radius of curvature (mm)
lt = 2×R×tan(0.5×theta)  % Effective leg length (mm)
ltt = 8.57               % Length between centers of the units (mm)
```

Input values for the simulation with external forces are shown on Table 10. To determine the force range of the cables, we considered the control aspect of the cables, and assumed that the ratio of two cable forces will not exceed ten and we set the range of the two cable forces as one to ten. The range of delta, which is the distance of the cable holder, is from zero to five mm. From the geometry of the unit, the maximum value of delta is five.

Table 10. The range of input variables and step size

Input variables	Range (min. to max.)		Step size
F1 (N)	0	10	1
F2 (N)	0	10	1
P (N)	0	func(delta)*	0.1xfunc(delta)*
F (N)	0	func(delta)*	0.1xfunc(delta)*
delta (mm)	0	5	1

On the Table 10, the value of func(delta) will vary with delta. See Table 11.

To determine the range of values used in the simulation, the maximum value of P and F were manually found by a trial and error method for different values of delta. If forces P and F have larger values than the upper range for a given delta, the second condition cannot be satisfied regardless of other input variables. Table 10 shows the range of external force P and F for different delta values. The upper ranges of external force P and F are almost proportional to the values of delta.

Table 11. Input range of external force P and F with the value of delta

delta (mm)	Range of P and F (N)
0	0 ~ 0.060
1	0 ~ 0.130
2	0 ~ 0.185
3	0 ~ 0.235
4	0 ~ 0.290
5	0 ~ 0.335

When input values satisfied the two conditions, input values and calculated variables were saved as output values for the purpose of analysis. Figure 32 to 37 are made with the output variables.

From Table 12, the percentage of points on the F_1 and F_2 plane varies with delta; the maximum and the minimum value are found at delta values of zero and five, respectively. Since all saved friction coefficients satisfy the required number of 0.2, we can calculate the average value and observe the change of values. The average of the friction coefficients is increased as delta increases. The average of the friction coefficients is less then 0.1, and it slowly increases as delta goes from zero to five. We check the average friction coefficient to find a possible correlation between the friction coefficient and the possible combinations of two cable forces. A high value of percentage of points on the F_1-F_2 plane indicates more possible combinations of the two cable forces. In other words, we have more possibilities from which to select the cable forces for the given colon curvature. When delta is

five, we can have the maximum combination of cable forces to retain the stability of the exoskeleton structure.

Table 12. Percentage of points on F_1-F_2 plane and average of friction coefficient with delta

delta (mm)	0	1	2	3	4	5
Percentage of points on F_1-F_2 plane (%)	29	38	40	45	49	52

Table 13. Legend of the friction coefficient on Figure 32, 34, and 36

Contrast	Range of friction coefficient
Dark	0.00 ~ 0.05
Medium	0.05 ~ 0.10
Medium dark	0.10 ~ 0.15
Light	0.15 ~ 0.20

Figures 32, 34, and 36 represent the three-dimensional graphs of the cable forces and friction coefficients. The gaps in the figures are for a step size of one. The small step size will make the plot look continuous. Figures 33, 35, and 37 show the relationship between the maximum external resisting moment and the sum of

the moment caused by external forces on each unit. As delta goes from zero to five millimeters for this example geometry, the maximum external resisting moment and the sum of moment caused by P and F are proportionally increased. On Figure 29 at the range of H to G (unit 1 to 19), the maximum external resisting moments have the same values in Figure 33, 35, and 37. This means that the initial straight section is insensitive to delta. The distal section A-B is very sensitive to delta and delta should be maximized for greatest resistance to applied external force. There are jumps at point G and D and they usually occur when the angle of unit changes from zero to a much higher value. As value of delta goes high, the magnitude of jump is decreased. A change in delta means that cable angles change with respect to the units, and the cable angles are reduced at high values of delta. From previous work, we found that the minimum value of the cable angle reduced the loss of cable forces and introduced maximum locking ability to the units. The same result can be applied for the case of applied external forces.

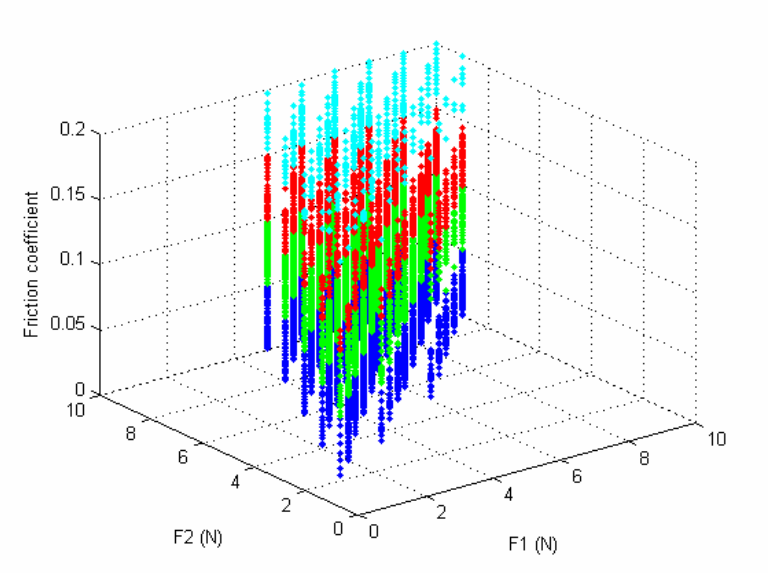

Figure 32. The relation between cable forces and friction coefficient when delta = 0 with external force P and F.

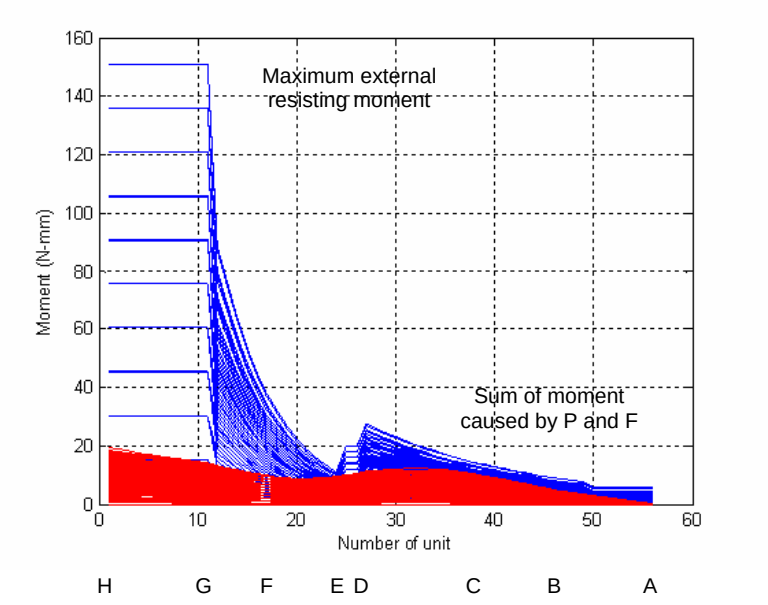

Figure 33. The maximum external resisting moment and sum of moment caused by external force P and F when delta = 0.

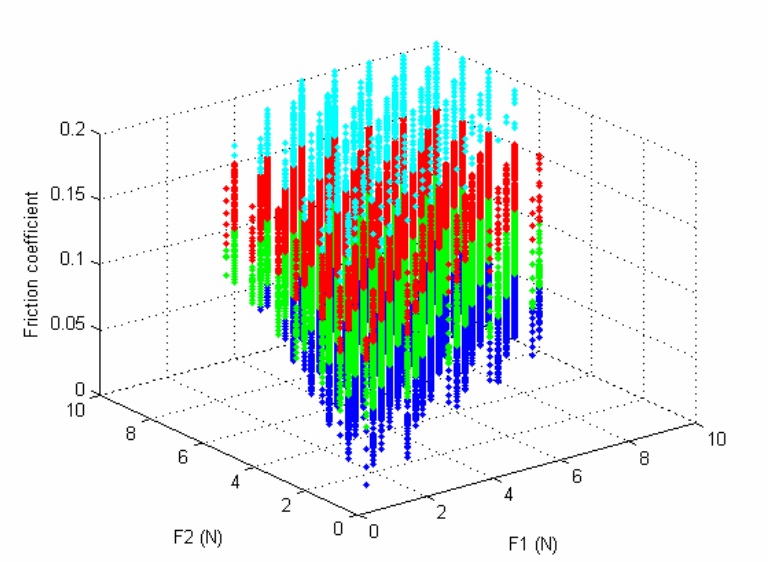

Figure 34. The relation between cable forces and friction coefficient when delta = 3 with external force P and F.

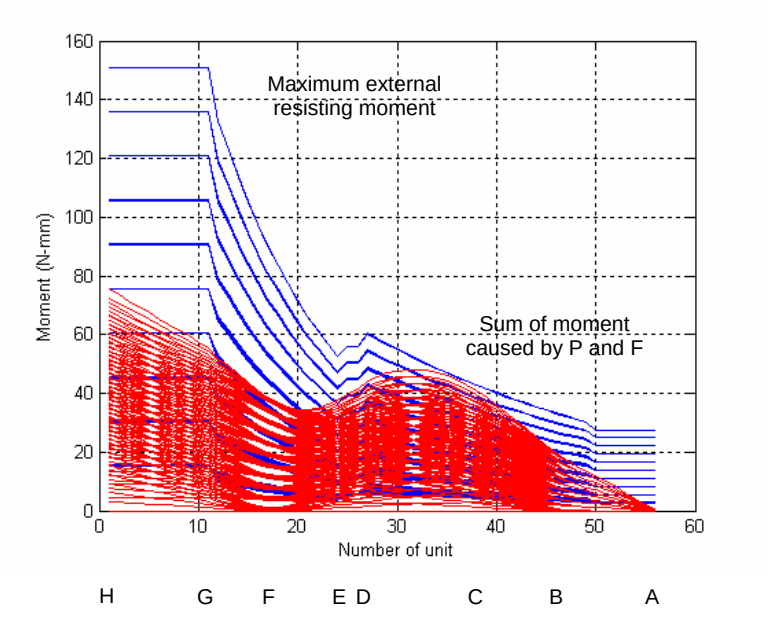

Figure 35. The maximum external resisting moment and sum of moment caused by external force P and F when delta = 3.

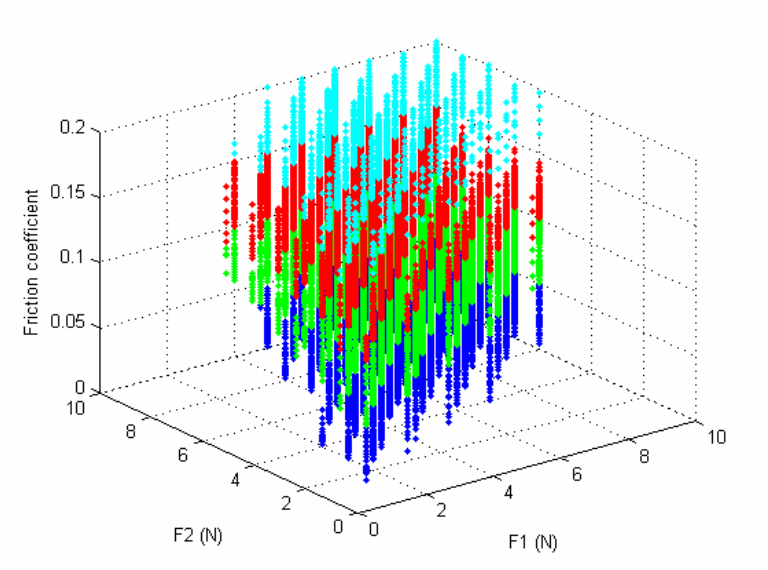

Figure 36. The relation between cable forces and friction coefficient when delta = 5 with external force P and F.

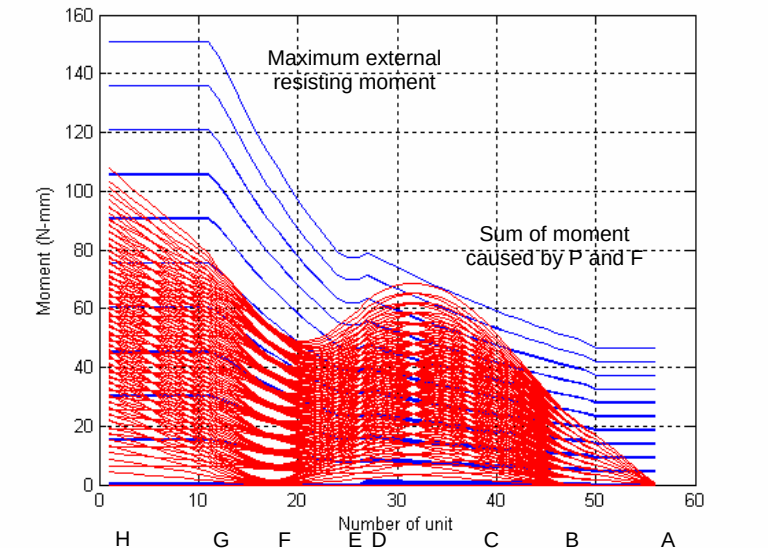

Figure 37. The maximum external resisting moment and sum of moment caused by external force P and F when delta = 5.

When delta is zero, most of the friction coefficients are located in the region of $F_1 < F_2$ without a significant discontinuity. As delta increases, the friction coefficients are crossing region of $F_1 = F_2$, and are located at the region of $F_1 > F_2$. That means we can have more choice of the combination of cable forces, and the control of cable force can be convenient. Unlike the case with no external force, there are values for the friction coefficient when F_1 equals F_2.

In the case with external forces, P and F cause a moment to be applied to each unit, and friction coefficients can be calculated. When F_2 is greater than F_1, the friction coefficient exists for the values of $F_1 = 10$ N and $F_2 = 6$ N. From Figure 36 and 37, it can be seen that when delta is five, the maximum value of external resisting moments will occur. Since the maximum value of the external resisting moment is directly related to the locking ability, we can say that the optimum value of delta is five. When delta is five, the exoskeleton structure can be stable from the external forces with the maximum combinations of the cable forces.

5.3 Optimization of cable holes

From a previous chapter, we defined delta as the geometric variable to determine the location of cable holes, and solved the optimal value of delta. The location and orientation of cable holes on the unit affects the friction and abrasion between cables and the unit. In this chapter, we introduce another variable beta for the orientation of four cable holes to minimize the loss of cable forces and cable wear. Beta is the angle between the centerline of the unit and the cable hole. We find the optimal beta so that we can minimize the cable forces that is a function of cable angles and cable wear under the assumed locations of cables.

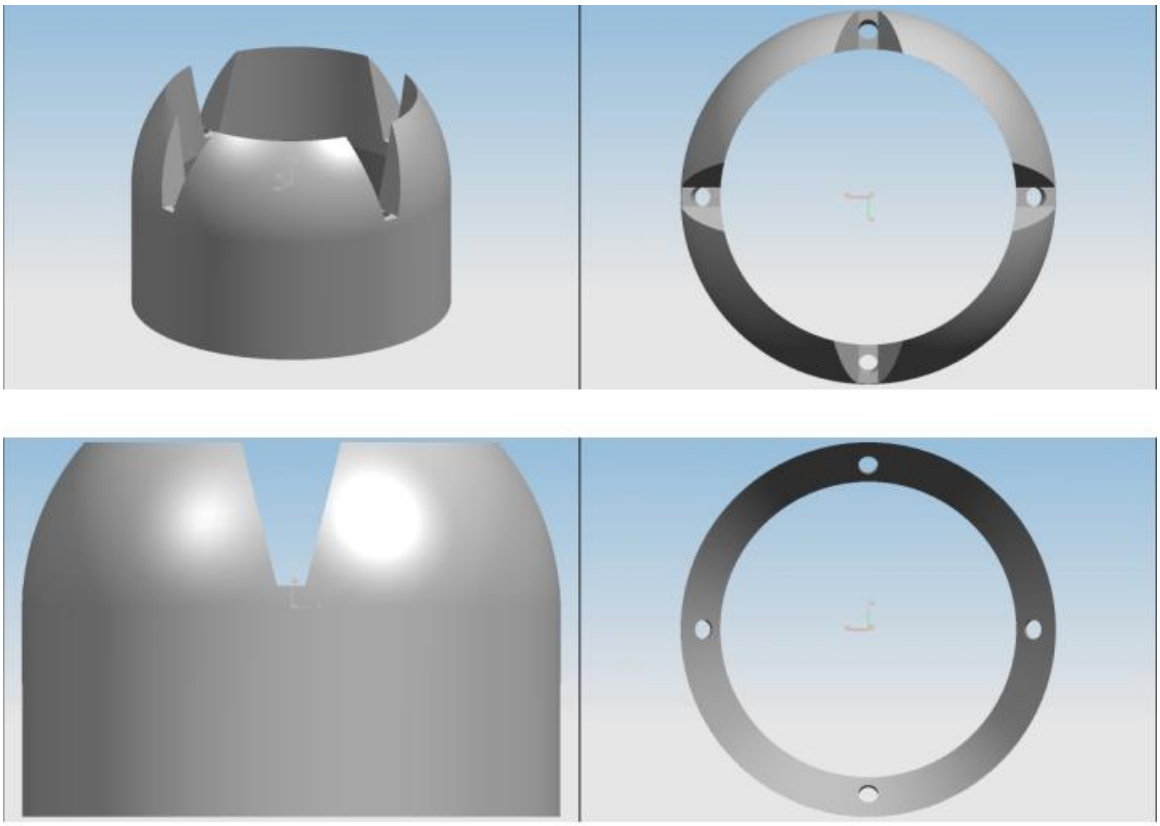

Figure 38. The prototype of an exoskeleton structure with corrected angle of four holes.

The prototype of the unit is shown in Figure 38. Chapter 4.2 showed the dimension of the unit on Figure 38. The diameter of cable hole is 2 mm and delta is 4mm. Four holes and slots are symmetrical with respect to the center point of the unit. Four reversed trapezoidal slots can make cables avoid any contact between cables and the body of the exoskeleton structure for the various angles between two units except for the inside surfaces of cable holes.

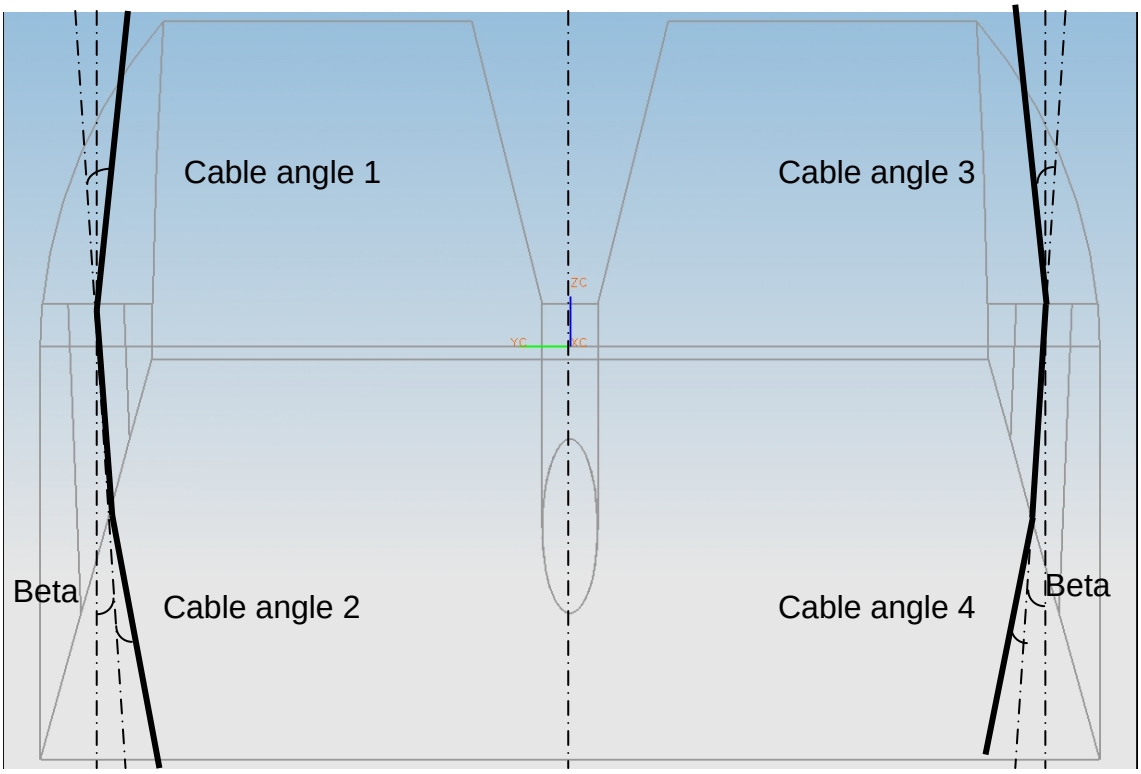

Figure 39. The unit with inclined cable holes.

Figure 39 shows the side view of the unit and we can see cable angles and beta. The bold lines depict the assumed centerlines of two cables but the diameter of the two cables in Figure 39 is not to scale. The cable angle is the relative angle between two parts of a cable. The base point of the rotation is the beginning point of the cable hole near the unit head, and as beta increases, the holes on the conical part are close to the centerline of the unit. The physical limit of beta is 30 degrees. If beta has a value of more than 30 degrees, the top of cable hole will be rotated out of the surface of the unit.

We rotate two units and measure the cable angles with various values of beta. In this simulation, the range of beta is zero to five degrees and we manually checked

that an optimal value of beta exists in this range. The rotation angles between two units are selected to be zero, three, seven, ten, and fourteen degrees for analysis. Fourteen degrees is the maximum rotation angle that two units can make.

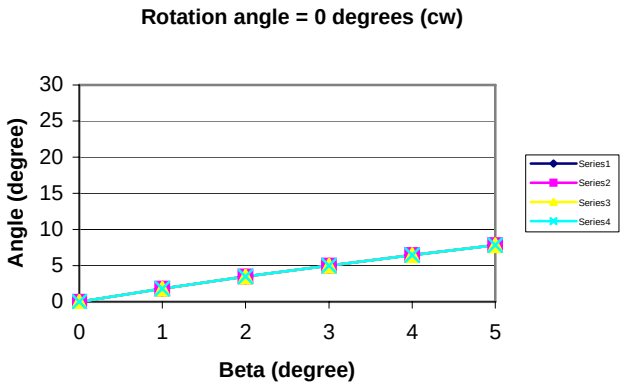

Figure 40. Four cable angles when the rotation angle of two units is zero degrees.

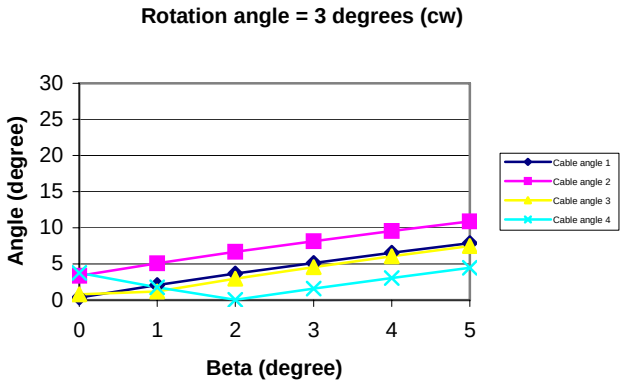

Figure 41. Four cable angles when the rotation angle of two units is three degrees.

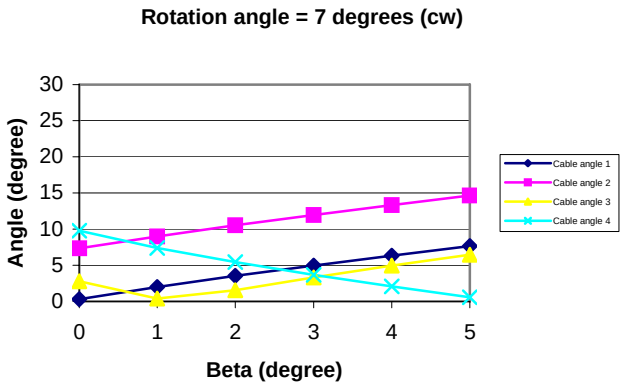

Figure 42. Four cable angles when the rotation angle of two units is seven degrees.

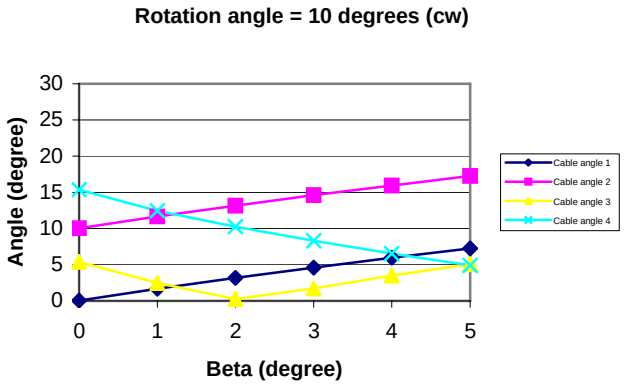

Figure 43. Four cable angles when the rotation angle of two units is ten degrees.

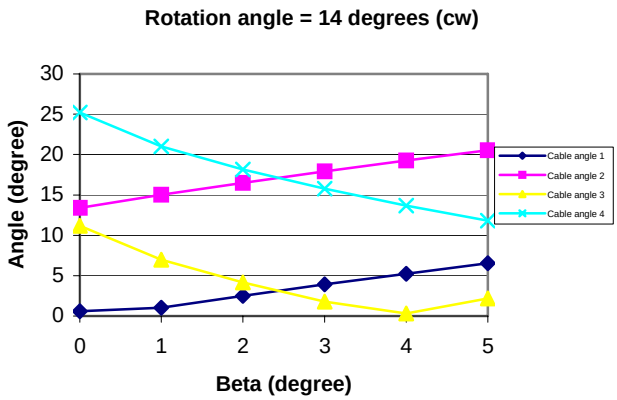

Figure 44. Four cable angles when the rotation angle of two units is fourteen degrees.

Figure 40 through Figure 44 show four cable angles with the rotation angle of zero, three, seven, ten, and fourteen degrees. Figure 39 shows that the four cable angles have the same value because there is no rotation between two units. When two units have a clock wise rotation, cable angles 1 and 2 are increased proportionally along beta and cable angle 2 is greater than 1. Cable angle 3 is varying for beta and rotation angles of two units. When the rotation angle is three degrees, cable angle 3 constantly increases with beta. In the case of seven degrees of rotation, cable angle three decreases in the range of beta zero and one and increases between beta one and five. In the case of rotation angles of ten and fourteen degrees, the minimum value of cable three is shifted to beta two and four. Table 14 represents rotation angle versus cable angles for beta zero to five.

Table 14. Rotation angle versus cable angles for beta zero to five degrees

Rotation angle=0 (degrees)	Beta	Angle 1	Angle 2	Angle 3	Angle 4	Angle sum
	0	0	0	0	0	0
	1	1.83	1.83	1.83	1.83	7.32
	2	3.48	3.48	3.48	3.48	13.92
	3	5.01	5.01	5.01	5.01	20.04
	4	6.44	6.44	6.44	6.44	25.76
	5	7.81	7.81	7.81	7.81	31.24

Rotation angle=3 (degrees)	Beta	Angle 1	Angle 2	Angle 3	Angle 4	Angle sum
	0	0.34	3.34	0.78	3.78	8.24
	1	2.07	5.07	1.21	1.78	10.13
	2	3.66	6.66	2.96	0.03	13.31
	3	5.14	8.14	4.57	1.57	19.42
	4	6.54	9.54	6.06	3.06	25.2
	5	7.87	10.87	7.47	4.47	30.68

Rotation angle=7 (degrees)	Beta	Angle 1	Angle 2	Angle 3	Angle 4	Angle sum
	0	0.33	7.33	2.79	9.79	20.24
	1	1.98	8.98	0.40	7.40	18.76
	2	3.51	10.51	1.56	5.44	21.02
	3	4.95	11.95	3.32	3.67	23.89
	4	6.32	13.32	4.93	2.06	26.63
	5	7.63	14.63	6.44	0.55	29.25

Rotation angle=10 (degrees)	Beta	Angle 1	Angle 2	Angle 3	Angle 4	Angle sum
	0	0.04	10.04	5.38	15.38	30.84
	1	1.67	11.67	2.47	12.47	28.28
	2	3.18	13.18	0.24	10.24	26.84
	3	4.60	14.60	1.71	8.28	29.19
	4	5.95	15.95	3.47	6.52	31.89
	5	7.25	17.25	5.09	4.90	34.49

Rotation angle=14 (degrees)	Beta	Angle 1	Angle 2	Angle 3	Angle 4	Angle sum
	0	0.59	13.40	11.18	25.18	50.35
	1	1.01	15.06	6.98	20.98	44.03
	2	2.50	16.50	4.16	18.16	41.32
	3	3.91	17.91	1.77	15.77	39.36

4	5.25	19.25	0.31	13.68	38.49
5	6.54	20.54	2.19	11.80	41.07

Table 15. Sum of cable angles with rotation angles and beta. (degrees)

Rotation angle	Beta (degrees)					
	0	1	2	3	4	5
0	0	7.32	13.93	20.06	25.79	31.25
3	8.26	10.15	13.33	19.44	25.21	30.70
7	20.25	18.78	21.03	23.91	26.64	29.26
10	30.86	28.29	26.85	29.20	31.90	34.50
14	50.37	44.00	41.33	39.36	38.50	41.08
Total sum	109.75	108.57	116.50	131.99	148.05	166.82

Table 15 shows the sum of the cable angles with rotation angles and beta. By checking the sum of the cable angles, we can predict the total amount of loss of cable forces. A minimum value of cable angles can minimize the loss of cable forces, and we showed it on Chapter 3.4 and 4.5. We can add all the cable angles for each beta and come up with the total summation of cable angles. When beta is one degree, the total summation of the cable angles has the minimum value, and we can choose beta of one degree for the minimum summation of cable angles.

To increase the lifetime of the cables, we have to minimize the maximum value of angles on Table 14 for each case of beta and rotation angles. We can choose the maximum value of angles for each case of beta and when the rotation angle has a value of fourteen degrees, the cable angle 4 has three values (beta 0, 1, and 2 degrees) and the cable angle 3 has three values (beta 3, 4, and 5 degrees). If we plot six values and add more values when we approach the minimum value, we have Figure 45. The minimum value of the maximum cable angles occurs at a beta

of 2.4 degrees and we can choose a beta of 2.4 as the optimal value for the minimum cable wear.

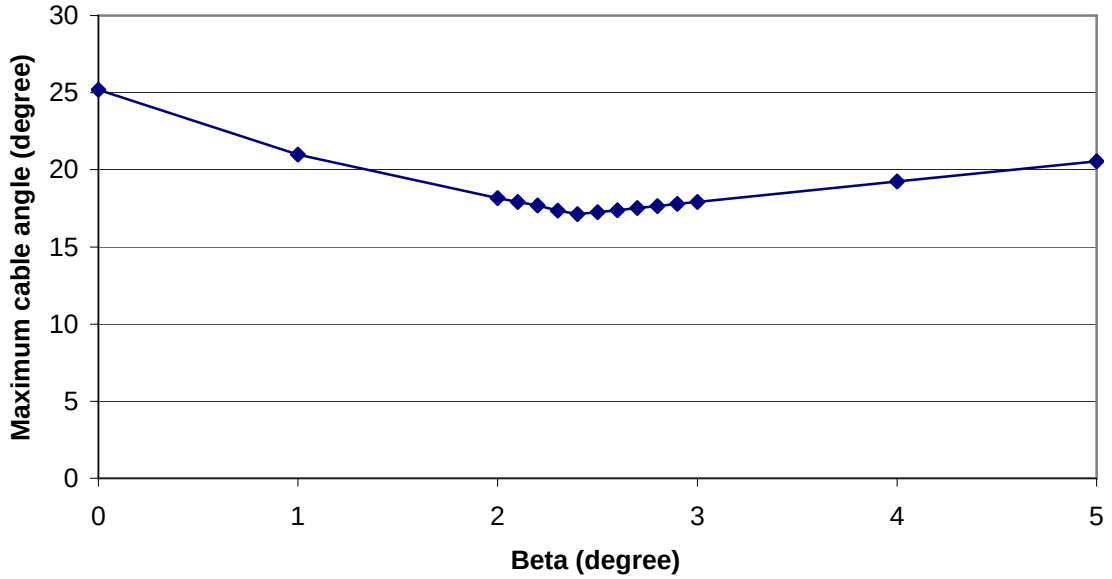

Figure 45. Maximum cable angles versus beta.

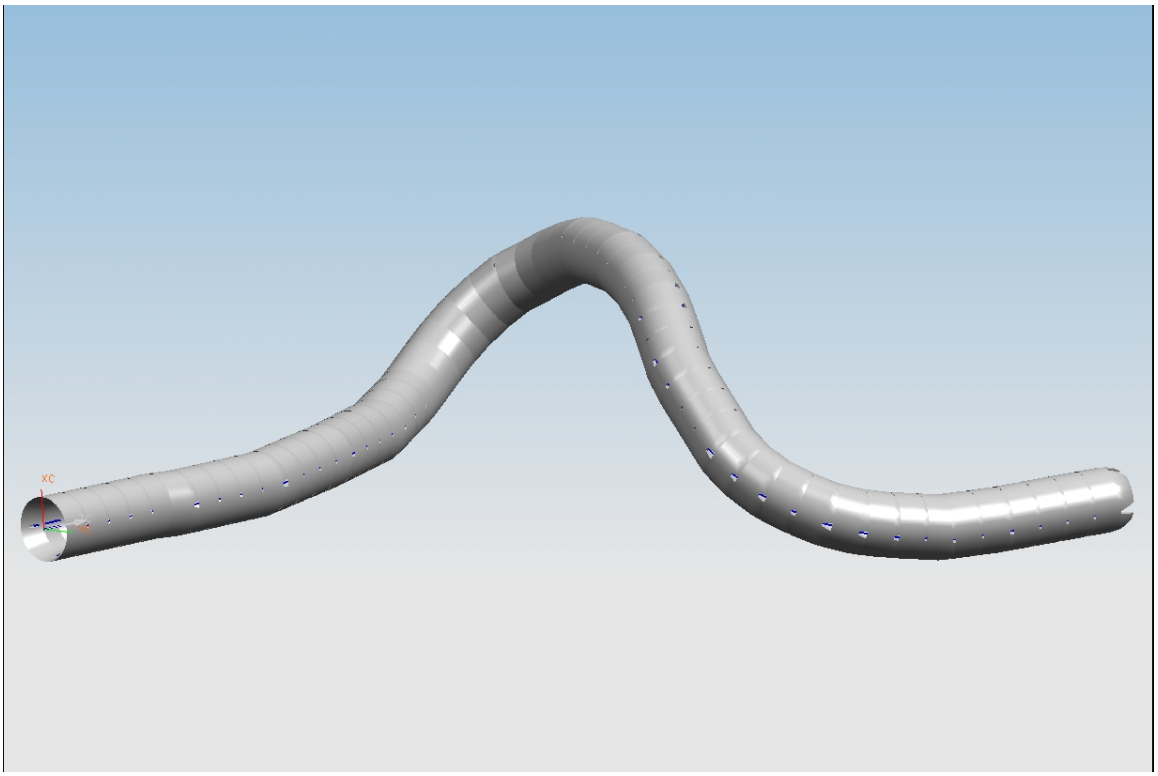

Figure 46. The exoskeleton structure with four cables from the anus to the sigmoid colon

Based on the geometry of the unit with optimized beta, we check the cable angles with the configuration of a human colon. Figure 46 shows the exoskeleton structure comprised of the units and four cables and the exoskeleton structure copies three dimensional curve of the human colon from the anus to the sigmoid colon. The left end of the exoskeleton structure depicts the exoskeleton structure where it enters the anus. The relatively straight portion represents the exoskeleton structure in the rectum. The radius of the curvature of the first sharp curve is about 25 mm and the total length of the exoskeleton structure is 500 mm, or about 58 units long. Four tendons are passed through the units and fixed at the end of the

unit. The first unit can be fixed to avoid the relative motion to other units, and we can pull and release the tendons to control stiffness of the exoskeleton structure. When the tension is applied to the four tendons, locking ability is activated between the units, and the exoskeleton structure is stiffened to hold the position of the exoskeleton structure. No gap exists between the contact areas of the units except for the reverse trapezoidal slots and the conically bored end part of the units to fulfill the contact condition. An endoscope will go through the exoskeleton structure and the inside of a colon wall is protected for the force caused by the end of the distal tip and the stem of the endoscope.

The configuration of the exoskeleton structure will decide the path of four cables. To scrutinize the path of four cables through the units, Figure 47 shows the skeleton view of Figure 46 and four bold lines depict four cables. There is no positional twist along the axial direction between the units.

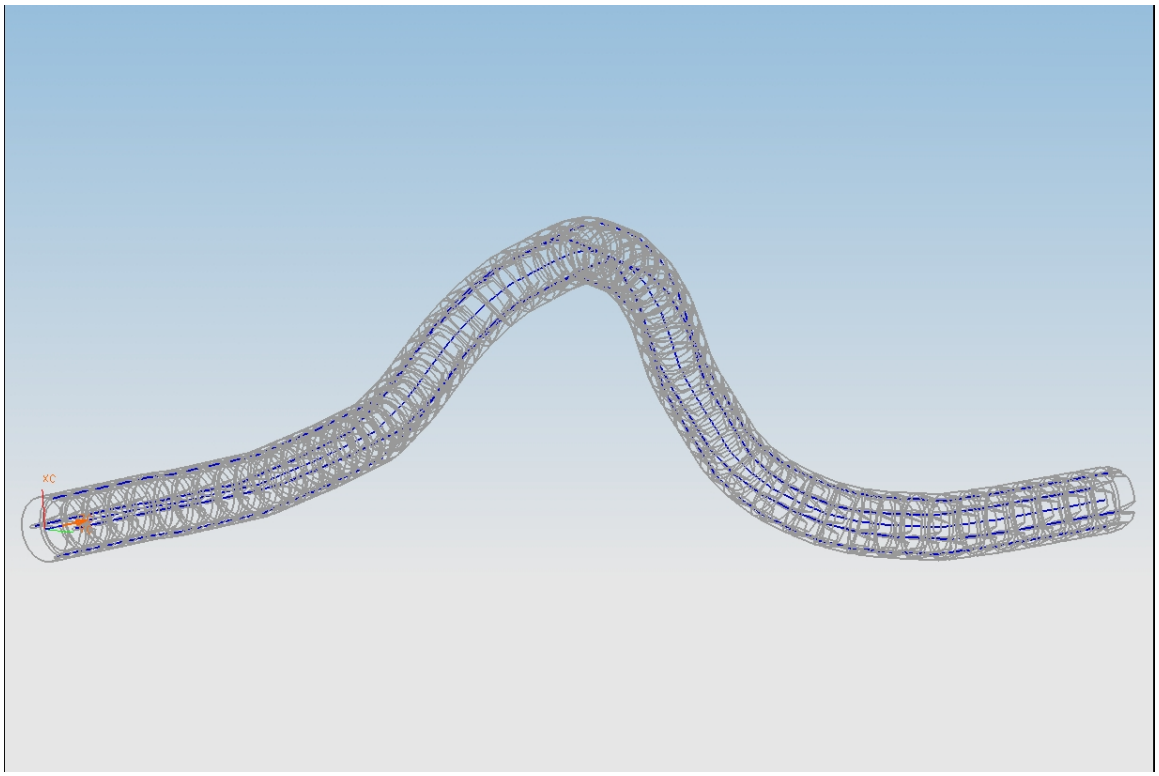

Figure 47. Outline view of Figure 45.
(Four thick lines through the exoskeleton structure refer to the four cables)

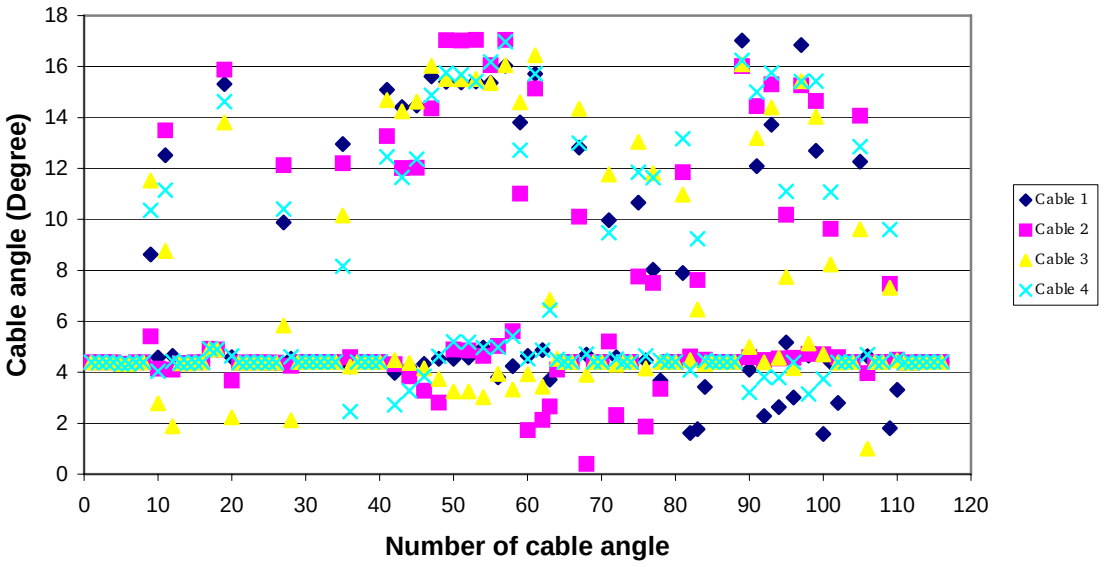

Figure 48. The cable angles of four cables through units.

Figure 48 shows cable angles of four cables through the exoskeleton structure and the absolute values are plotted regardless of their direction (CW or CCW). From the geometry of the unit, one cable has two cable angles per the unit on Figure 39, and the total number of the units for the exoskeleton structure is 58. Figure 11 shows the cable and two cable angles. Because of beta which makes four cable holes tilted, cable angle has values for the straight position of the exoskeleton structure. At the anus, the exoskeleton structure started the straight position, and from the first to the eighth unit is straight position. Because of the beta, cable angles have non-zero values at the straight configuration of the exoskeleton structure. The first curve starts from unit number 20 to 40 and the second curve is from unit number 45 to 51. The maximum value of the cable angles is less than 18 degrees and the results are from the optimized value of beta=2.4.

5.4 Conclusion for Chapter 5

We found that loss of the cable force is linear result with respect to increasing cable angles, but the locking characteristics for the units have different aspects for the different configuration of the exoskeleton structure. In the case of no external force analysis, we found the limit of delta, and the range of possible combinations of cable forces.

The results of simulation with external forces are directly applicable for a flexible self-retaining retractor with a base. We found the characteristics of delta with respect to two external forces, the friction coefficients, and cable forces. A simulation program was developed to find the maximum external forces for a given sets of cable forces and an optimal value of delta. Using the previously defined geometric variables, force variables were found to satisfy the required friction coefficient. The possible range of cable forces was verified for the given external forces and optimal cable holder locations.

We found the optimal value of the orientation of cable holes to minimize the loss of cable forces and cable wear by minimizing the cable angles. The result was shown with the geometry of a human colon.

6. Closed Form Solution of the Friction Coefficient with Four Cables

From the analysis in a two-dimensional plane, we derived a closed form solution of the limiting friction coefficient for stability in terms of cable forces. We assumed that the critical friction coefficient is 0.2, and if the combination of cable forces is more than the critical friction coefficient, a slip between two cylindrical units may occur and a unit will lose its locking ability. In a real system, we use four cables to control the stiffness of the exoskeleton structure. Since the location of two sets of cables are orthogonal to and decoupled from each other, and using an assumption of no axial rotation of each unit, superposition can be used to complete the analysis of a four-cable system for the three dimensional space curves of a human colon. Based on the analysis of the friction coefficient with two cables, we now develop the closed form solution for the friction coefficient using four cables to analyze the relation of cable forces and friction coefficient between units. The solution will not work for the zero degrees of the units with four same cable forces.

6.1 Configuration of Two Units

Here we present the first stages of three-dimensional modeling of the unit. First we diagram two consecutive units with associated coordinate frames, in Figure 49. Whereas the previous, 2-dimensional model only considered 2 cables per unit, this 3-D model incorporates all four cables, with forces F_1, F_2, F_3, and F_4. For simplicity, we do not yet consider the spherical, tapered ends which go 5 mm beyond the distal cable attachments (i.e. the trapezoidal-slotted portions shown in Figure 38). In other words, we do not yet consider the interface between the units.

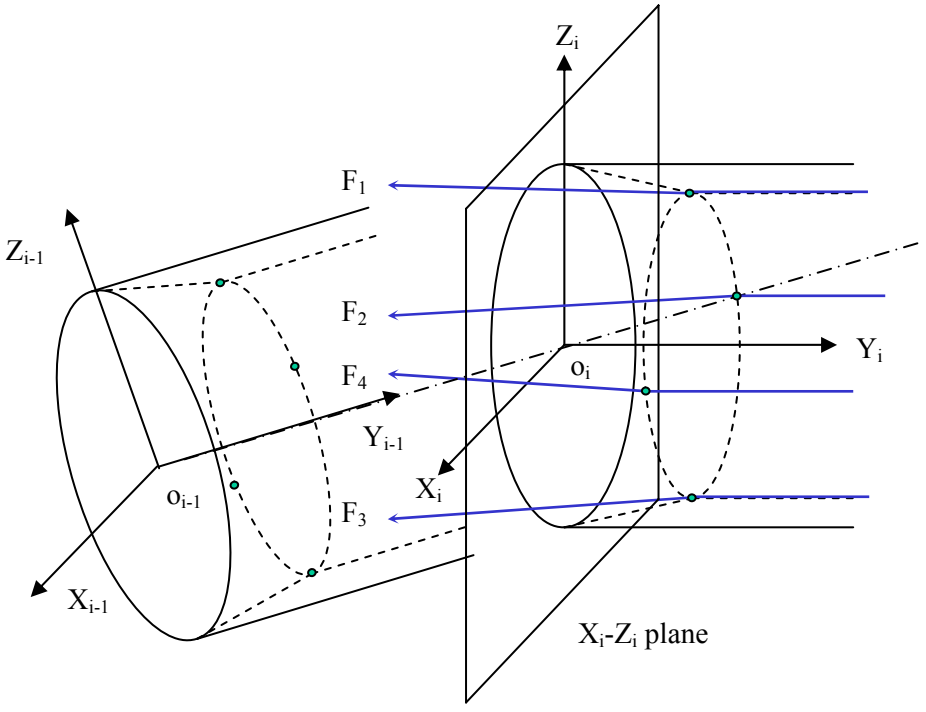

Figure 49. Two consecutive units with coordinate frames and four cable forces

Where,

X_{i-1} :Origin of i-1 coordinate frame

X_i :Origin of i coordinate frame

$X_{i-1}Y_{i-1}Z_{i-1}$: component of i-1 coordinate frame

X_i Y_i Z_i: component of i coordinate frame

i coordinate frame : rotation and translation of i-1 coordinate frame

For further simplicity, the cables are not shown on the *i*-1-th unit. The end of the *i*-th unit is exactly on the X_i-Z_i plane. The four cables are radially constrained, but are free to move along the Y-axis. The detailed way to attach the cables to the inside wall of the unit is not shown in the figure. Origin points are always on the Y-axis and no rotation occurs along the Y-axis. The distance between origin points of the coordinate frame is the same under normal locking situations, regardless of the rotation of the unit or the coordinate frame.

Table 16. Comparison between 2-D vs. 3-D model

	2-D model	3-D model
Number of cable	2	4
Cable force	Half analysis	Full analysis
Configuration	Two dimensions (Y-Z plane)	Three dimensions (X-Y-Z)
Friction coefficient for each unit	Based on 2-D static model	2-D static modeling with equivalent forces

Table 16 summarizes the comparison between two-dimensional and three-dimensional models. The two-dimensional model uses two cables on a two-dimensional plane (Y-Z plane). The three-dimensional model uses four cables for the full analysis of the interface part of two units. For the given cable forces, we determine a locking ability at the interface of a specific unit. Within the allowable friction coefficient, we also solve the range of the four cable forces, which corresponds to holding the locking ability. Using the four cable forces, we find a principal rotation plane and rotation axis, which is on the X-Z plane.

We can model a three-dimensional configuration from the average shape of a human colon. Since an endoscope minimizes invasiveness and does not change the shape of a human colon, we assume that the location of the stem and the exoskeleton structure of an endoscope are inside the middle of a human colon. To copy the shape of a human colon, we need information of each unit's heading angle. The length of a unit is already decided and does not change for the heading angles. Once the endoscope copies the shape of a human colon for its entire length, we calculate the cable angles for each unit. Four cables go through the units and each cable has two cable angles with respect to the rotation axis. We analyze the losses of cable forces for each cable with calculated sets of cable angles.

For the fixed cable forces, we find the axis of rotation, which is on the X-Z plane. Because of the radial constraint condition and structural characteristics, we assume that no rotation will occur along the Y-axis.

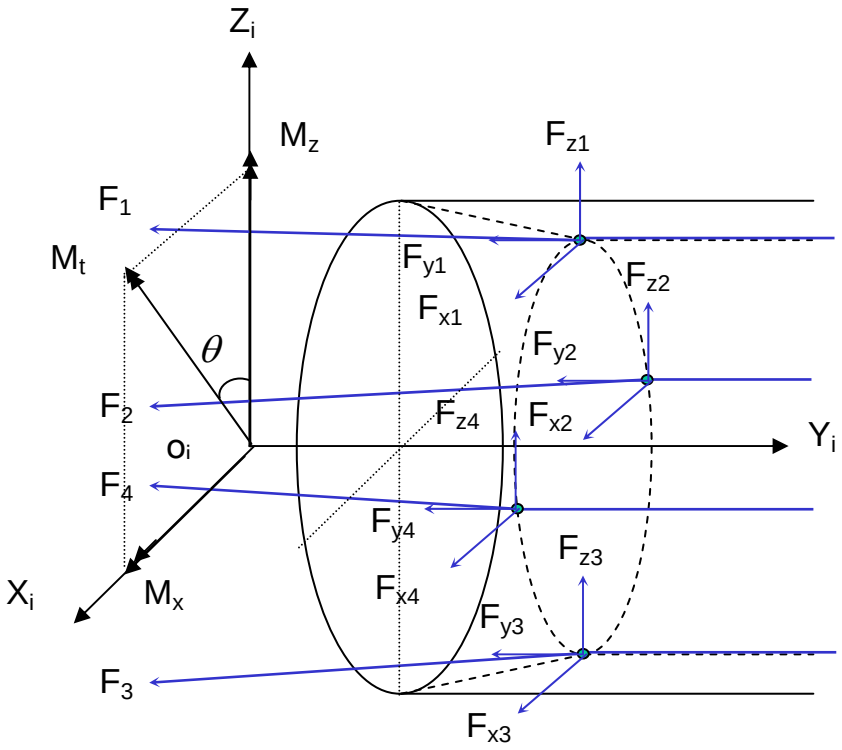

Figure 50. Unit on the coordinate frame with the components of cable forces and moments.

Where,

M_x and M_z: moment on x and z axis

M_T: Vector sum of M_x and M_z

F_1, F_2, F_3, and F_4: four cable forces

In Figure 50, we set the origin of the coordinate frame at the fixed rotation point. In other words, the rotation axis always passes through the origin point. The sum

of cable forces F_{Y1}, F_{Z1}, F_{Z2}, F_{Y3}, F_{Z3}, and F_{Z4} cause moment M_X. The sum of cable forces F_{X1}, F_{X2}, F_{Y2}, F_{X3}, F_{X4}, and F_{Y4} cause moment M_Z. M_T is the sum of moments for M_X and M_Z.

To solve the friction coefficient for the case of four cables, we convert the four cable forces to two equivalent cable forces without changing the total moment and forces.

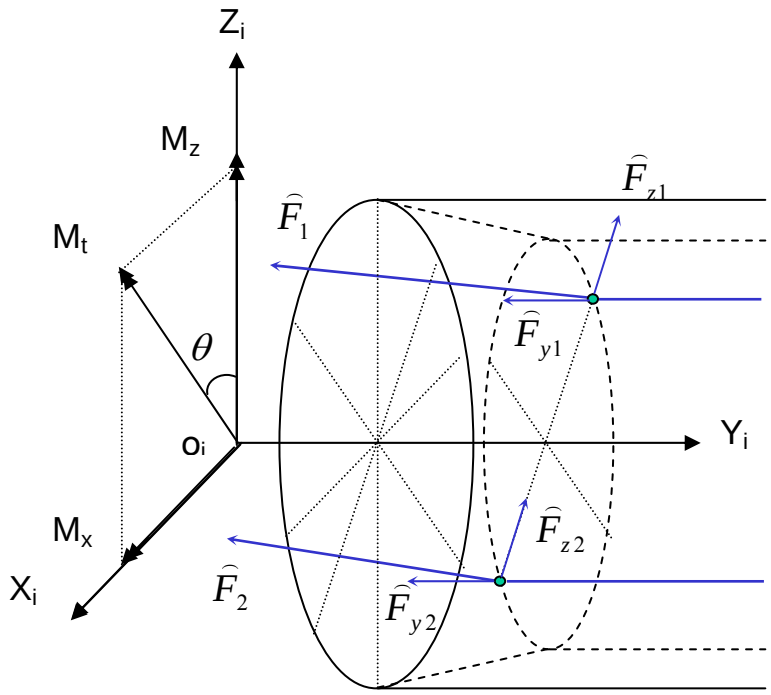

Figure 51. Two equivalent forces and force components

Where,

$\widehat{F}_1$ and $\widehat{F}_2$: two equivalent cable forces

We substitute cable forces F_1, F_2, F_3, and F_4 to $\hat{F}_1$ and $\hat{F}_2$. Figure 51 shows the equivalent force components of $\hat{F}_1$ and $\hat{F}_2$. The component forces F_{xi}, F_{yi}, and F_{zi} (i=1,2,3, and 4) are replaced by $\hat{F}_{Yj}$ and $\hat{F}_{Zj}$. (j=1 and 2) From Figure 51, we recognize that the axis of M_T and the axis which passes two constraint points of $\hat{F}_1$ and $\hat{F}_2$ are perpendicular to each other.

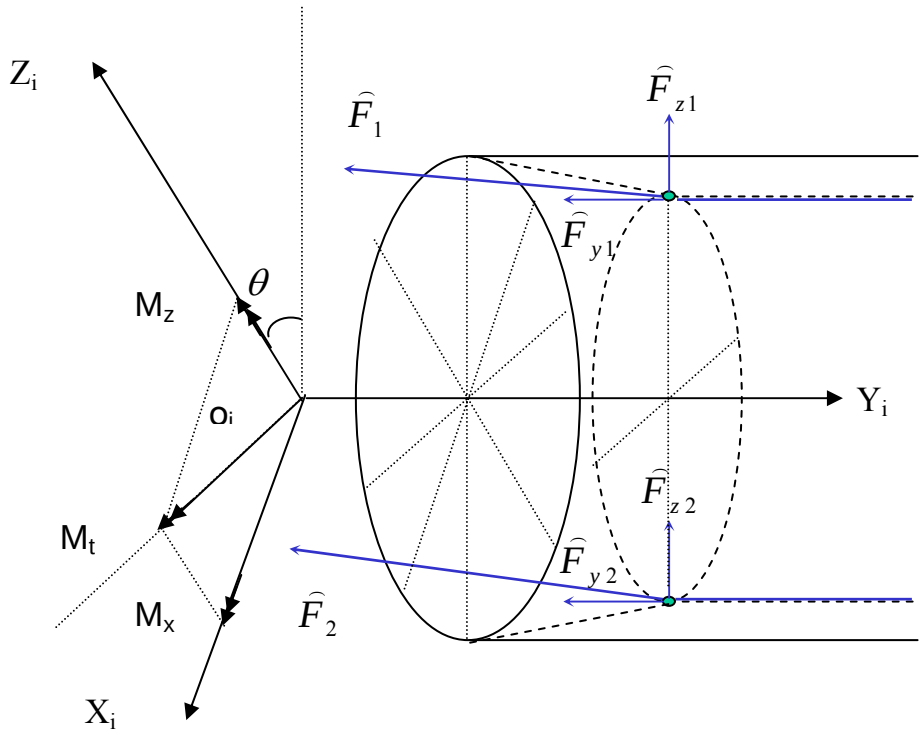

Figure 52. Rotated two equivalent forces and force components

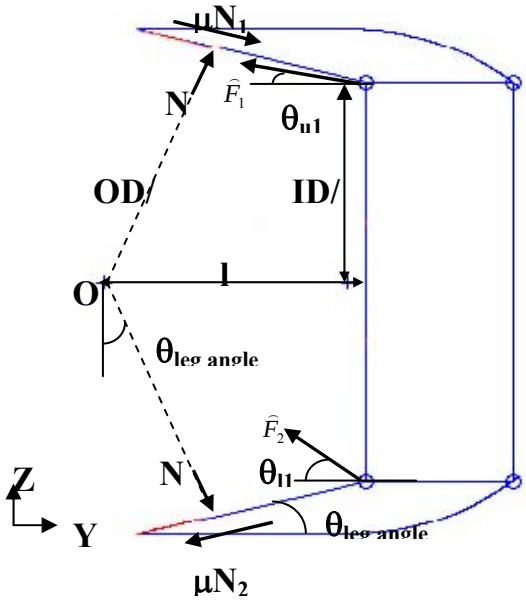

Figure 53. Figure 51 viewed from M_T axis with reaction forces

Since there is no force component in the X-direction, we treat Figure 52 as a two-dimensional problem. Figure 53 is a result of a view from the axis corresponding to M_T. Now we use two-dimensional equations with equivalent forces and rotation angle to solve the friction coefficient for each unit.

6.2 Assumptions of Equivalent Forces

A number of assumptions related to the unit and cable mechanism are required to reduce cable forces to a set of equivalent forces. We assume that cables and

cylindrical units are rigid and no elongation occurs during the operation. Specifically, the three major assumptions are:

1. The rotation axis due to the moment passes through the origin point of the coordinate system ‘o’.

   The head of a unit is spherical and fits inside a tail part of a unit. When a unit rotates along the X-axis, point o will not change position.

2. The rotation axis due to the moment is on the X-Z plane.

   As long as each unit satisfies the contact condition, the principal rotation axis remains on the X-Z plane and passes through the point ‘o’.

3. No rotation on the Y-axis.

   Since the distance between cable holders at the head and tail of a unit is short and due to the stiffness of the cables, no rotation will occur when units are locked. When units are unlocked, they have enough stiffness not to rotate along the Y-axis but still can copy the shape of a colon without inducing stresses inside the colon wall.

6.3 Mathematical Model

By equating the force values from Figure 50 and 51, we calculate the summation of all cable force vectors.

$$\left|F_1 + F_2 + F_3 + F_4\right| = \left|\widehat{F}_1 + \widehat{F}_2\right| \tag{19}$$

If we square both sides of equation (19) and express them as X, Y, and Z components:

$$\left(\sum_{i=1}^{4} F_{xi}\right)^2 + \left(\sum_{i=1}^{4} F_{yi}\right)^2 + \left(\sum_{i=1}^{4} F_{zi}\right)^2 = (\hat{F}_{z1} + \hat{F}_{z2})^2 + (\hat{F}_{y1} + \hat{F}_{y2})^2 \tag{20}$$

where

$F_1 = F_{x1}\, i + F_{y1}\, j + F_{z1}\, k$

$F_2 = F_{x2}\, i + F_{y2}\, j + F_{z2}\, k$

$F_3 = F_{x3}\, i + F_{y3}\, j + F_{z3}\, k$

$F_4 = F_{x4}\, i + F_{y4}\, j + F_{z4}\, k$

$\hat{F}_1 = \hat{F}_{z1} \cos\theta\, i + \hat{F}_{y1}\, j + \hat{F}_{z1} \sin\theta\, k$

$\hat{F}_2 = \hat{F}_{z2} \cos\theta\, i + \hat{F}_{y2}\, j + \hat{F}_{z2} \sin\theta\, k$

The sum of cable forces in the X, Y, and Z directions will results in equations (21), (22), and (23), where *i*, *j*, and *k* represent unit vectors in the X, Y, and Z directions, respectively.

$$\sum F_x : (F_{x1} + F_{x2} + F_{x3} + F_{x4})\, i = (\hat{F}_{z1} + \hat{F}_{z2}) \cos\theta\, i \tag{21}$$

$$\sum F_y : (F_{y1} + F_{y2} + F_{y3} + F_{y4})\, j = (\hat{F}_{y1} + \hat{F}_{y2})\, j \tag{22}$$

$$\sum F_z : (F_{z1} + F_{z2} + F_{z3} + F_{z4})\, k = (\hat{F}_{z1} + \hat{F}_{z2}) \sin\theta\, k \tag{23}$$

From equations (21), (22), and (23), we derive equation (24), which is the same as equation (19), without Y-component forces. From equation (24), we assume that

the sign of the sum of force vectors is positive, since the cable tension is always positive.

$$\widehat{F}_{z1} + \widehat{F}_{z2} = \sqrt{\left(F_{x1} + F_{x2} + F_{x3} + F_{x4}\right)^2 + \left(F_{z1} + F_{z2} + F_{z3} + F_{z4}\right)^2} \tag{24}$$

The sums of moments along the X and Z-axes are presented in equation. (25) and (26),

$$M_x = (F_{y1} - F_{y3})\, r_i + (F_{z1} + F_{z2} + F_{z3} + F_{z4})\, lt \tag{25}$$

$$M_z = (F_{y2} - F_{y4})\, r_i + (F_{x1} + F_{x2} + F_{x3} + F_{x4})\, lt \tag{26}$$

where r is half the inner diameter (ID) and lt is the distance from the origin of a coordinate frame to the point of cable constraint along the Y-axis.

The total moment is the sum of moments along the X and Z-axes and is equal to the moment caused by equivalent force components.

$$M_T = \sqrt{M_x^2 + M_z^2} = (\widehat{F}_{y1} - \widehat{F}_{y2})\, r_i + (\widehat{F}_{z1} + \widehat{F}_{z2})\, lt \tag{27}$$

From equations (21), (22), (23), and (27), we solve for the components of equivalent forces, shown in equations (28), (29), and (30).

$$\widehat{F}_{y1} = \frac{1}{2}\left(\sum_{i=1}^{4} F_{yi} + \frac{M_T}{r_i} - \frac{lt}{r_i}\sqrt{\left(\sum_{i=1}^{4} F_{xi}\right)^2 + \left(\sum_{i=1}^{4} F_{zi}\right)^2} \right) \tag{28}$$

$$\widehat{F}_{y2} = \frac{1}{2}\left(\sum_{i=1}^{4} F_{yi} - \frac{M_T}{r_i} + \frac{lt}{r_i}\sqrt{\left(\sum_{i=1}^{4} F_{xi}\right)^2 + \left(\sum_{i=1}^{4} F_{zi}\right)^2} \right) \tag{29}$$

$$\widehat{F}_{z1} + \widehat{F}_{z2} = \sqrt{\left(\sum_{i=1}^{4} F_{xi}\right)^2 + \left(\sum_{i=1}^{4} F_{zi}\right)^2} \tag{30}$$

Although we have four equations, equations (21) and (23) are coupled and result in only one independent equation. Equation (30) contains two unknowns, which are the Z-components of equivalent forces.

Now we have the equivalent forces in terms of geometric variables, total moment, and cable forces (equations (20), (21), and (22)) and are ready to apply equivalent forces to the solution of the friction coefficient from the two-dimensional model.

From Figure 52, we can express two equivalent forces in terms of cable forces F1, F2, and cable angles (θ_{u1} and θ_{l1}).

$$\widehat{F}_{y1} = F_1 \cos\theta_{u1} \tag{31}$$

$$\widehat{F}_{y2} = F_2 \cos\theta_{l1} \tag{32}$$

$$\widehat{F}_{z1} = F_1 \sin\theta_{u1} \tag{33}$$

$$\widehat{F}_{z2} = F_2 \sin\theta_{l1} \tag{34}$$

We substitute the components of equivalent forces (equations (31), (32), (33), and (34)) to the 2-D equations (equations (9), (10), and (11)).

$$\Sigma F_x : (N_1 + N_2)\sin\theta + \mu(N_1 - N_2)\cos\theta - \widehat{F}_{y1} - \widehat{F}_{y2} = 0 \tag{35}$$

$$\Sigma F_y : (N_1 - N_2)\cos\theta - \mu(N_1 + N_2)\sin\theta + \widehat{F}_{z1} + \widehat{F}_{z2} = 0 \tag{36}$$

$$\Sigma T : -\mu(N_1 + N_2)\frac{OD}{2} + (\widehat{F}_{y1} - \widehat{F}_{y2})\, r_i + lt(\widehat{F}_{z1} + \widehat{F}_{z2}) = 0 \tag{37}$$

We have three unknowns (N1, N2, and μ) and three equations (equations (35), (36), and (37)). We solve for the friction coefficient (μ) as a function of equivalent forces, geometric variables, and rotation angle (μ) to obtain equation (38).

$$\mu = \frac{OD\Delta y + \sqrt{OD^2 F_y{}^2 - 4\left[ID\Delta y + 2lt\sin\theta F_Z\left[-ODF_Z + ID\sin\theta\Delta y + 2ltF_Z\right]\right]}}{2\left\{ODF_Z - \sin\theta\left[ID\Delta y + 2ltF_Z\right]\right\}} \tag{38}$$

Where,

$F_y = F_{y1} + F_{y2}$

$\Delta y = F_{y1} - F_{y2}$

$F_z = F_{z1} + F_{z2}$

There are two conditions for the solution for the friction coefficient. First, the argument in the square root must be greater or equal to zero. Secondly, the numerator must not vanish:

$$OD^{2}F_{y}^{2} - 4\left[ID\,\Delta y + 2lt\,\sin\theta F_{Z}\left[-ODF_{z} + ID\,\sin\theta\Delta y + 2ltF_{z}\right]\right] \geq 0 \tag{39}$$

$$ODF_{z} - \sin\theta\left[ID\,\Delta y + 2ltF_{z}\right] \neq 0 \tag{40}$$

From equations (39) and (40), we find the constraint condition of the forces and a design principle for the rigid unit with respect to the cable forces.

6.4 Conclusion for Chapter 6

We derive the closed form solution of a friction coefficient using a two-dimensional model with two equivalent cable forces. For a given curvature of a human colon, we can calculate the allowable operating range of cable forces while maintaining a locking ability among units. From the friction coefficient, we can check critical parts for a possible kink or collapse with the inputs of four cable forces. A four-cable model is more applicable for the simulation of an exoskeleton structure of an endoscope and a retractor application.

7. Elastic Analysis: Endoscope in an Exoskeleton Structure

Stiffness in the stem of endoscope introduces distributed forces on the inner surface of the exoskeleton structure. Most external forces inside the wall of the exoskeleton structure are restitution forces from the bent stem. In other words, the shape of the exoskeleton structure constrains the stem, resulting in external forces on the inner surface of the exoskeleton structure. We reverse the problem and solve the distributed forces for the given shape of the stem.

In this chapter, we solve for the external forces on the surface of a specific configuration of a stem. From the external reaction forces, we can find the optimum stiffness of the stem to obtain the best operation of an endoscope. Generally, the stem of an endoscope is comprised of rubber tubes optical lines, which can be represented by an elastic equivalent with assumptions.

7.1 Review of Elastica problems

Frisch-Fay broadly explained many cases of flexible bars [25]. In particular, we can use his model of a cantilever under *n*-concentrated loads as a model for the endoscope stem. To solve the cantilever problem with *n*-concentrated loads, bending moment equations must be reduced to Legendre's standard elliptic forms. Since there are no closed form solutions for the Legendre's equation, a numerical method and table of values should be used to calculate the approximate solutions. For the *n*-concentrated loads, we need to set up 2*n*-1 numbers of equations and use

the principle of elastic similarity, which is similar with superposition theory. The difficulties of this method are finding the moduli, which determine the shape of the bar, new variables, and integration constants. This method can be extended and applied to *n*-inclined concentrated loads.

Nakagiri presented a formulation to find the shape of thin bent rods in a plane. He used Lagrange multipliers to develop the formulation, and assumed that strain energy is stationary through the bent rod. Experiments and numerical solutions matched well, and the material properties of the rod were not much affected by the shape of the rod [26]. However, the uniqueness of his solution and the stability of the rod are not applicable to our exoskeleton structure design.

Wilson and Mahajan presented an analysis and a positioning algorithm for flexible limbs. The authors employed large deflection theory to calculate the position of a tip of flexible robotic limbs by using an adaptive positioning program. The flexible robotic limbs are comprised of a series of polymeric tube elements and manipulated by the internal pressure in each element. The adaptive positioning program improved both computational speed and positioning accuracy [27].

Howell et al. developed an evaluation of equivalent spring stiffness using a large deflection compliant mechanism. They also proposed new modeling equations. From the parametric approximations of a pseudo-rigid body model, they derived stiffness coefficients and showed examples to validate the new modeling equations [28]. Their new models are useful to apply to the motion of large deflection members and for optimization of compliant mechanisms.

Chucheepsakul and Huang presented two methods to approach the elastica problems. The first method uses elliptic integral formulations and the second method uses variational formulation in a stationary condition of the potential energy function. They compared numerical results and calculated critical values of moments. The finite element method based on the Eulerian method also yielded good results [29].

Navaee and Elling presented a study on the deflected configurations of a cantilever beam subjected to a specified inclined end load. The solutions were described to find all deflected shapes on the beam with minimal computational efforts. The authors developed specific equilibrium configurations with various end loading conditions for seven cases with the Ten Point Gauss-Legendre Formula [30].

Plaut and Mroz investigated unidirectional bucking of an elastica with pinned ends. They neglected the beam weight and subjected to an axial compressive load. They determined equilibrium paths with various initial conditions and examined three geometry of elastica: unbuckled configuration with no initial curvature, unbuckled configuration with initial curvature, and buckled configuration [31].

Plaut et al. developed equations and a method of deflections and buckling of a bent elastica with a flat surface. Many planar equilibrium shapes were demonstrated with various end conditions. The authors analyzed some of the important parametric variables with symmetric and asymmetric shapes of a thin and inextensible elastic strip [32].

Plaut et al. showed the elastic behavior of the loop tack test for pressure sensitive adhesives. The developed mathematical formulations based on the equilibrium

model of elements of elastica, and calculated numerical solutions by using a shooting method. The results described the characteristics of the shapes and forces of loop tack for an inextensible and nonlinearly-elastic loop [33].

Plaut et al. investigated post buckling and vibration of elastica with end conditions. They established formulations of equilibrium with no contact case, symmetric case with self-contact, and asymmetric case with contact of strip and substrate. This research is focused on flexible electronic circuits and many flexible lines in automobiles [34].

In summary, we will use Plaut's works [31,32,33,34] to calculate the reaction forces of the bent stem of an endoscope.

7.2 Assumptions of Elastica Problems

We consider the stem of an endoscope as uniform and elastic. The stem is inextensible in bending and the bending moment through the stem is assumed to be proportional to the entire curvature. The friction coefficient between the inside wall of an exoskeleton structure and the surface of the stem is neglected, as is the weight of the stem. There will not be much space inside the exoskeleton structure and the stem will fit perfectly inside the exoskeleton structure. The shape of the stem will pass the centerline inside the exoskeleton structure and make contact at known points on the inner surface of the exoskeleton structure.

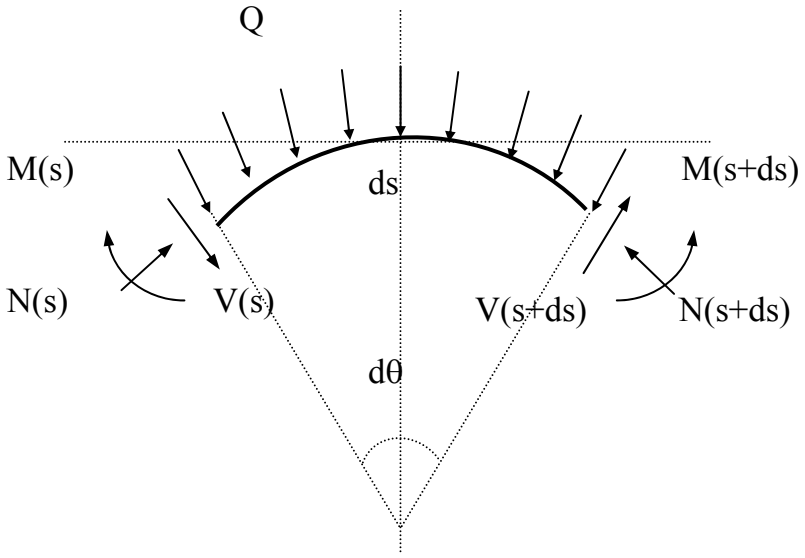

Figure 54. Free-body diagram of segment of a stem [31].

Where,

N(s): normal force at the position s

V(s): shear force at the position s

M(s): moment at the position s

Q: distributed force on ds

ds: length of the beam

dθ; angle along ds at the center of radius of curvature

Position s starts from the left side of the segment.

Equation (41) derived in Appendix B is the nonlinear equation and θ is a function of path s. Q is the distributed force per unit length along the segment in Figure 54. With boundary conditions, we can integrate equation (41) and solve for the distributed forces along the segment.

$$EI\frac{d^3\theta}{ds^3}+N_0\frac{d\theta}{ds}+\frac{EI}{2}\left(\frac{d\theta}{ds}\right)^3=Q \tag{41}$$

7.2 Distributed Force along a Quadrant

To check the equation of the distributed force, we apply it to a simple quadrant. The length of the stem is L and the bending stiffness is EI. Initially straight, the distributed force along its surface bends the stem. The initial point of s is fixed and the direction of distributed force in Figure 55 is towards the center point of the quadrant.

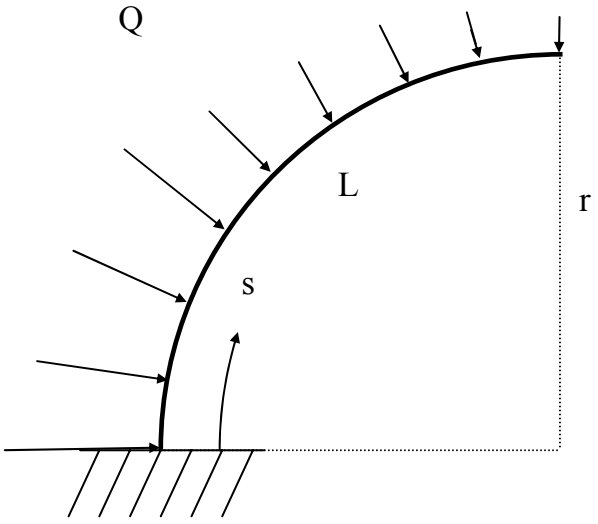

Figure 55. Distributed Force along the quadrant

Q: distributed force (not actual magnitude)

L: length of the beam

s: path of the beam

r: radius of curvature

For the given configuration in Figure 55, the boundary conditions are defined in equations (42) and (43).

At the beginning of beam (fixed end and s=0),

$$\theta(0) = 0 \tag{42}$$

At the end of beam (free end and s=L),

$$\text{M=0 and V=0 or } \theta'(0) = 0 \text{ and } \theta''(0) = 0 \tag{43}$$

For static analysis of the equilibrium case, no initial normal force (N_0) is applied.

$$N_0 = 0 \tag{44}$$

$$\text{For the quadric circle, } ds = rd\theta \text{ or } \frac{d\theta}{ds} = \frac{1}{r} \tag{45}$$

where r is the radius of the curvature of the quadrant.

Substitution of equation (44) and (45) into equation (41) yields

$$\frac{d^3\theta}{ds^3} = \frac{Q}{EI} - \frac{1}{2r^3} \tag{46}$$

With the boundary conditions described by equations (42), (43), and (44), integration of equation (46) yields

$$\theta(s) = \frac{1}{6}\left(\frac{Q}{EI} - \frac{1}{2r^3}\right)s^3 \tag{47}$$

The length of a bar is L, so r has a value of $\frac{2L}{\pi}$ and

$$\theta(s) = \frac{\pi}{2L}s \tag{48}$$

We substitute equation (48) into equation (47) and represent Q as a function of s.

$$Q(s) = EI\frac{\pi}{L}\left[\frac{3}{s^2} + \frac{1}{16}\left(\frac{\pi}{L}\right)^2\right] \tag{49}$$

The distributed force Q becomes a function of the position, s, of a beam for the quadrant.

Once we find the distributed load along the beam, we can convert the distributed load to point loads. Since we assume the contact points between the stem of an endoscope and an exoskeleton structure with the assumption of an elastic stem, we can solve for the magnitude of each point load at the given position.

We normalize equation (49) and the distributed load, q(s), can be expressed as

$$q(s) = \pi\left(\frac{3}{s^2} + \frac{\pi^2}{16}\right), \quad where \quad 0 \le s \le 1 \tag{50}$$

or

$$q(\theta) = \frac{\pi^3}{4}\left(\frac{3}{\theta^2} + \frac{1}{4}\right), \quad where \quad 0 \le \theta \le \frac{\pi}{2} \tag{51}$$

By using equation (50), we can calculate the normalized distributed force, q, for the quadrant with the result shown in Figure 56.

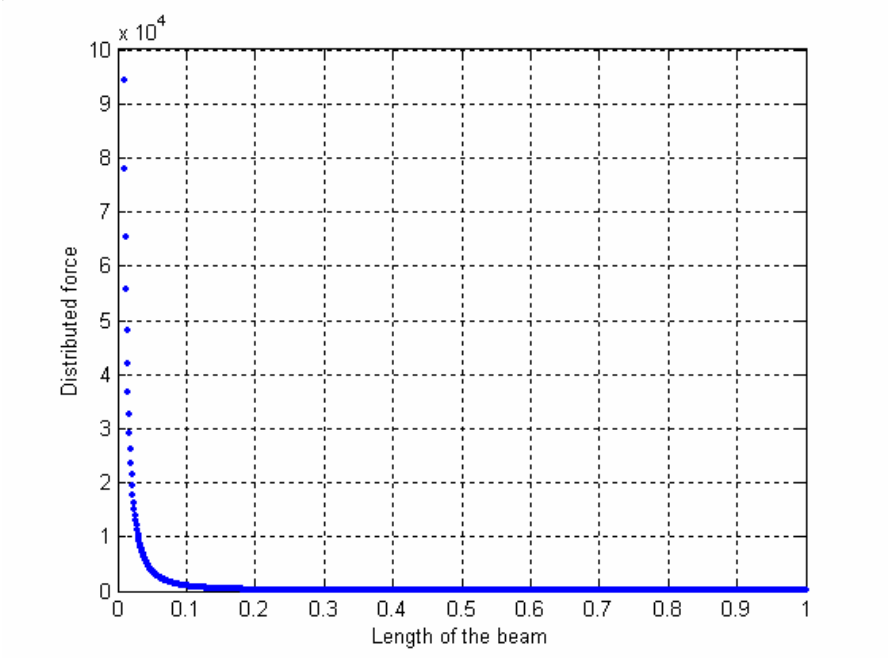

Figure 56. Distributed force versus length of the beam

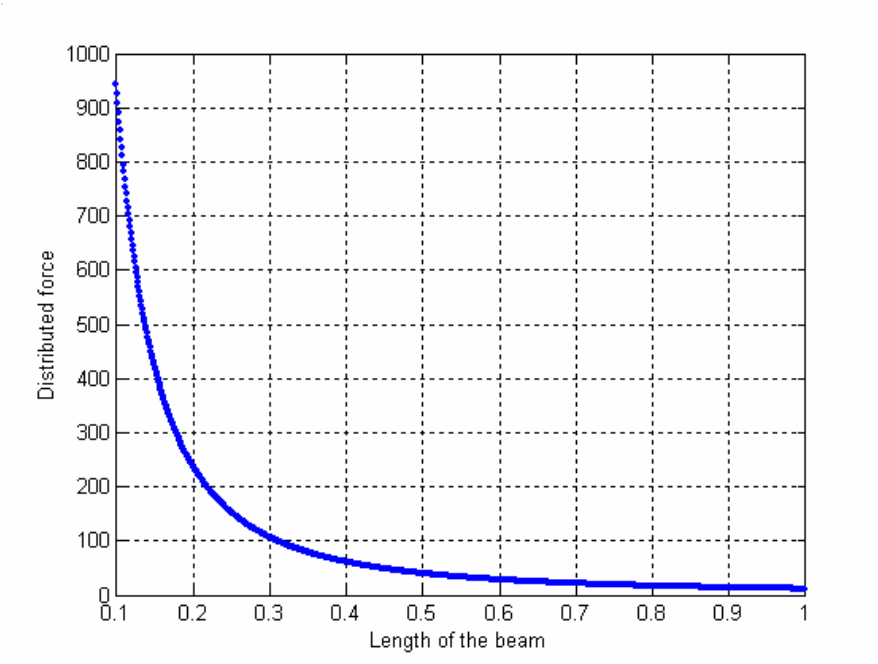

Figure 57. Distributed force versus length of the beam

(Magnified from 0.1 to 1.0 range)

Because the quadrant has a constant radius, and the length of the quadrant is a function of slope angle, we selected the quadrant for the convenience of reducing variables. However, from Figure 56, a beam length from zero to 0.1 yields too high a value for distributed forces. This means that it is hard to make the quadrant shape of a beam with distributed forces, which point toward the center point of the quadrant.

7.3 Reaction forces of the stem of the endoscope

We solve the reaction forces for the configuration of a human colon along the center line of the stem of the endoscope. From Figure 46, we assume that the stem of endoscope passes the center line of the exoskeleton structure, and Figure 58 presents the center line of the stem on Figure 46. We also assume that no twist exists through the stem of an endoscope.

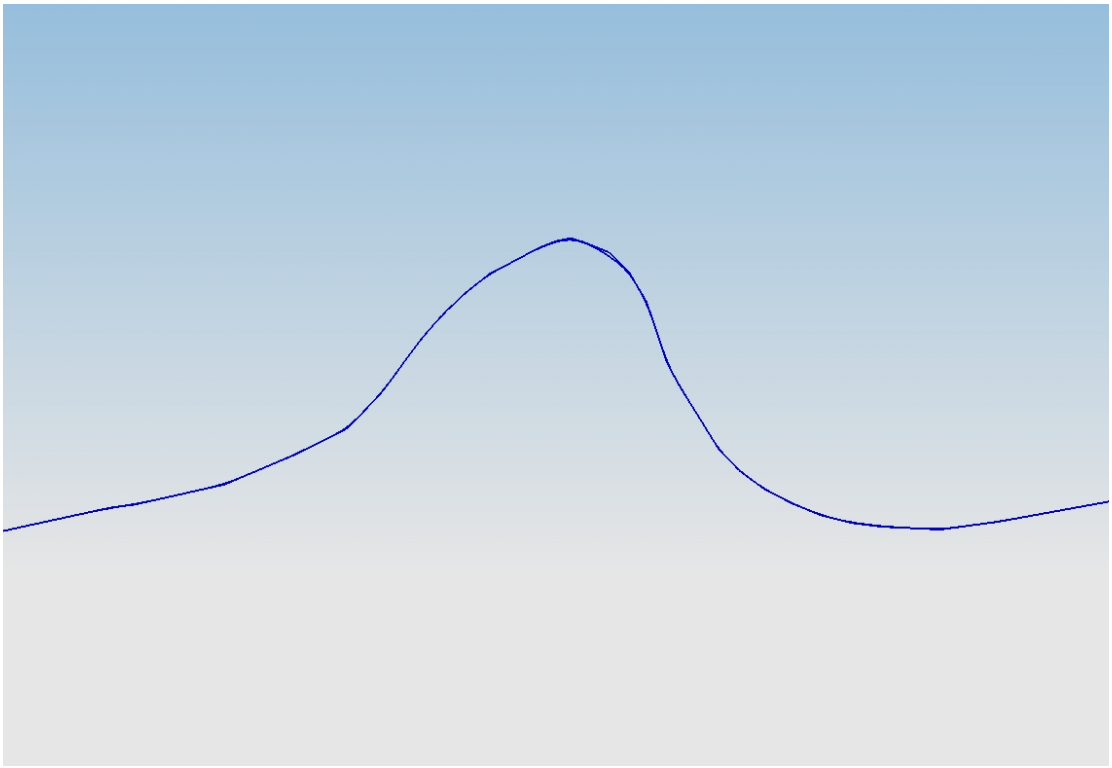

Figure 58. The center line of the stem on Figure 45.

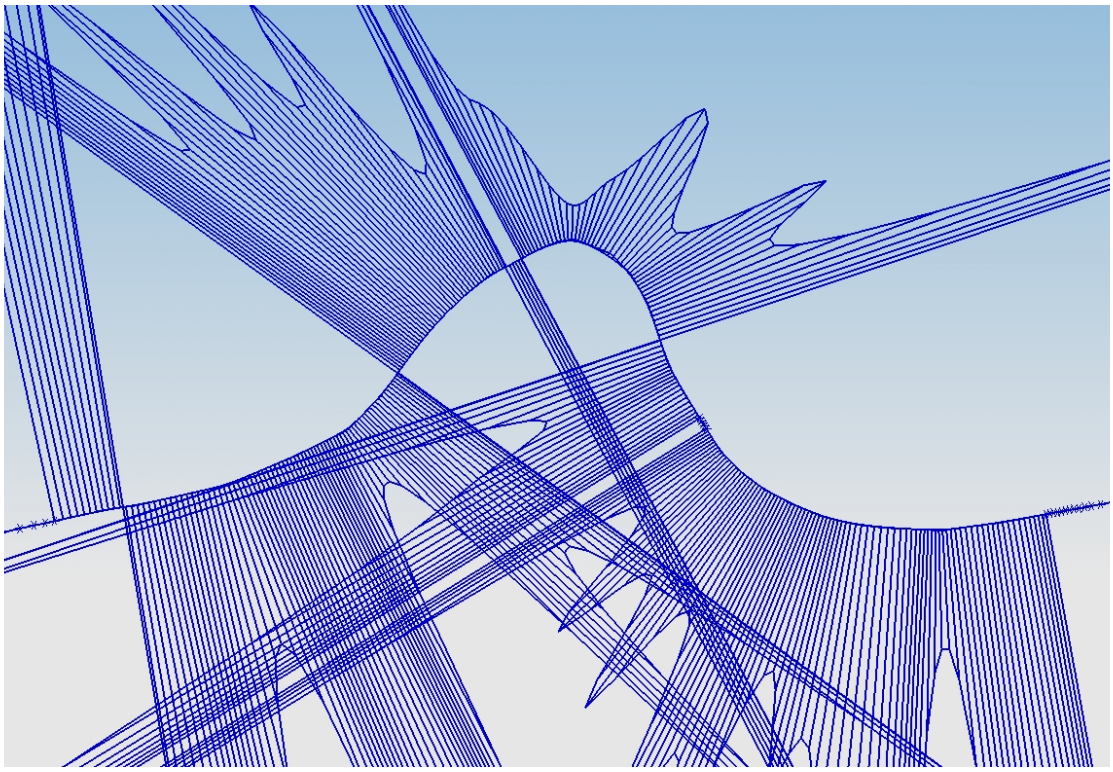

Figure 59. Radius of curvatures on the curve of the stem.
(Radius of curvatures is projected on a plane)

Figure 59 shows the radii of curvature on the curve of the stem, and the radius of curvatures are represented as projected line vectors for the visual convenience. At the straight forward section of the stem, the line lengths are infinities.

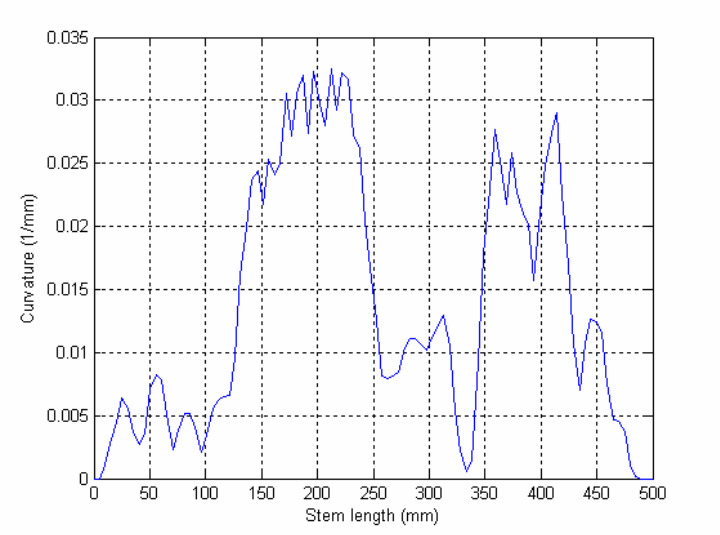

Figure 60. Curvatures on the curve of the stem

Figure 60 shows the curvatures on the curve of the stem. The curvature is an inverse number of the radius of the curvature, and the unit is 1/mm. The zero value of curvature means a straight line at the measured section of the curve.

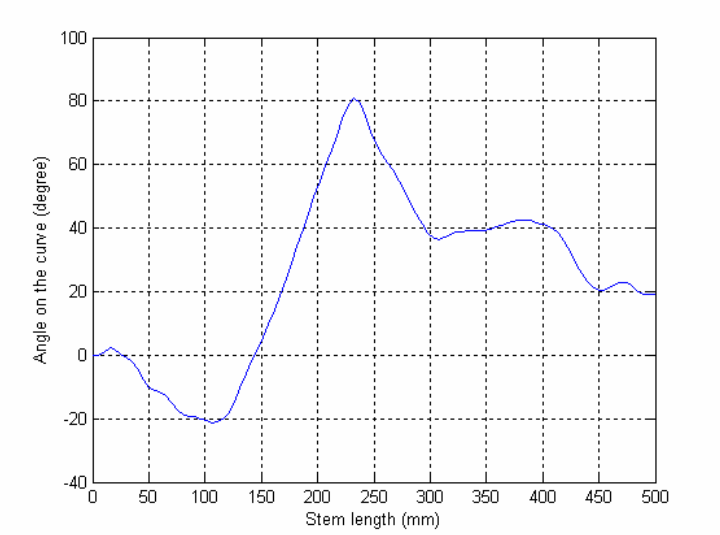

Figure 61. Slope angles on the curve of the stem

Figure 61 shows the slope angles on the curve along the length of stem. We use the Cartesian coordinate system to measure the angle between the x-y plane and the slope of the stem, and the base of the coordinate system is at the left end of the curve on Figure 58. The slope angle is one of the input variables of equation (47), and we measure the slope angles on the curve to solve the reaction forces of the stem.

From equation (47), we can solve the distributed force as a function of the stem length, slope angle of the stem, and the radius of curvature of the stem. The directions of the distributed forces are toward the centers of circles on the curve for the unit length of curvature.

$$Q = EI\left(\frac{6\theta}{s^3} + \frac{1}{2r^3}\right) \tag{52}$$

Where,

Q: Distributed force along the stem (N/m)

E: Elastic modulus of the stem

I: Moment of inertia of the stem ($Kg \cdot m^2$)

s: The stem length (m)

r: The radius of curvature of the stem for a given length (m)

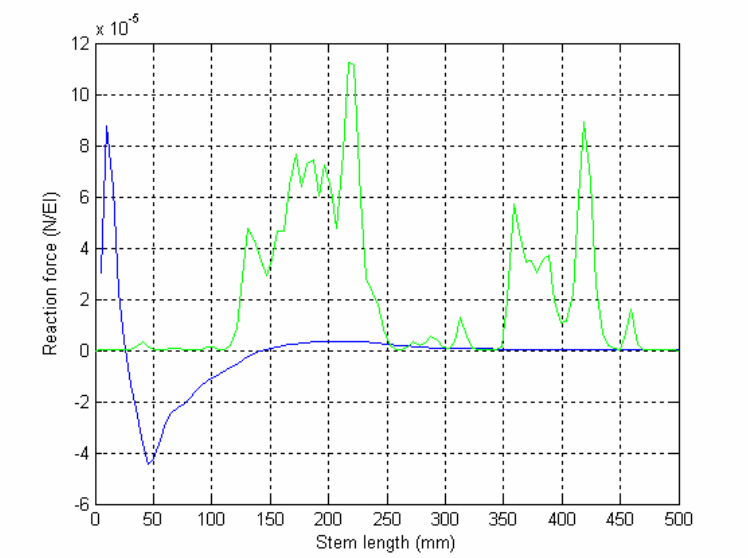

Figure 62. Two components of reaction forces

Figure 62 shows the two different components of reaction forces caused by the radius of curvature and the slope angles of the curve along the length of stem. Negative reaction force means an opposite direction of the reaction force. The first term of the reaction force in Equation 52 is the function of the stem length and the slope angle on the curve. As you can see in Figure 61, the first term of the reaction force affects greatly at the initial length of the stem, and it gradually dies out at the final length of the stem. The second term in Equation 52 is varying with respect to the value of the curvature regardless of the length of the stem.

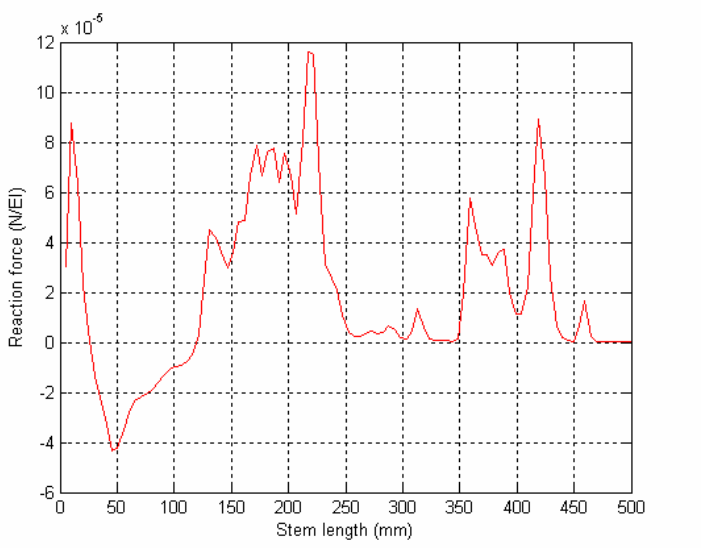

Figure 63. The sum of the reaction force along the stem

Figure 63 presents the total reaction forces along the stem. At the length between zero to 120 mm, the reaction forces caused by the value of slope and the stem length dominate the summed value of the reaction force, and the reaction forces that are the function of the curvature are the main values of the total reaction forces for the rest of the stem length.

From Figure 63, we conclude that the fixed boundary condition in Equation 52 makes the reaction force at the initial region, and small values of radius curvature cause more reaction forces to the exoskeleton structure.

7.4 Conclusion for Chapter 7

In this chapter, we calculated the distributed forces along the stem of the endoscope. We treat the stem of an endoscope as an elastic beam and find the distributed load on the surface of the stem. Distributed loads can be changed to point loads at the specific parts of the units. The point loads are applied to inner surface of the exoskeleton structure, which is comprised of small rigid units.

8 Concluding Remarks

We investigated a minimally invasive endoscope with a flexible stem and stiffenable stem. A summary for the important accomplishment of each chapter is described and the future works are suggested.

8.1 Summary

- We analyzed the mechanical properties of a descending colon. We found the damage level of the colon wall with various sizes of end-tools to help the field of endoscopy.

- The cable force analysis and the closed form solution of the friction coefficient are established to check the stability of the exoskeleton structure.

- From the simple configurations, we tested 2-dimensional and 3-dimensional exoskeleton structure models. Simulation with and without external forces were done to find the range of cable forces, satisfied the friction coefficient, and determined the optimal location of cable holders. We found the orientation of cable holes to minimize the loss of the cable forces and cable wear.

- The closed form solution of the friction coefficient for the four cables was derived to check the stability of the exoskeleton structure.

- External forces caused by the stem of an endoscope were solved for the static case.

8.2 Future Work

- Extended strength test of colon tissue should be taken with various shapes of end-tool.

- The control method of cable forces should be studied with respect to the configuration of the exoskeleton structure and external forces.

- Develop the system control device with the same cable forces. (2 cable and 4 cable systems)

- Develop the variable stiffness control system with partial stiffness control ability. (Currently, our system is for on/off or highly stiffened/highly flexible control.)

- The interaction between a stem of an endoscope and an exoskeleton structure should be considered. The three-dimensional model of a human colon and the effects of point loads caused by the stem inside the exoskeleton structure wall should be studied. Tangential forces caused by the advance of the stem should be considered with the normal forces for a quasi-static analysis.

References

[1] Demling Classen Fruhmorgen, *Atlas of Enteroscopy*, Springer-Verlag Verlin Heidelberg, 1975.

[2] Jack R. Dreyfuss and Murray L. Janower, *Radiology of the Colon*, Waverly Press, Inc. Baltimore, 1980.

[3] Ikuta K, Tsukamoto M and Hirose S, "Shape memory alloy servo actuator system with electric resistance feedback and application for active endoscope," *Proceedings of the 1988 IEEE International Conference on Robotics and Automation*, pp. 427-430, 1988.

[4] A. Menciassi et al., "Robotic Solution and Mechanisms for a Semi-Autonomous Endoscope," *Intl. Conference on Intelligent Robotics and Systems*, pp. 1379-1384, EPFL, Lausanne, Switzerland, October 2002.

[5] Wan Sing Ng, Soo Jae Phee, Choen Seow, and Brian Lawrence Davies, "Development of a robotic colonoscope," *Digestive Endoscopy* (2000) 12, pp. 131-135, 1999.

[6] A. Brett Slatkin, Joel Burdick, "The Development of a Robotic Endoscope," *Proceedings of the 1991 IEEE International Conference on Robotics and Automation*, pp. 2582-2591, 1999.

[7] H.D. Hoeg, A.B. Slatkin, J.W. Burdick, Warren S. Grundfest, "Biomedical Model of the Small Intestine as Required for the Design and Operation of a Robotic Endoscope," *Proceedings of the 2000 IEEE International Conference on Robotics and Automation*, pp. 1599-1606 San Francisco, CA April 2000.

[8] Alexandre Krupa, Jacques Gangloff, Michel F. de Mathelin, Guillaume Morel, Joel Leroy, Luc Soler, and Jacques Marescaux, "Autonomous 3-D Rpsitioning of Surgical Instruments in Robotized Laparoscopic Surgery Using Visual Servoing," *IEEE Transaction on Robotics and Automation*, Vol. 19, No. 5, pp. 842-853 October 2003.

[9] M. Sendoh, K, Ishiyama, and K.-I. Arai, "Fabrication of Magnetic Actuator for Use in a Capsule Endoscope," *IEEE Transactions on Magnetics*, Vol. 39, No. 5, pp. 3232-3234, September 2003.

[10] Tae song Kim, Byungkyu Kim, Dongil Dan Cho, Si Young song, Paolo Dario, and Metin Sitti, "Fusion of Biomedical Microcapsule Endoscope and Microsystem Technology," *The 13th International Conference on Solid-State Sensors*, Actuators and Microsystems, pp. 9-14, Seoul, Korea, June 2006.

[11] Byungkyu Kim, Sunghak Lee, Jong Heong Park, and Jong-Oh Park, "Design and Fabrication of a Locomotive Mechanism for Capsule-Type Endoscopes Using Shape Memory Alloys (SMAs)," *IEEE/ASME Transactions on Mechatronics*, pp. 77-86, Vol. 10, No. 1, February 2005.

[12] Dorin Panescu " Energing Technologies : an imaging pill for gastrointestinal endoscopy," *IEEE Engineering in Medical and Biology Magazine*, pp.12-14 July/August 2005.

[13] Elizabeth V. Mangan, Dan A. Kingsley, Roger D. Quinn, and Hillel J. Chiel, "Development of a Peristaltic Endoscope," *IEEE International Conference on Robotics and Automation*, Washington DC, pp. 347-352, May 2002.

[14] Sturges RH and Laowattana," A Flexible, Tendon-Controlled Device for Endoscopy," *The International Journal of Robotics Research,* Vol. 12,No. 2, pp. 121-131, April 1993.

[15] Yamada H. Yamada Strength of Biological Materials (2nd edition ed.),, Williams and Watkins, Baltimore (1972)

[16] Junghun Choi, and Robert H. Sturges, "Preliminary Element Design and Analysis of a Smart Endoscope," *Flexible Automation & Intelligent Manufacturing*, Toronto, Canada, July 2004.

[17] Junghun Choi, and Robert H. Sturges, "Design and Simulation of a Smart Endoscope," *Intelligent Manupulation and Grasping*, Genoa, Italy, July 2004.

[18] Junghun Choi, and Robert H. Sturges, "Design and simulation of a smart endoscope," *ASME International Mechanical Engineering Congress and RD&D Expo*, Anaheim, California, Nov. 2004.

[19] Phillip J. Ross, *Taguchi Techniques for Quality Engineering*, McGraw-Hill Publishing Company, 1988.

[20] Hual-Te T. Huang, B. Ravani, "Contact Stress Analysis in Ball Screw Mechanism Using the Tubular Medial Axis Representation of Contacting Surfaces," *ASME Journal of Mechanical Design*, Vol. 119, pp. 8-14, March 1996.

[21] S.A. Lukowski, L.A. Medeksza, P.W. Claar, II, "Geometry of Contact and Hertzian Stress Analysis of Frictional Coupling Elements of Multidisk Stepless Transmission with Initial Point Contact," *ASME Journal of Mechanical Design*, Vol. 113. pp. 416-421, December 1991.

[22] L.J. Gutkowski and G.L. Kinzel, "A Coulomb friction model for spherical joints," *ASME Robotics*, Spatial Mechanisms and Mechanical Systems, DE-Vol. 45, pp. 243-250, 1992.

[23] Ali Faraz and Shahram Payandeh, "Towards approximate models of Coulomb frictional moments in: (I) revolute pin joints and (II) spherical-socket ball joints," *Journal of Engineering Mechanics,* 40, pp. 283-396, 2001.

[24] Y.J. Shin and C.H. Kim, "An analytical solution for spherical joint mechanisms including Coulomb friction," *The 6th international pacific conference on automotive engineering*, Vol. I, pp. 383-389, 1991.

[25] Frisch-Fay R., *Flexible Bars*, Butterworth's, London, England, 1962.

[26] Shigeru Nakagiri, "A note on shape finding of elastic bending rod," *Engineering Analysis with Boundary Elements*, 1990, Vol. 7, No. 1, pp. 46-49, 1990.

[27] J.F. Wilson, U. Mahajan,"The Mechanics and Positioning of Highly Flexible Manipulator Limbs," *ASME Journal of Mechanisms*, Transmissions, and Automation in Design, Vol. 111, pp. 232-237, 1989.

[28] L.L. Howel, A. Midha, and T.W. Norton, "Evaluation of Equivalent Spring Stiffness for Use in a Pseudo-Rigid-Body Model of Large-Deflection Compliant Mechanisms," *ASME Journal of Mechanical Design*, Vol. 118, pp. 126-131, March 1996.

[29] Somichai Chucheepsakul, Suraphan Buncharoen, Tsen Huang, "Elastica of Simple Variable-Arc-Length Beam Subjected to End Moment," *ASME Journal of Engineering Mechanics*, Vol. 121, No. 7, July 1995.

[30] S. Navaee, R.E. Elling, "Equilibrium configurations of cantilever beams subjected to inclined end loads," *ASME Journal of Applied Mechanics*, Vol. 59, pp. 572-579, September 1992.

[31] R. H. Plaut, Z. Mroz "Uni-directional buckling of a pinned elastica with external pressure," *International Journal of Solids and Structures,* 29, No. 16, pp. 2091-2100, 1992.

[32] Raymond H. Plaut, Surjani Suherman, David A. Dillard, Brad E. Williams, and Layne T. Watson, "Deflections and buckling of a bent elastica in contact with a flat surface," *International Journal of Solids and Structures,* 36, pp.1209-1229, 1999.

[33] R.H. Plaut, Nurocha L. Williams, and David A. Dillard, "Elastic Analysis of the Loop Tack Test for Pressure Sensitive Adhesives," J. Adhesin, Vol. 76, pp. 37-53, 2001

[34] Raymond H. Plaut, R. Raul Taylor, David A. Dillard, "Postbuckling and vibration of a flexible strip clamped at its ends to a hinged substrate," *International Journal of Solids and Structures,* 41, pp. 859-870, 2004.

[35] Christofer Kuhl, Georges Dumont, "Virtual Endoscopy : From Simulation to Optimization of an Active Endoscopy," *Modeling & Simulation for Computer-aided Medicine and Surgery*, Vol 12, pp. 1-10, Nov. 12-15th, 2002.

[36] Wan Sing Ng et. al,. "Development of a Robotic Colonoscope," *3rd NTU-SGH Symposium*, College of Medicine Building, Singapore, pp. 131-135, 14 Apr 2000.

[37] J. Peirs, et al., "A Miniature Manipulator for Integration in a Self-Propelling Endoscope," *EUROSENSORS XIV*, 14th European Conference on Solid-State Transducers, pp. 309-312, Copenhagen, Denmark, August 27-30, 2000.

[38] Viacheslav I. Egorov, Ilia V. Schastlivtsev, et. al, "Mechanical properties of the human gastrointestinal tract," *Journal of Biomechanics*, Vol. 35, Issue 10, October 2002, pages 1417-1425.

[39] Iman Brouwer, Jeffrey Ustin, Loren Bentley, Alana Sherman, Neel Dhruv, and Frank Tendick, "Measuring In Vivo Animal Soft Tissue Properties for Haptic Modeling in Surgical Simulation," *Medicine Meets Virtual Reality 2001,* IOS Press, pp. 69-74, 2001.

[40] S.J. Phee, W.S. Ng, I.M. Chen, F. Seow-Choen, B.L. Davies, "Locomotion and Steering Aspects in Automation of Colonoscopy Part one: A Literature Review," *IEEE Engineering In Medicine and Biology*, pp. 85-96, November/December 1997.

[41] S.J. Phee, W.S. Ng, I.M. Chen, F. Seow-Choen, B.L. Davies, "Automation of Colonoscopy Part II: Visual-Control Aspects," *IEEE Engineering in Medicine and Biology*, pp. 81-98, May/June 1998.

[42] Byungkyu Kim, Sunghak Lee, Jong Hyeon Park, and Jong-oh Park, "Inchworm-Like Microrobot for Capsule Endoscope," *Proceedings of the 2004 IEEE International Conference on Robotics and Bioimetics*, pp. 458-463, August 22-26, 2004, Shenyang, China.

[43] Dominiek Reynaerts, Jan Peirs, and Hendrik Van Brussel, "Shape memory micro-actuation for a gastro-intestinal intervention system," *Sensors and Actuators,* 77, pp. 157-166, 1999.

[44] A. Aenciassi, Jong H. Park, S. Lee, S. Gorini, P. Dario, Jong-Ok Park, "Robotic Solutions and Mechanisms for a Semi-Autonomous Endoscope," *Proceedings of the 2002 IEEE*, RSJ intl. Conference on Intelligent Robots and Systems EPFL pp. 1379-1384, Lausanne, Switzerland, October 2002.

[45] Yoshihiko Koseki, Toshikatsu Washio, Kiyoyuki Chinzei, and Hiroshi Iseki, "Endoscope Manipulator for Trans-nasal Neurosurgery, Optimized for and Compatible to Vertical Field Open MRI," *Medical Image Computing and Computer-Assisted Intervention*, MICCAI 2002, 5th International Conference, pp. 114-121, Tokyo, Japan, September, 2002.

[46] Christofer Kühl, and Georges Dumont, "Virtual Endoscopy: From Simulation to Optimization of an Active Endoscope," *ESAIM-Proceedings,* MS4CMS 2002, 12:pp. 84-93, November 2002.

[47] Delphine Nain, Steven Haker, Ron Kikinis, and W. Eric L. Grimson, "An Interactive Virtual Endoscopy Tool," *Interactive Medical Image Visualization and Analysis*, Fourth International Conference on Medical Image Computing and Computer-Assisted Intervention - MICCAI'01, 2001.

[48] J. Peirs, D. Reynaerts, and H. Van Brussel, "A Miniature Manipulator for Integration in a Self-Propelling Endoscope," *EUROSENSORS XIV,* the 14th European Conference on Solid-State Transducers, pp. 309-312, Copenhagen, Denmark, August 2000.

[49] Zehel Wendell E., Baumann Dwight M., Brenner William B., Method and apparatus for conducting explaoratory procedures, United States Patent 5251611 October 12, 1993.

[50] Armin Gärtner; medical technics and information technologie, Band II. Medizintechnik und Informationstechnologie, Band II.

[51] Dafnis, G et al. Complications of diagnostic and therapeutic colonoscopy within a defined population in Sweden. Gastrointestinal Endosc 54: 302-9, 2001.

Appendix

A. The closed form solution of the friction coefficient.

The closed form solution of the friction coefficient

$$\mu = \frac{A + \sqrt{B}}{C}$$

Where,

$$A: OD\left(F_1 \cos\phi_1 + F_2 \cos\phi_2\right)$$

$$B: OD^2\left(F_1 \cos\phi_1 + F_2 \cos\phi_2\right)^2 - 4\sin\theta\left[ID\left(F_1 \cos\phi_1 - F_2 \cos\phi_2\right) + 2lt\left(F_1 \sin\phi_1 + F_2 \sin\phi_2\right)\right]$$
$$\left[ID\sin\theta\left(F_1 \cos\phi_1 - F_2 \cos\phi_2\right) - \left(OD - 2lt\sin\theta\right)\left(F_1 \sin\phi_1 + F_2 \sin\phi_2\right)\right]$$

$$C: 2F_1 ID\cos\phi_1 \sin\theta - 2\left[F_2 ID\cos\phi_2 \sin\theta + \left(OD - 2lt\sin\theta\right)\left(F_1 \sin\phi_1 + F_2 \sin\phi_2\right)\right]$$

B. The derivation of the distributed force along the segment of a stem

In Appendix B, we derived the equations from the free-body diagram of Figure 53. The free-body diagram and the equations are from the Plaut's work [31], and we solved them for the fit of our boundary conditions.

We consider the equilibrium state of the stem, represented by Figure 53 for a stem segment. From Figure 53, we can get the sum of the forces along a horizontal direction.

$$N(s)\cos(\frac{d\theta}{2}) + V(s)\sin(\frac{d\theta}{2}) + V(s+ds)\sin(\frac{d\theta}{2}) - N(s+ds)\cos(\frac{d\theta}{2}) = 0 \quad \text{(B-1)}$$

For infinitely small ds, we can approximate the shear force, sin term, and cosine term in equation (B-2).

$$V(s) \approx V(s+ds),\ \sin(\frac{d\theta}{2}) \approx \frac{d\theta}{2}, \text{ and } \cos(\frac{d\theta}{2}) \approx 1 \quad \text{(B-2)}$$

With equation (B-2), equation (B-1) can be expressed as

$$N(s+ds) - N(s) = V(s)d\theta \quad \text{(B-3)}$$

We divide both sides of equation (B-3) by ds.

$$\frac{N(s+ds) - N(s)}{ds} = V(s)\frac{d\theta}{ds} \quad \text{(B-4)}$$

ds goes to zero on the left hand side, resulting in equation (B-5).

$$\frac{dN(s)}{ds} = V(s)\frac{d\theta}{ds} \tag{B-5}$$

We can rewrite equation (B-5) as

$$N' = V\theta' \tag{B-6}$$

The sum of the forces along the vertical direction in Figure 53 is given by equation (B-7)

$$Q\ ds + V(s)\cos(\frac{d\theta}{2}) - V(s+ds)\cos(\frac{d\theta}{2}) - N(s)\sin(\frac{d\theta}{2}) - N(s+ds)\sin(\frac{d\theta}{2}) = 0 \tag{B-7}$$

With equation (B-1), equation (B-7) can be expressed as

$$V(s+ds) - V(s) = Q\ ds - N(s)d\theta \tag{B-8}$$

Dividing both sides of equation (B-8) by ds results in equation (B-9)

$$\frac{V(s+ds) - V(s)}{ds} = Q - N(s)\frac{d\theta}{ds} \tag{B-9}$$

Following the same procedure for the sum of horizontal forces, equation (41) becomes equation (B-10).

$$\frac{dV(s)}{ds} = Q - N(s)\frac{d\theta}{ds} \tag{B-10}$$

This result is expressible as

$$V'(s) = Q - N(s)\theta' \text{ or } Q = V'(s) + N(s)\theta' \tag{B-11}$$

The sum of the moment at position s is zero and for the equilibrium state,

$$M(s+ds) - M(s) - V(s+ds)\frac{ds}{2} - V(s)\frac{ds}{2} = 0 \tag{B-12}$$

With the substitution of equation (B-2) into equation (B-12), equation (B-12) is written as

$$M(s+ds) - M(s) = V(s)ds \tag{B-13}$$

We divide both sides of equation (B-13) by ds, resulting in

$$\frac{M(s+ds) - M(s)}{ds} = V(s) \tag{B-14}$$

As ds approaches zero, the left hand side of equation (B-14) can be expressed as

$$\frac{dM(s)}{ds} = V(s) \text{ or } M' = V(s) \tag{B-15}$$

From the sum of the horizontal and vertical forces and the moment at s, we derive three equations (equations (B-6), (B-11), and (B-15)).

From Euler beam theory,

$$M = EI\frac{d\theta}{ds} \tag{B-16}$$

We substitute equation (B-6) into (B-16) yielding equation (B-17).

$$V = EI\frac{d^2\theta}{ds^2} \tag{B-17}$$

We substitute equation (B-17) into (B-16) resulting in

$$\frac{dN}{ds} = EI\frac{d\theta}{ds}\frac{d^2\theta}{ds^2} \tag{B-18}$$

Integration of equation (B-18) yields

$$N(s) = N_0 + \frac{EI}{2}\left(\frac{d\theta}{ds}\right)^2 \tag{B-19}$$

where N_0 is a constant.

Substitution of equations (B-17) and (B-19) into equation (B-11) yields equation (B-20).

$$EI\frac{d^3\theta}{ds^3} + N_0\frac{d\theta}{ds} + \frac{EI}{2}\left(\frac{d\theta}{ds}\right)^3 = Q \qquad \text{(B-20)}$$

Equation B-20 is for the distributed force along the unit of a stem.

Vita

JungHun Choi was born on June 17, 1972 in Seoul, South Korea. He lived in Seoul, and graduated HwaGok Elementary School, ShinWol Middle School, and MaPo High School in 1991. After graduation, JungHun majored in Biology and Information and Communication Engineering. He earned a Bachelor of Science degree and a Master of Science degree in Automotive Engineering, Kookmin University. In August of 1999, JungHun began his Ph.D. education at Virginia Polytechnic Institute and State University. He completed his Ph.D. degree in Mechanical Engineering on 2006.